APPLIED COMPUTATIONAL ELECTROMAGNETICS SOCIETY JOURNAL

March 2015
Vol. 30 No. 3
ISSN 1054-4887

The ACES Journal is abstracted in INSPEC, in Engineering Index, DTIC, Science Citation Index Expanded, the Research Alert, and to Current Contents/Engineering, Computing & Technology.

The illustrations on the front cover have been obtained from the research groups at the Department of Electrical Engineering, The University of Mississippi.

THE APPLIED COMPUTATIONAL ELECTROMAGNETICS SOCIETY
http://www.aces-society.org

EDITOR-IN-CHIEF

Atef Elsherbeni
Colorado School of Mines, EECS Dept.
Golden, CO 80401, USA

ASSOCIATE EDITORS-IN-CHIEF

Sami Barmada
University of Pisa. EE Dept.
Pisa, Italy, 56126

Yasushi Kanai
Niigata Inst. of Technology
Kashiwazaki, Japan

Ozlem Kilic
Catholic University of America
Washington DC, 20064, USA

Fan Yang
Tsinghua University, EE Dept.
Beijing 100084, China

Mohammed Hadi
Kuwait University, EE Dept.
Safat, Kuwait

Alistair Duffy
De Montfort University
Leicester, UK

Mohamed Bakr
McMaster University, ECE Dept.
Hamilton, ON, L8S 4K1, Canada

Abdul Arkadan
Rafik Hariri University
Chouf 2010, Lebanon

Paolo Mezzanotte
University of Perugia
I-06125 Perugia, Italy

Antonio Musolino
University of Pisa
56126 Pisa, Italy

Marco Arjona López
La Laguna Institute of Technology
Coahuila 27266, Mexico

EDITORIAL ASSISTANTS

Matthew J. Inman
University of Mississippi, EE Dept.
University, MS 38677, USA

Shanell Lopez
Colorado School of Mines, EECS Dept.
Golden, CO 80401, USA

EMERITUS EDITORS-IN-CHIEF

Duncan C. Baker
EE Dept. U. of Pretoria
0002 Pretoria, South Africa

Robert M. Bevensee
Box 812
Alamo, CA 94507-0516, USA

Allen Glisson
University of Mississippi, EE Dept.
University, MS 38677, USA

Ahmed Kishk
University of Mississippi, EE Dept.
University, MS 38677, USA

David E. Stein
USAF Scientific Advisory Board
Washington, DC 20330, USA

EMERITUS ASSOCIATE EDITORS-IN-CHIEF

Mohamed Abouzahra
MIT Lincoln Laboratory
Lexington, MA, USA

Levent Gurel
Bilkent University
Ankara, Turkey

Erdem Topsakal
Mississippi State University, EE Dept.
Mississippi State, MS 39762, USA

Alexander Yakovlev
University of Mississippi, EE Dept.
University, MS 38677, USA

EMERITUS EDITORIAL ASSISTANTS

MARCH 2015 REVIEWERS

THE APPLIED COMPUTATIONAL ELECTROMAGNETICS SOCIETY

JOURNAL

Vol. 30 No. 3 March 2015

TABLE OF CONTENTS

Observed Accuracy of Point-Tested and Galerkin Implementations of the Volume EFIE for Dielectric Targets

Andrew F. Peterson

School of Electrical and Computer Engineering
Georgia Institute of Technology, Atlanta, GA. 30332-0250, USA
peterson@ece.gatech.edu

Abstract **─** Galerkin testing in method-of-moments procedures is defined as the use of the same set of functions as both basis functions and testing functions to construct a linear system from a continuous equation. There is a widespread belief that Galerkin testing enhances the accuracy of numerical results, and this has been shown to be true under certain conditions for surface integral equation formulations. This property is investigated for the volume electric field integral equation (EFIE) applied to dielectric bodies. The relative accuracy obtained in internal fields and scattering cross section for Galerkin and for point testing schemes is compared for a variety of target sizes and materials. In many cases, the point-tested results converge at the same rate as the Galerkin results and are more accurate.

Index Terms **─** Dielectric targets, method of moments, numerical techniques, radar cross section.

I. INTRODUCTION

There are numerous applications requiring accurate numerical solutions for electromagnetic fields in the presence of heterogeneous dielectric bodies. Volume integral equation formulations offer one avenue to approach these problems, and are of interest in conjunction with fast iterative solvers due to their relatively low matrix condition numbers. Formulations based on both the electric field integral equation (EFIE) and the magnetic field integral equation (MFIE) using tetrahedral cells in 3D have been proposed [1-7]. The EFIE approaches impose the integral equation using "Galerkin" testing, where testing functions that are identical to the basis functions are used to enforce the equations and create a linear system. This type of testing scheme imposes a cost in the form of additional integrations that must be carried out to produce the system of equations. Galerkin testing offers the advantage that it produces a symmetric matrix for EFIE formulations, and may make it easier to compute the entries of the system matrix by distributing derivatives and thereby limiting the order of the Green's function singularity. However, there is also a widespread belief that Galerkin testing is associated with a variational principle that enhances the accuracy of the numerical results, specifically the far fields and scattering cross section (SCS) [8-9].

For surface EFIE formulations involving scattering from conducting targets, the SCS accuracy converges at a faster rate than the surface current density when Galerkin testing is used with mixed-order divergence-conforming basis functions [10]. Galerkin-tested results with these basis functions also show faster convergence rates and improved accuracy for SCS compared to point-tested results [10]. However, this "super-convergence" does not happen for all equations and all basis function types [11]. Furthermore, to the author's knowledge, this phenomenon has not been investigated for volume integral equations.

The following considers the widely-used EFIE-D formulation proposed in [1], where the electric flux is represented by mixed-order divergence-conforming Schaubert-Wilton-Glisson (SWG) basis functions. Results obtained using a Galerkin testing scheme to enforce the EFIE are compared with results obtained using point testing in the center of the cell faces. The theory of variational techniques [9] suggests that the accuracy of internal fields obtained by the two approaches should be

Submitted On: October 15, 2014
Accepted On: December 11, 2014

similar, but that the accuracy of the SCS will be improved by Galerkin testing. However, results suggest that this is not the case for most of the examples considered. Often, point testing produces more accurate SCS results than Galerkin testing. Preliminary results of this study were reported in [12-13].

II. THE POINT TESTED EFIE-D FORMULATION

Details of the point-tested EFIE-D formulation are not reported in the literature, so the expressions arising from that scheme that are summarized in this section. The EFIE can be expressed:

$$\bar{E}^{inc} = \bar{E}^{tot} + j\omega\mu_0 \left(\bar{J} * \frac{e^{-jkr}}{4\pi r} \right) + \frac{1}{\varepsilon_0} \nabla \left(\rho_e * \frac{e^{-jkr}}{4\pi r} \right), \quad (1)$$

where the asterisk denotes spatial convolution, ω is the radian frequency, μ_0 and ε_0 are the permeability and permittivity of the background medium, and $k = \omega\sqrt{\mu_0 \varepsilon_0}$ is the wavenumber of the background medium. The electric flux, polarization current, and polarization charge densities are represented by:

$$\bar{D}^{tot}(\bar{r}) \cong \sum_{n=1}^{N_f} D_n \bar{f}_n(\bar{r}), \quad (2)$$

$$\bar{J} \cong j\omega \sum_{n=1}^{N_f} D_n \kappa(\bar{r}) \bar{f}_n(\bar{r}), \quad (3)$$

and

$$\begin{aligned} \rho_e \cong &-\sum_{n=1}^{N_f} D_n \kappa(\bar{r}) \nabla \bullet \left\{ \bar{f}_n(\bar{r}) \right\} \\ &-\sum_{n=1}^{N_f} D_n \left\{ \kappa_n^- - \kappa_n^+ \right\} \delta(\bar{r} - \bar{r}_n), \end{aligned} \quad (4)$$

where $\bar{f}$ denotes an SWG basis function straddling two tetrahedral cells T_n^+ and T_n^- adjacent to face n [1], and $\kappa = (\varepsilon_r - 1)/\varepsilon_r$ denotes the contrast ratio of the appropriate cell, where ε_r is the relative permittivity of that cell. The point-matched approach employs a Dirac delta test function:

$$\bar{T}_m(\bar{r}) = \hat{u}_m \delta(x - x_m) \delta(y - y_m) \delta(z - z_m), \quad (5)$$

where (x_m, y_m, z_m) denotes the center of face m and $\hat{u}_m$ is a normal vector to that face pointing from cell T_m^+ to cell T_m^-. However, since the total electric field exhibits a jump discontinuity at a dielectric boundary, the EFIE must be tested slightly to one side of such an interface, at a point where the total, scattered, and incident fields are all well-defined. For uniqueness, we will test slightly to the T_m^+ side of face *m*.

Point testing produces the system of equations **ZD** = **E**, where the entries of the system are:

$$\begin{aligned} Z_{mn} = &\frac{1}{\varepsilon_0 \varepsilon_{rm}^+} \hat{u}_m \bullet \bar{f}_n(\bar{r}_m) \\ &-\hat{u}_m \bullet \frac{k^2}{\varepsilon_0} \left\{ \kappa_n^+ \iiint_{T_n^+} \bar{f}_n(\bar{r}') \frac{e^{-jkR}}{4\pi R} dv' + \kappa_n^- \iiint_{T_n^-} \bar{f}_n(\bar{r}') \frac{e^{-jkR}}{4\pi R} dv' \right\}_{\bar{r}_m} \\ &-\hat{u}_m \bullet \frac{1}{\varepsilon_0} \nabla \left\{ \frac{a_n \kappa_n^+}{V_n^+} \iiint_{T_n^+} \frac{e^{-jkR}}{4\pi R} dv' - \frac{a_n \kappa_n^-}{V_n^-} \iiint_{T_n^-} \frac{e^{-jkR}}{4\pi R} dv' \right\}_{\bar{r}_m} \\ &-\frac{1}{\varepsilon_0} \left\{ \kappa_n^- - \kappa_n^+ \right\} \hat{u}_m \bullet \nabla \left\{ \iint_n \frac{e^{-jkR}}{4\pi R} dS' \right\}_{\bar{r}_m \text{ in } T_m^+}, \end{aligned} \quad (6)$$

and the excitation vector is:

$$E_m = \hat{u}_m \bullet \bar{E}^{inc}(\bar{r}_m). \quad (7)$$

The evaluation of the first and second expressions in (6) is straightforward; in the latter case there is a $1/R$ singularity at the observer that can be handled by the usual singularity cancellation procedures. The third term in (6) may be expressed as:

$$\begin{aligned} Z_{mn}^Q = &\frac{1}{\varepsilon_0} \frac{a_n \kappa_n^+}{V_n^+} \iiint_{T_n^+} \hat{u}_m \bullet \hat{R} \left\{ (1 + jkR) \frac{e^{-jkR}}{4\pi R^2} \right\} dv' \bigg|_{\bar{r}_m} \\ &- \frac{1}{\varepsilon_0} \frac{a_n \kappa_n^-}{V_n^-} \iiint_{T_n^-} \hat{u}_m \bullet \hat{R} \left\{ (1 + jkR) \frac{e^{-jkR}}{4\pi R^2} \right\} dv' \bigg|_{\bar{r}_m} . \end{aligned} \quad (8)$$

These integrals contain $1/R^2$ singularities at the observer, but since they are volume integrals they are integrable and can also be handled by singularity cancellation transformations.

Finally, when the observation point is located on the source face, the final expression in (6) may be evaluated analytically to produce:

$$\begin{aligned} Z_{mn}^S &= -\frac{1}{\varepsilon_0} \left\{ \kappa_n^- - \kappa_n^+ \right\} \iint_n \hat{u}_m \bullet \hat{R} \left\{ (1 + jkR) \frac{e^{-jkR}}{4\pi R^2} \right\} dS' \bigg|_{\bar{r}_m \text{ in } T_m^+} \\ &= -\frac{1}{2\varepsilon_0} \left\{ \kappa_n^- - \kappa_n^+ \right\}. \end{aligned} \quad (9)$$

In summary, for a point-tested EFIE, the matrix entries are well defined and bounded and may be computed without difficulty. Integrals are performed using adaptive quadrature to an accuracy of at least 3 decimal places.

III. NUMERICAL RESULTS

A variety of results were computed for homogeneous spherical targets of different size and permittivity, using a series of tetrahedral-cell meshes ranging from 32 cells (80 faces) to 3383 cells (7067 faces). The error in each result was determined using exact solutions obtained from the eigenfunction series. The 2-norm error in the scattering cross section is defined:

$$E = \frac{\sqrt{\frac{1}{N_{angles}} \sum_{n=1}^{N_\theta} \sum_{m=1}^{N_\phi} \sin\theta_m \left| \sigma_{exact}(\theta_m, \phi_n) - \sigma_{numerical}(\theta_m, \phi_n) \right|^2}}{\sigma_{exact,\,forward}}, \tag{10}$$

while the 2-norm error in the internal electric field is:

$$E = \frac{1}{\varepsilon_r \eta_0} \sqrt{\frac{1}{N_{faces}} \sum_{n=1}^{N_{faces}} \left| \varepsilon_r E_n^{nor}\Big|_{exact} - \varepsilon_r E_n^{nor}\Big|_{numerical} \right|^2}. \tag{11}$$

The SCS error was averaged on a 30 degree grid in spherical angles (θ,ϕ); the error in internal fields was compared at the center of each face in the mesh.

In addition to results obtained from the point-tested EFIE-D and the Galerkin-tested EFIE-D, we also computed results for each target using the Galerkin-tested EFIE-H formulation, which employs solenoidal basis functions for the electric flux [3,7].

As an illustration of typical results, Fig. 1 shows the error in the bistatic SCS versus number of unknowns for a homogeneous dielectric sphere with $ka = 0.6$ and $\varepsilon_r = 10$, averaged over samples taken every 30 degrees in θ and ϕ. For this target, the Galerkin-tested EFIE-D SCS is slightly more accurate than the point-tested EFIE-D SCS, but both are converging at an approximate rate of O(h^2), where h is the average cell dimension. SCS results were observed to converge at an O(h^2) rate for every target considered in this study, for both point-tested and Galerkin results. The SCS produced by the EFIE-H formulation is somewhat more accurate than either EFIE-D result for a given mesh and for a similar number of unknowns. Figure 2 shows the error in the internal electric fields versus the number of unknowns, for $ka = 0.6$ and $\varepsilon_r = 10$, obtained from (11) by averaging over every cell face in the mesh. The point-tested EFIE-D results are slightly more accurate than the Galerkin-tested EFIE-D results, and are similar in accuracy to the EFIE-H results. In this case, the rate of convergence of the internal electric field appears to be somewhere between O(h) and O(h^2).

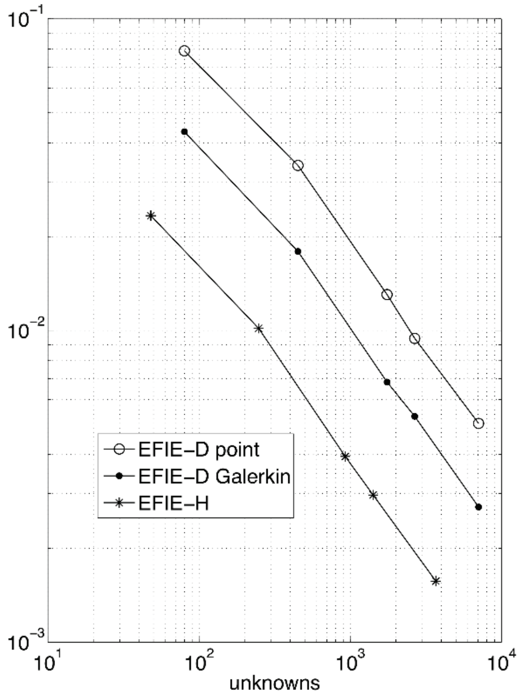

Fig. 1. Error in the SCS for a dielectric sphere with $ka = 0.6$ and $\varepsilon_r = 10.0$.

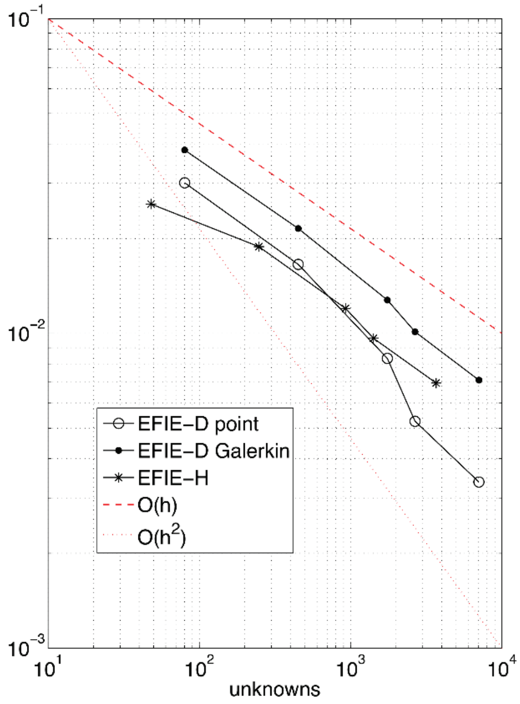

Fig. 2. Error in the internal electric field for a sphere with $ka = 0.6$ and $\varepsilon_r = 10.0$.

Figure 3 shows the error in the SCS versus number of unknowns for a larger sphere with ka = 1.5 and ε_r = 10. For this target, the point-tested EFIE-D SCS is almost an order of magnitude more accurate than the Galerkin-tested EFIE-D SCS, with both converging at an O(h^2) rate. Figure 4 shows the error in the internal electric fields for this target. The point-tested EFIE-D internal field results are more accurate than the Galerkin-tested EFIE-D results. The EFIE-H results exhibit an accuracy between those of the point-tested and Galerkin tested EFIE-D results. In this case, the rate of convergence of the internal electric field appears to be O(h^2) for both point and Galerkin tested approaches.

Table 1 shows the approximate error in the SCS and internal fields for a range of targets, at a common cell density where the average edge length is approximately 0.1 λ_d within the target. For the specific set of models in use, the number of faces (and therefore, the number of unknowns) that corresponds to an average cell edge length of 0.1 dielectric wavelengths is approximately given by:

$$N_{faces} \cong 400(k_0 a)^3 (\varepsilon_r)^{1.5}. \qquad (12)$$

We will use unknown level in (12) to standardize accuracy comparisons. These results are extrapolated from error plots similar to those in Figs. 1-4 using (12) to identify the appropriate number of unknowns. Table 2 shows the observed rate of convergence for the electric field in each set of results. The SCS always appears to converge at an O(h^2) rate.

From Table 1 we observe that, at an average edge length of 0.1 λ_d, the point-tested EFIE-D results for internal fields exhibit an error level of approximately 0.007 across a wide range of target parameters. The error level for the Galerkin-tested EFIE-D internal fields for this average edge length is much more variable, and usually at least twice as high as the point-tested errors. For SCS errors, the point-tested results show a trend of lower error as the effective target size grows, while Galerkin-tested SCS results seem to show the opposite. In other words, from these data, it appears that the Galerkin SCS error grows as either k_0a or ε_r increases, despite the cell dimensions being reduced to compensate for the smaller dielectric wavelength.

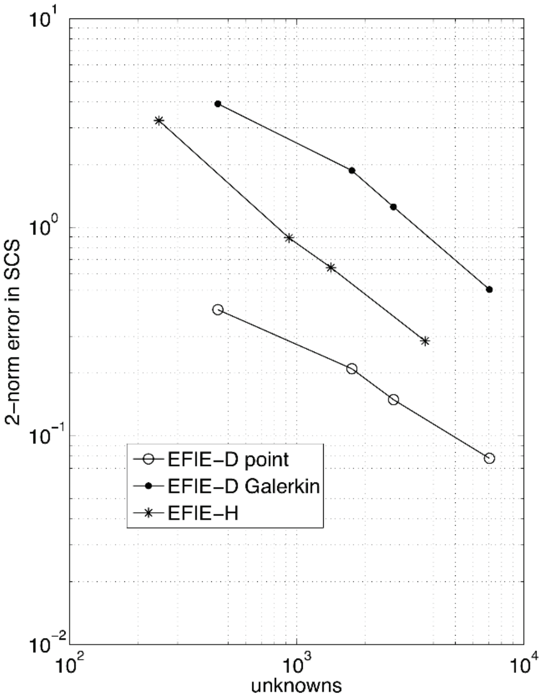

Fig. 3. Error in the SCS for a dielectric sphere with ka = 1.5 and ε_r = 10.0.

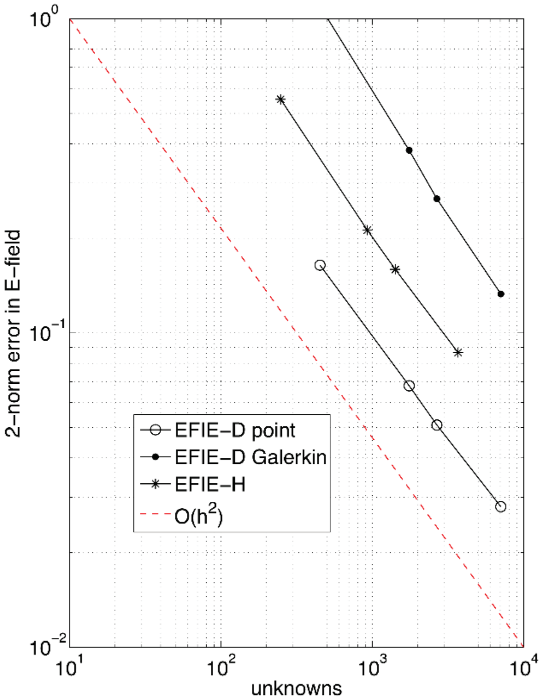

Fig. 4. Error in the internal electric field for a sphere with ka = 1.5 and ε_r = 10.0.

IV. DISCUSSION

For SWG bases, which are fundamentally piecewise-constant functions, the error in the internal fields is expected to converge at an O(h) rate. However, it appears that the field error at the center of the faces of the mesh converges at a superconvergent rate of O(h^2). (A similar effect occurs in numerical solutions of the surface EFIE using RWG basis functions [10-11].) This may explain the convergence rates reported in Table 2, although the effect is not apparent for small target sizes. For the Galerkin-tested EFIE-D, the SCS convergence rate of O(h^2) is expected due to variational properties [8-9]. However, the point-tested SCS also always appears to converge at an O(h^2) rate, which is contrary to expectation (and different from what is observed for the surface EFIE using RWG basis functions and point testing [11]). Since the SCS is computed by actually integrating over the SWG basis functions, one should expect an O(h) convergence rate in the absence of some variational effect.

The author has also investigated two-dimensional volume integral equations using triangular cells, and has observed similar behavior for the TM EFIE with pulse basis functions, and the TE EFIE with RWG basis functions [12]. In both cases, internal field results are usually slightly better with point testing, while SCS results appear to be as good or sometimes better with point testing than with Galerkin testing.

It is also observed in Table 1 that the point-tested results exhibit an SCS error that is usually comparable or larger than the field error, while the Galerkin-tested SCS error is often much smaller than the field error. This observation seems to be in accordance with the Galerkin theory that predicts that the SCS error will be lower than field error [8-9]. However, for these results the point-tested field error is often substantially smaller than the Galerkin-tested field error, so there is no net improvement in SCS error with Galerkin testing.

Table 1: Approximate error levels when the average edge length is 0.1 dielectric wavelengths

ka	ε_r	Unknowns for Avg. Edge Length = 0.1 λ_d	Point-Tested E-Field Error	Galerkin E-Field Error	Point-Tested SCS Error	Galerkin SCS Error
1.0	3	2100	0.007	0.015	0.006	0.006
1.0	5	4500	0.006	0.020	0.005	0.009
1.0	7	7400	0.007	0.035	0.004	0.016
1.0	10	12,600	0.007	0.060	0.0035	0.035
0.35	10	540	0.011	0.008	0.03	0.0034
0.6	10	2700	0.005	0.01	0.009	0.005
1.0	10	12,600	0.007	0.06	0.003	0.035
1.5	10	42,700	0.009	0.03	0.02	0.1

Table 2: Approximate convergence rates for the internal electric field error

ka	ε_r	Point E-Field Error Rate	Galerkin E-Field Error Rate
1.0	3	Between h and h^2	O(h)
1.0	5	O(h^2)	Between h and h^2
1.0	7	O(h^2)	O(h^2)
1.0	10	O(h^2)	O(h^2)
0.35	10	O(h)	O(h)
0.6	10	Between h and h^2	O(h)
1.0	10	O(h^2)	O(h^2)
1.5	10	O(h^2)	O(h^2)

IV. CONCLUSION

Results suggest that for the most widely-used volume integral formulation, the expected benefit of Galerkin testing is not realized in practice for many targets. Galerkin testing imposes a significant additional cost (an order of magnitude) in terms of matrix fill time, while increasing the complexity of the required integrations since observer locations are often closer to source cells as a result of the iterated integrals. However, it seldom produces more accurate near fields and only occasionally produces more accurate far fields than point testing.

It was observed in [7] that the EFIE-H formulation usually outperforms the Galerkin

EFIE-D approach. That observation also applies here, for a wider range of target size and permittivity than considered in [7]. However, in many cases the point-tested EFIE-D outperforms the EFIE-H approach.

In conclusion, when compared to the Galerkin-tested EFIE-D approach [1], the point-tested EFIE-D formulation is more efficient, more accurate for near fields, and usually as accurate for far fields.

REFERENCES

[1] D. H. Schaubert, D. R. Wilton, and A. W. Glisson, "A tetrahedral modeling method for electromagnetic scattering by arbitrarily shaped inhomogeneous dielectric bodies," *IEEE Trans. Antennas Propagat.*, vol. AP-32, pp. 77-85, Jan. 1984.

[2] A. F. Peterson, "A magnetic field integral equation formulation for electromagnetic scattering from inhomogeneous 3-D dielectric bodies," in *Proc. 5th Annual Review of Progress in Applied Computational Electromagnetics*, pp. 387-403, Mar. 1989.

[3] S. A. Carvalho and L. S. Mendes, "Scattering of EM waves by inhomogeneous dielectrics with the use of the method of moments and 3D solenoidal basis functions," *Microwave and Optical Technology Letters*, vol. 23, pp. 42-46, Oct. 1999.

[4] M. M. Botha, "Solving the volume integral equations of electromagnetic scattering," *J. Comp. Physics*, vol. 218, pp. 141-158, 2006.

[5] L. E. Sun and W. C. Chew, "A novel formulation of the volume integral equation for electromagnetic scattering," *Waves in Random and Complex Media*, vol. 19, pp. 162-180, 2009.

[6] J. Markkanen, C.-C. Lu, X. Cao, and P. Yla-Oijala, "Analysis of volume integral equation formulations for scattering by high contrast penetrable objects," *IEEE Trans. Antennas Propagat.*, vol. 60, pp. 2367-2374, May 2012.

[7] A. F. Peterson, "Efficient solenoidal discretization of the volume EFIE for electromagnetic scattering from dielectric objects," *IEEE Trans. Antennas Propagat.*, vol. 62, pp. 1475-1478, Mar. 2014.

[8] S. Wandzura, "Optimality of Galerkin method for scattering computations," *Microwave Opt. Technol. Lett.*, vol. 4, pp. 199-200, Apr. 1991.

[9] A. F. Peterson, D. R. Wilton, and R. E. Jorgenson, "Variational nature of Galerkin and non-Galerkin moment method solutions," *IEEE Trans. Antennas Propagat.*, vol. 44, pp. 500-503, Apr. 1996.

[10] A. F. Peterson, "Beyond RWG/Galerkin solutions of the EFIE: investigations into point-matched, discontinuous, and higher order discretizations," *Proceedings of the 27th Annual Review of Progress in Applied Computational Electromagnetics*, Williamsburg, VA, pp. 117-120, Mar. 2011.

[11] A. F. Peterson, "Observed baseline convergence rates and superconvergence in the scattering cross section obtained from numerical solutions of the MFIE," *IEEE Trans. Antennas Propagat.*, vol. 56, pp. 3510-3515, Nov. 2008.

[12] A. F. Peterson, "Assessment of Galerkin testing for volume integral equations of electromagnetics," *Proceedings of the 30th Annual Review of Progress in Applied Computational Electromagnetics*, Jacksonville, FL, pp. 566-570, Mar. 2014.

[13] A. F. Peterson, "Volume integral equations for electromagnetic scattering from dielectric objects: observations and questions," *Forum for Electromagnetic Research Methods and Application Technologies (FERMAT)*, vol. 5, 10 pages, Sep.-Oct. 2014. (www.e-fermat.org)

Andrew F. Peterson received the B.S., M.S., and Ph.D. degrees in Electrical Engineering from the University of Illinois, Urbana-Champaign in 1982, 1983, and 1986 respectively. Since 1989, he has been a member of the faculty of the School of Electrical and Computer Engineering at the Georgia Institute of Technology, where he is now Professor and Associate Chair for Faculty Development. Within ACES, he has served at various times as a member of the Board of Directors, the Finance Committee Chair, the Publications Committee Chair, and the President. He also served as a Technical Co-Chair for the 25th Annual Review of Progress in Applied Computational Electromagnetics (ACES 2009). He was elevated to ACES Fellow in 2008.

Near-Field Wireless Power Transfer to Embedded Smart Sensor Antennas in Concrete

Xiaohua Jin [1], Juan M. Caicedo [2], and Mohammod Ali [1]

[1] Department of Electrical Engineering
[2] Department of Civil and Environmental Engineering
University of South Carolina, Columbia, South Carolina, 29208, USA
alimo@cec.sc.edu, caicedo@cec.sc.edu

Abstract **─** Wireless power transfer to embedded smart sensor antennas using near-field coupled loop antennas is experimentally studied. Multi-turn loop antennas designed for operation at around 10 MHz show that they can attain fairly high efficiency when properly matched and operated in close proximity to each other whether in free-space or within dry concrete. When one loop is embedded inside 2, 4, and 6 cm of concrete while the other resides over it, it is shown that the embedded loop can receive about 1.9, 1.6, and 1.3 watts of power respectively when the transmit power is 5 watts. Thus, even with an external transmitter with only 1 watt of power (30 dBm) will allow the received power to be 380 mw, 360 mw, and 260 mw for 2, 4, and 6 cm of concrete respectively. It is expected that the use of an even larger loop, magnetic material loading, and or the use of a flux concentrator will increase the efficiency further.

Index Terms **─** Concrete, embedded, near-field, sensor, wireless power.

I. INTRODUCTION

The infrastructure that supports the smooth operation of our society such as, buildings, roads, and bridges has grown in an incredible rate during the last decades. Many of these structures have surpassed their life cycle and require routine structural evaluation to ensure proper operation and safety. In addition, the nation's infrastructure is aging and major upgrades are becoming a necessity. The structural integrity of a building or bridge can be compromised in several ways. For example, the rebar could corrode due to the salt used to de-ice roads, humidity and other environmental factors. This corrosion reduces the area of the steel bars and it eventually changes the stress distribution within the reinforcement. Structural Health Monitoring (SHM) focuses on developing sensor technologies and systems that assesses the integrity of structures [1]-[10]. Apart from conventional visual inspection [11] and ground penetrating radar (GPR) [12]-[13], various types of sensors have been introduced for SHM applications, such as fiber optics [14], strain gauges [15], accelerometers, guided wave [16]-[18] and ultra sound sensors. Such sensors and the necessary wire connections must be installed while the infrastructure is being built or afterwards as retrofits. The wires connect the sensors with their data acquisition stations to which measured data are collected and processed.

In recent years, there has been a growing interest on wireless sensors for structural health monitoring [19]-[27]. Major advantages of wireless sensors over traditional wired sensors are their low cost and ease of installation. Most of the sensors studied in the literature utilize RF (radio frequency) wireless modules that operate outside the infrastructure, and hence some sort of wired connection to the actual measuring unit (strain gauge, humidity sensor) is required for the data to reach the outside wireless unit.

Wireless sensors that can be embedded or buried within the infrastructure, such as a concrete bridge pier during its construction phase would be clearly a better choice. Wireless embedded sensors will have improved reliability since the lack of any wired connection will prevent the sensor from loss of connection due to crack and corrosion in the wire resulting from changes in the surrounding environment. The possibility of developing such

Submitted On: December 9, 2013
Accepted On: October 9, 2014

sensors has been conceptually demonstrated by some RF studies of antennas buried in concrete [28]-[32].

The sensors when placed in appropriate locations of the structure will measure strain, vibration, moisture, etc., and then communicate such data to other sensors and or to a supervisory base station. The sensors will operate independently and will be capable of processing information and make decisions, and hence called *smart sensors*. A basic schematic illustrating a typical sensor deployment scenario is shown in Fig. 1. However, for smart wireless sensors energizing the sensor battery wirelessly from outside is essential because once embedded the sensors cannot be accessed without destroying the structure.

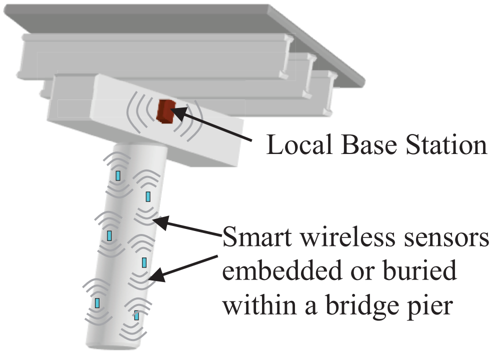

Fig. 1. Proposed distributed embedded or buried wireless sensors within a bridge pier.

In the literature, wireless power transfer has been addressed from two different thrusts: (1) far-field radiated power transfer, and (2) near-field coupled power transfer.

For far-field radiated power transfer, a rectenna [33-35] consisting of an antenna for receiving microwave power, filters, and a diode (mostly Schottky diode) as a rectifying component are needed. The rectenna can receive microwave power and convert it into dc output. Except for difficult to access areas, wireless power transfer using far-field radiated power is very inefficient. For example, in [31] we find that a microstrip patch antenna embedded in 20 mm thick concrete receives only 10.4 mw of power at a distance of 60 cm when the transmit power is 7w.

Clearly for smart sensors embedded in concrete or other structures, wireless power transfer using near-field coupling will be far more efficient than far field wireless power transfer. For the latter case, just above the surface of the infrastructure closely coupled power transfer antennas and transmit circuits will be installed. The transmit circuits and the external antennas can be energized using solar energy or energy from utilities if available. With the proliferation of RFID (Radio Frequency Identification Device), near-field wireless power transfer has become an intense activity of research and development [36-37], [32] including wireless phone battery charging, car battery charging, etc. The objective of this paper is to study the efficacy of wireless power transfer to sensor elements that can be embedded in concrete.

To that end, a multi-turn loop antenna is designed and matched for operation in free-space. Experiments are performed to evaluate the wireless power transmission loss in free-space for two closely coupled loops. Then wireless power transmission loss when one of the loops is embedded in concrete is measured. Measurements are performed for different thicknesses of concrete demonstrating the feasibility to charge the battery of a wireless embedded sensor in concrete.

II. ANTENNA CONFIGURATION

We consider a square spiral loop printed on one side of a 9 cm by 9 cm by 0.0508 cm Rogers 5880 substrate (ε_r=2.2, tanδ=0.0002).

The back side of the substrate does not contain a ground plane. The end of the inner loop turn is connected to a trace on the back surface of the substrate using a via. The loop geometry is shown in Fig. 2. The antenna is fed using a 50 Ω SMA connector. Three loop configurations were investigated (see Table 1).

Table 1: Square spiral loop configurations studied

Loop Type	Name	Width of Strip (cm)	Gap Between Strips (cm)
1	Thin dense	0.1	0.1
2	Plain	0.2	0.2
3	Thin	0.1	0.3

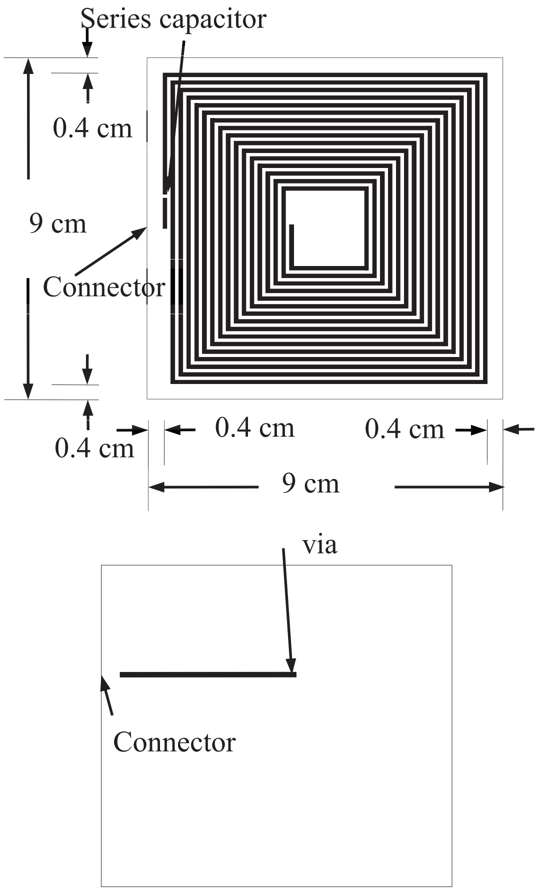

Fig. 2. A multi-turn square spiral loop antenna in free-space with a series chip capacitor. Top and bottom views.

III. SIMULATION RESULTS

Antenna impedance and S-parameters were studied by performing modeling and simulations using Ansys HFSS (High Frequency Structure Simulator). Our objective was to design efficient coupled resonant loop antennas for wireless power transfer where each loop was matched to a 50 Ω feed transmission line. Initially, all simulations were performed at 13.56 MHz. Given the long wavelength (22 meters), the multi-turn loop shown in Fig. 2 is electrically small and thus not self-resonant. In order to force it to resonate at a specific frequency, knowledge about its impedance characteristics is required. Simulated self-resistance data of the three loops listed in Table 1 are plotted in Fig. 3 as function of the number of turns. Clearly, the "Plain" and "Thin" loops have smaller self-resistances which will be difficult to match with a 50 Ω feed transmission line. The self-resistance of the "Thin dense" loop exceeds 50 Ω when the number of turns exceeds 15. Therefore, for this particular board size if we construct a 16 turn loop with trace width of 1 mm and trace gap of 1 mm that will meet our 50 Ω impedance matching requirements.

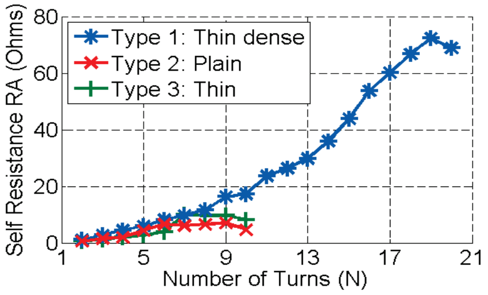

Fig. 3. Simulated loop self-resistance, R_A at 13.56 MHz versus number of turns, N.

Next, we look into the inductance the loop produces. As indicated before, given that this is a magnetic antenna it will have energy stored in its magnetic field which is characterized by its self-inductance. The self-inductances of all three antennas were simulated using HFSS.

Analytically, loop self-inductance is given by [38]:

$$L_{ant} = 2.34\mu_0 N^2 \frac{d_{avg}}{1+2.75p}, \tag{1}$$

where N is the number of turns and based on the coefficients for modified wheeler expression, for the case "Layout - Square", the layout dependent are 2.34 and 2.75, respectively.

For all three loops listed in Table 1, there are the outer diameter d_{out} = 0.082 (m), and the inner diameter $d_{in} = d_{out} - 0.002\,(2N-1)$ (m), $d_{out} - 0.002\,(4N-2)$ (m), and $d_{out} - 0.002\,(4N-3)$ (m) for loops of Type 1, Type 2, and Type 3, respectively, where the average diameter $d_{avg} = \frac{d_{out}+d_{in}}{2}$, fill ratio $p = \frac{d_{out}-d_{in}}{d_{out}+d_{in}}$, and $\mu_0 = 4\pi \times 10^{-7}$ (H/m).

Simulated and calculated (using Eqn. (1)) self-reactance data for these three loops are shown in Fig. 4. Simulated and calculated data are in good agreement for Type 2 and Type 3 loops. For the Type 1 loop (Thin dense), simulated self-reactance is larger than the calculated self-reactance, especially for larger *N*. The difference between the simulated and calculated reactance of Type 1 for higher *N* is due to the larger parasitic capacitance between two adjacent turns.

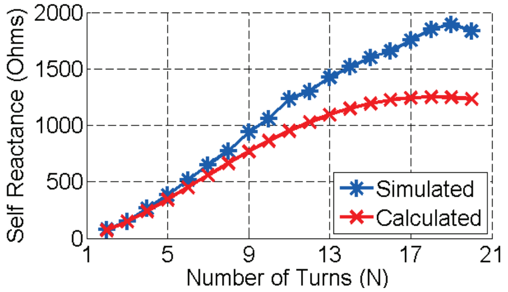

Type 1

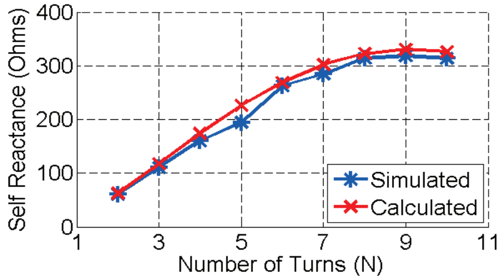

Type 2

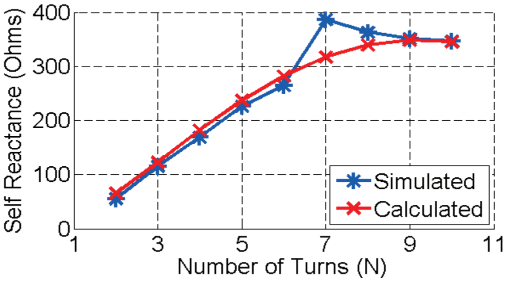

Type 3

Fig. 4. Simulated and calculated (using Eqn. (1)) loop self-reactance, X_A at 13.56 MHz versus *N* for loops of Type 1, Type 2, and Type 3, respectively.

Comparing the self-impedances of Type 2 and Type 3, it is seen that the Type 1 loop can offer much larger input resistance which will make it easier to match it with a 50 Ω line. For example, for *N* = 16 the Type 1 loop has self-impedance of 53.73+j1656 Ω at 13.56 MHz. Simulated self-resistance and reactance of Type 1 (16-turn loop) are shown in Fig. 5 as function of frequency. Both the self-resistance and reactance increases with frequency as expected. It is clear that antenna resistance variation with frequency is fairly slow and would not be a problem for impedance matching. However, because the antenna is electrically very small, the inductance varies quite rapidly and thus the matched bandwidth is expected to be narrow

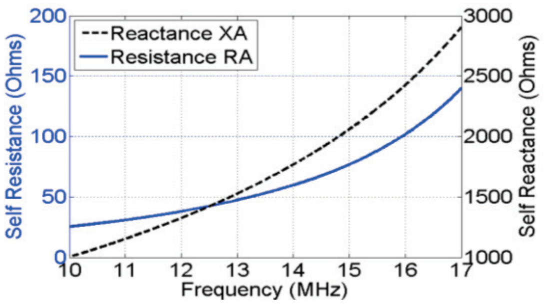

Fig. 5. Simulated self-resistance and reactance of the 16-turn loop versus frequency (MHz).

IV. EXPERIMENTAL RESULTS

A. Free-space measurement results

Figure 6 (a) shows a 16-turn loop that was fabricated on FR4 substrate. Measured S_{11} (dB) data of the loop matched using different chip capacitors are shown in Fig. 6 (b). An Agilent E5071C vector network analyzer (VNA) was used to perform the measurements. It is clear that the tuning frequency can be changed by choosing an appropriate capacitor.

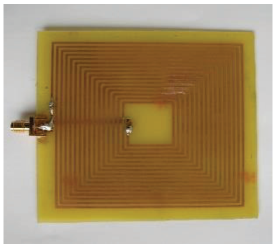

(a)

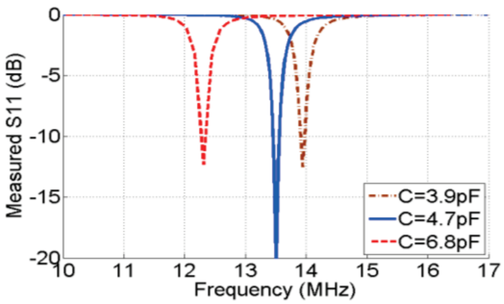

(b)

Fig. 6. Measured S_{11} (dB) data of 16-turn loop versus frequency.

To explore the transmission properties between two resonant loops they were connected to two ports of a VNA and were brought close to each other as shown in Fig. 7 below. Measured S_{11} (dB) data shown in Fig. 8 clearly shows that there are two resonances present when the distance is 3 to 10 cm. Only when the distance is larger (30 cm; i.e., greater than 0.1 wavelength) the double resonance disappears because the coupling between the two loops becomes weaker and the loop behaves like a loop in isolation.

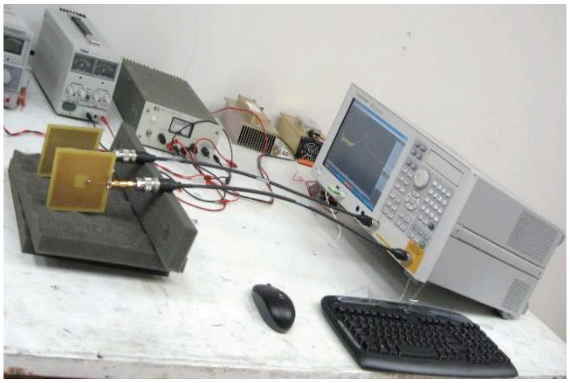

Fig. 7. Measurement setup for two loops in free space.

Measured S_{12} (dB) data for two closely coupled loops at different distances are shown in Figs. 8 (b) and (c). Distance varies as 1 to 5 cm at 1 cm increment and then as 6, 10, 20, and 30 cm. Measured S_{11} (dB) results are shown in Fig. 8 (a), where from it is clear that for 30 cm distance the loop resonance shows a single well-defined resonance that coincides with the resonance of an isolated loop in free-space. As the loops are brought closer and closer mutual coupling increases significantly which is manifested in two resonances.

Measured S_{12} (dB) results show that for distances less than 30 cm the loss is smaller than 10 dB. The (upper or lower) resonant frequencies are listed in Table 2, which will shift according to the relative distance *d* (cm). As apparent, for larger distances the frequencies are closer and eventually merging, while for very short distances the frequencies significantly diverge from each other.

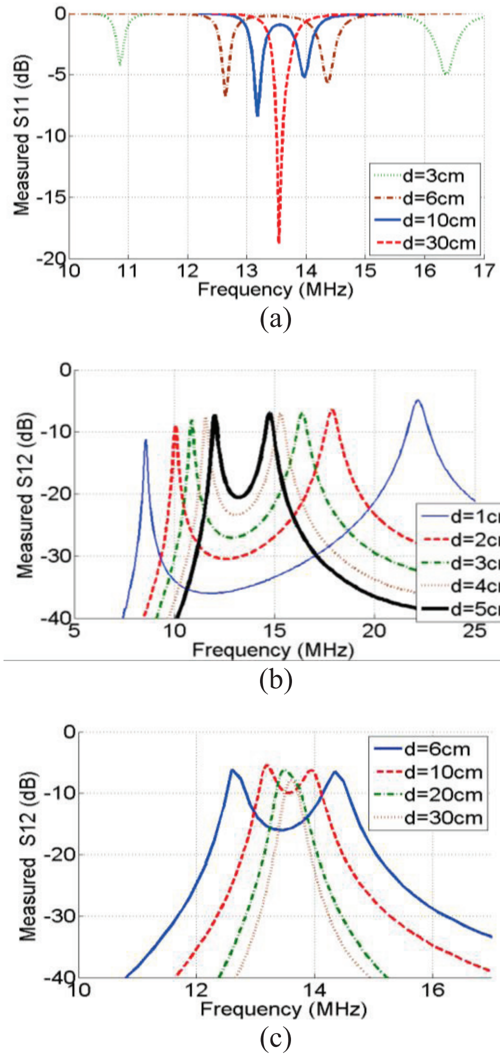

Fig. 8. Measured S-parameters of 16-turn loops at distance, *d*, in free space, *C* = 4.7 pF.

Table 2: Resonant frequency of two loops in free space.

d(cm)	1	2	3	4	5	6	10	20	30
Lower resonant frequency (MHz)	8.58	10.06	10.86	11.58	12.03	12.64	13.18	13.47	13.54
Upper resonant frequency (MHz)	22.15	17.82	16.36	15.30	14.76	14.37	13.96		

B. Measurement results in concrete

Subsequently measurements were performed when one of the loops were embedded inside concrete. This measurement setup is shown in Fig. 9, where the thickness of each concrete slab is 2 cm. Thus, we have the thickness of concrete: t = 2 cm for one layer of concrete, t = 4 cm for two layers of concrete, and t = 0 for no concrete between (*i.e.,* free space). Measured results according to this situation are shown in Fig. 10.

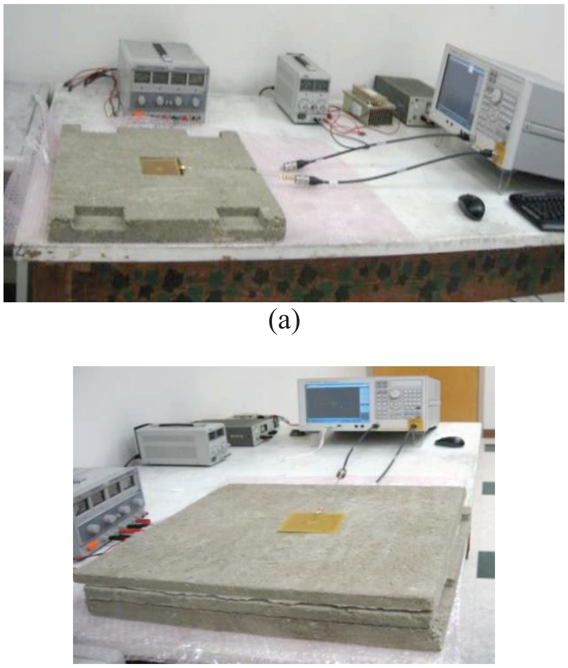
(a)

(b)

Fig. 9. Measurement setup: (a) Loop 1 put inside the concrete, and (b) Loop 2 put near concrete.

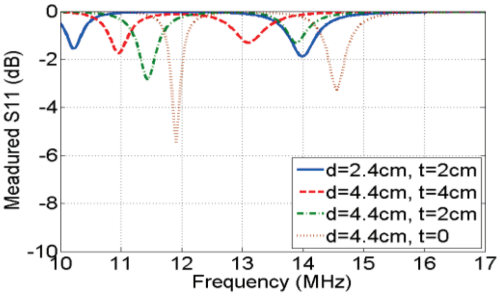

(a)

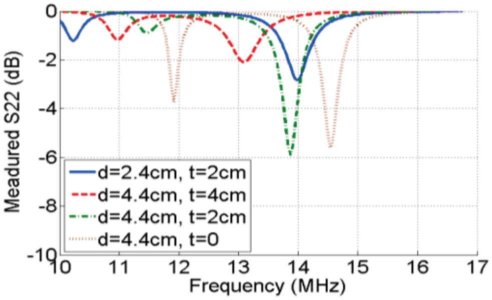

(b)

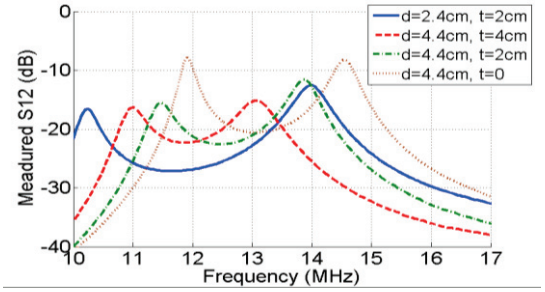

(c)

Fig. 10. Measured S_{11} (dB) for: (a) loop 1 inside concrete, (b) loop 2 touching the surface of concrete with C = 4.7 pF at relative distance d with concrete thickness t, and (c) measured S_{12} (dB) or transmission between the two loops.

Clearly for 2 cm of concrete thickness transmission loss is about 12 dB which increases to 15 dB for 4 cm thick concrete. Free-space loss is about 9 dB. Note that, the coupled antenna system has two closely separated resonant frequencies and we are discussing the performance at the higher frequency. Observing the impedance matching of the external and embedded loops, it is apparent that the matching is not good when the antennas are near concrete. To improve the impedance matching, we decided to use C =15 pF instead of 4.7 pF. The measured results comparing these two matching scenarios are shown in Fig. 11. Note that, with C =15 pF the operating frequency is significantly lower (8.5 MHz as opposed to 14 MHz). Because of the improvement in matching transmission, loss even in concrete is much lower (5 dB for 4 cm of concrete).

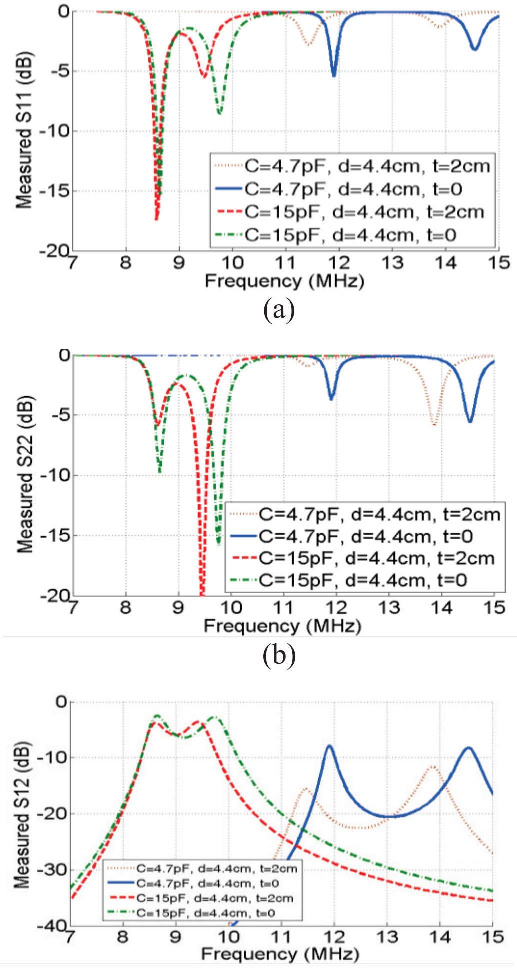

(a)

(b)

(c)

Fig. 11. Measured S_{11} (dB) and S_{12} (dB) or transmission for two loops with C = 4.7 and 15 pF at relative distance d with concrete of thickness t between.

V. RECEIVED WIRELESS POWER

Tests were performed using a power meter and a network analyzer to determine the power transmission efficiencies also. In this case, the power received by the embedded antenna was measured using a power meter. The transmit antenna was connected to a vector network analyzer and was set to signal generator mode of operation. These results are shown in dBm scale in Fig. 12 (a) and in watt scale in Fig. 12 (b). The maximum received powers corresponding to 5W of transmit power are 1.9, 1.6 and 1.3W with 2, 4, and 6 cm of concrete thickness respectively. Hence, the corresponding power transmission efficiencies through concrete are 38%, 32% and 26%, respectively.

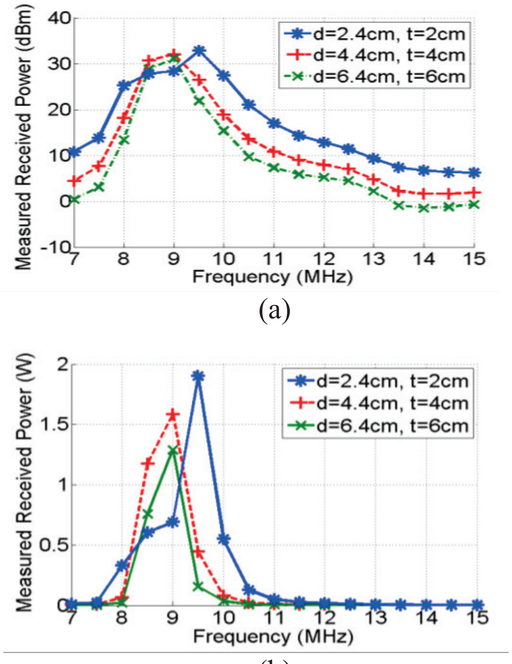

(a)

(b)

Fig. 12. Measured received power results with input 5W to transmitting loop with series capacitor 15 pF.

VI. CONCLUSION

The concept and prospects of energizing the battery of a wireless sensor embedded in concrete are introduced. It is shown that a well-designed pair of coupled resonant loop antennas operating around 10 MHz can achieve nearly 40% power transfer efficiency even in the presence of 2 cm of concrete. Given the loops operate in very close proximity to each other and that their resonant frequencies are susceptible to slight changes in the distance and the environment, proper matching of their impedance under a deterministic scenario will ensure even higher power transfer efficiency. Nevertheless, wireless embedded sensors that require very small power (10-100 mW) can be easily charged using the proposed scheme where both the embedded and external elements are left unattended and are in essence therefore self-sustained.

ACKNOWLEDGMENT

This work was supported in part by the NSF Award ECCS: 0619253.

REFERENCES

[1] S. W. Doebling, C. R. Farrar, M. B. Prime, and D. W. Shevitz, "Damage identification and health monitoring of structural and mechanical systems from changes in their vibration characteristics: a literature review," *Technical Report, Los Alamos National Laboratory*, May 1996.

[2] V. Giurgiutiu and A. Zagrai, "Damage detection in thin plates and aerospace structures with the electro-mechanical impedance method," *Structural Health Monitoring-an International Journal*, vol. 4, pp. 99-118, 2005.

[3] J. M. Caicedo and S. J. Dyke, "Determination of member stiffnesses for structural health monitoring," in *3rd World Conference in Structural Control*, Como, Italy, 2002.

[4] J. M. Caicedo, S. J. Dyke, and E. A. Johnson, "Natural excitation technique and Eigensystem realization algorithm for phase I of the IASC-ASCE benchmark problem: simulated data," *Journal of Engineering Mechanics*, vol. 130, pp. 49-60, 2004.

[5] J. M. Caicedo and S. J. Dyke, "Damage detection on cable-stayed bridges using acceleration measurements," in *7th International Conference on Motion and Vibration Control*, St. Louis, MO, 2004.

[6] J. M. Caicedo and S. J. Dyke, "Experimental validation of structural health monitoring for flexible bridge structures," *J. Struct. Control and Monitoring*, vol. 12, pp. 425-443, 2005.

[7] J. M. Caicedo, N. Catbas, M. Gul, and R. Zaurin, "Phase I of the benchmark problem for bridge health monitoring: numerical data," in *18th Engineering Mechanics Division Conference (EMD2007)*, Blacksburg, Virginia, 2007.

[8] D. Giraldo, J. M. Caicedo, and S. J. Dyke, "Damage detection accommodating varying environmental conditions," *Structural Health Monitoring*, vol. 5, pp. 155-172, 2006.

[9] D. Giraldo, J. M. Caicedo, W. Song, B. Mogan, and S. J. Dyke, "Modal identification through ambient vibration: a comparative study," in *24th International Modal Analysis Conference*, St. Louis, MO, 2006.

[10] J. M. Caicedo, A. Dutta, and B. A. Zarate, "System identification and model updating of the Bill Emerson memorial bridge," in *4th World Conference on Structural Control and Monitoring*, San Diego, CA, 2006.

[11] M. Moore, D. Rolander, B. Graybeal, B. Phares, and G. Washer, "Highway bridge inspection: state of the practice survey," *Federal Highway Administration*, McLean, VA FHWA-RD-01-033, April, 2001.

[12] C. Maierhofer, "Nondestructive evaluation of concrete infrastructure with ground penetrating radar," *Journal of Materials in Civil Engineering*, vol. 15, no. 3, pp. 287-297, May/June 2003.

[13] Ground Penetrating Radar, http://www.geosphereinc.com/gpr_gpradar.html

[14] W. L. Schulz, J. P. Conte, and E. Udd, "Long gauge fiber optic Bragg grating strain sensors to monitor civil structures," *SPIE*, vol. 4330, p. 56, 2001.

[15] T. Nagayama, M. R. Sandoval, B. F. Spencer, Jr., K. A. Mechitov, and G. Agha, "Wireless strain sensor development for civil infrastructure," *Proc., 1st Int. Workshop on Networked Sensing Systems*, pp. 97-100, 2004.

[16] D. N. Alleyne, B. Pavlakovic, M. J. S. Lowe, and P. Cawley, "Rapid long-range inspection of chemical plant pipework using guided waves," *Insight*, 43, pp. 93-96, 2001.

[17] H. Kwun, S. Y. Kim, and G. M. Light, "Long-range guided wave inspection of structures using the magnetostrictive sensor," *J. Korean Soc. NDT*, 21: 383-390, 2001.

[18] J. L. Rose, "Standing on the shoulders of giants: an example of guided wave inspection," *Mat. Eval*., 60, pp. 53-59, 2002.

[19] J. P. Lynch, K. H. Law, A. S. Kiremidjian, T. Kenny, and E. Carryer "A wireless modular monitoring system for civil structures," *Proceedings of the 20th International Modal Analysis Conference*, Los Angeles, CA, February 4-7, 2002.

[20] J. P. Lynch, "Overview of wireless sensors for real-time health monitoring of civil structures," *Proc. of the 4th International Workshop on Structural Control and Monitoring*, New York City, June 10-11, 2004.

[21] S. W. Arms, J. H. Galbreath, A. T. Newhard, and C. P. Townsend, "Remotely programmable sensors for structural health monitoring," *Structural Materials Technology (SMT): NDE/NDT for Highways and Bridges*, Buffalo, NY, September 16, 2004.

[22] J. P. Lynch, A. Sundararajanb, K. H. Lawb, H. Sohnc, and C. R. Farrarc, "Design of a wireless active sensing unit for structural health monitoring," *SPIE 11th Annual International Symposium on Smart Structures and Materials*, San Diego, CA, USA, March 14-18, 2004.

[23] B. F. Spencer, M. Ruiz-Sandoval, and N. Kurata, "Smart sensing technology: opportunities and challenges," *Structural Control and Health Monitoring*, vol. 11, pp. 349-368, 2004.

[24] D. D. L. Mascareñas, *Development of An Impedance Method Based Wireless Sensor Node for Monitoring of Bolted Joint Preload, M.S. Thesis*, University of California, San Diego, 2006.

[25] D. Musiani, K. Lin, and T. Simunic Rosing, **"**Active sensing platform for wireless structural health monitoring," *Proceedings of the 6th International Conference on Information Processing in Sensor Networks*, pp. 390-399, 2007.

[26] K. C. Lu, Y. Wang, J. P. Lynch, P.Y. Lin, C. H. Loh,

and K. H. Law, "Application of wireless sensors for structural health monitoring, *The 18th KKCNN Symposium on Civil Engineering*, Taiwan, December 2005.

[27] S. Kim, S. Pakzad, D. Culler, J. Demmel, G. Fenves, S. Glasser, and M. Turon, "Health monitoring of civil infrastructures using wireless sensor networks," *Proceedings of the 6th International Conference on Information Processing in Sensor Networks*, pp. 254-263, 2007.

[28] J. T. Bernhard, K. Hietpas, E. George, D. Kuchma, and H. Reiss, "An interdisciplinary effort to develop a wireless embedded sensor system to monitor and assess the corrosion in the tendons of pre-stressed concrete girders," *Proc. IEEE Topical Conf. Wireless Communication Technology*, Honolulu, Hawaii, pp. 241-243, October 2003.

[29] K. M. Z. Shams, M. Ali, and A. M. Miah, "Characteristics of an embedded microstrip patch antenna for wireless infrastructure health monitoring," *IEEE Antennas Propagation Society Int. Symp.*, Albuquerque, NM, July 2006.

[30] K. M. Z. Shams, A. M. Miah, and M. Ali, "Gain and transmission properties of an embedded microstrip patch antenna for structural health monitoring application," *IEEE Antennas Propagation Society Int. Symp.*, Honolulu, Hawaii, June 2007.

[31] K. M. Z. Shams and M. Ali, "Wireless power transmission to a buried sensor in concrete," *IEEE Sensors Journal*, vol. 7, no. 12, pp. 1573-1577, December 2007.

[32] O. Jonah and S. V. Georgakopoulos, "Wireless power transfer in concrete via strongly coupled magnetic resonance," *IEEE Trans. Antennas Propagat.*, pp. 1378-1384, March 2013.

[33] B. Strassner and K. Chang, "5.8-GHz circularly polarized dual-rhombic-loop traveling-wave rectifying antenna for low power-density wireless power transmission applications," *IEEE Trans. Microwave Theory Tech.*, vol. 51, no. 5, pp. 1548-1553, May 2003.

[34] M. Ali, G. Yang, and R. Dougal, "A new circularly polarized rectenna for wireless power transmission and data communication," *IEEE Antennas Wireless Propagat. Lett.*, vol. 4, pp. 205-208, 2005.

[35] M. Ali, G. Yang, and R. Dougal, "Miniature circularly polarized rectenna with reduced out-of band harmonics," *IEEE Antennas Wireless Propagat. Lett.*, vol. 5, pp. 107-110, 2006.

[36] K. Finkenzeller, *RFID Handbook*, Second Edition, John Wiley and Sons Inc., 2003.

[37] M. Ali, J. M. Caicedo, and X. Jin, *Wireless Power Transfer to Embedded Sensors*, US Patent Application Number: 20110287713, 2009.

[38] S. S. Mohan, M. del Mar Hershenson, S. P. Boyd, T. H. Lee, " Simple accurate expressions for planar spiral inductances," *IEEE J. of Solid-State Circuits*, vol. 34, no. 10, pp. 1419-1424, October 1999.

Xiaohua Jin received the B.S. and M.E. degrees in Electrical Engineering from Automation Department, Tsinghua University in 1986 and 1989, respectively. She earned the Ph.D. in Mathematics in 2005 and Ph.D. in Electrical Engineering in 2011, both from University of South Carolina, USA. From 2011 to 2014, Jin has been an Assistant Professor at Allen University, South Carolina.

Juan Caicedo is an Associate Professor in the Department of Civil and Environmental Engineering at the University of South Carolina. He received his B.S. in Civil Engineering from the Universidad del Valle in Colombia, South America in 1998. He received his M.S. in 2002 from Washington University in St. Louis and his D.Sc. in 2003 from the same institution. His research interests are in structural dynamics, model updating, structural health monitoring and engineering education. Caicedo is the recipient of the 2009 National Science Foundation CAREER award and has authored and co-authored over 100 conference and journal publications.

Mohammod Ali received the B.Sc. degree in Electrical and Electronic Engineering from the Bangladesh University of Engineering and Technology, Dhaka in 1987, and the M.A.Sc. and Ph.D. degrees, both in Electrical Engineering, from the University of Victoria, Victoria, BC, Canada, in 1994 and 1997, respectively. From January 1998 to August 2001, he was with Ericsson Inc., Research Triangle Park, NC. Since August 2001, he has been with the Department of Electrical Engineering, University of South Carolina at Columbia where currently he is a Professor. Ali is the recipient of the 2003 National Science Foundation Faculty Career Award. He is the author/co-author of over 150 publications and 8 US patents. His research interests include smart antennas, metamaterials and metasurfaces, conformal antennas, and wireless power transfer and wireless sensors.

New Technique to Design Fresnel Zone Plate Antennas

Josefa Gómez, Abdelhamid Tayebi, and Felipe Cátedra

Computer Science Department
University of Alcalá, Alcalá de Henares, 28871, Madrid, Spain
josefa.gomezp@uah.es, hamid.tayebi@uah.es, felipe.catedra@uah.es

Abstract **─** A new method to design Fresnel Zone Plate Antennas (FZPA) is presented in this paper. The proposed method is based on deforming a flat metallic surface in order to achieve the desired phase distribution required to point the main beam to a certain direction. The resulting shaped reflector is modeled by using parametric surfaces, since they allow fitting the real shape of the antenna accurately providing smooth variations. Therefore, the diffraction effect that appears in the transition region between Fresnel zones can be reduced. Unlike bulky parabolic reflectors, FZPAs are much smaller and easy to transport and support, being a promising candidate for satellite communication applications due to its high gain, high polarization purity and minimum volume.

Index Terms **─** Electromagnetic radiation, reflector antennas, satellite communication.

I. INTRODUCTION

Shaped reflector antennas have been typically used to radiate contoured beams in applications where a certain geographical coverage is required [1]. Although contoured beams can also be obtained using array feeds, parabolic shaped reflectors are becoming more popular mainly because they have smaller volume and lower losses, and because array feeds require a complex feeding network. Moreover, the shaping technique is cheaper, since it only needs a single feed element. Parabolic reflectors have been also deformed to improve the antenna performance [2]. For instance, the shaping technique has been applied to increase the aperture efficiency, to improve the beam scanning capabilities, to enhance the polarization purity or to minimize side lobes. These reflectors have been particularly useful in satellite communications because they require simple feeds. However, in practical applications, parabolic reflectors are too bulky and difficult to place due to mechanical constraints. To overcome this limitation, membrane and mesh reflectors have been deployed for space applications. Although these reflectors outperform Fresnel Zone Plate Antennas (FZPA) due to its broad bandwidth, FZPAs have been also studied over a period of many years due to its low profile and low weight. The concept of the zone plate for optical wavelengths was developed by Wood in 1898 [3]. The first millimeter wave usage was reported in 1960 [4]. There are two types of zone plates: one where alternative concentric zones are made opaque or reflecting [5], and the second where phase correction is introduced in successive zones [6]. The latter can be fabricated by cutting grooves in a slab of dielectric material and depositing a thin metal film on the substrate. Thus, each zone is composed of a number of terraces or steps that are used to compensate the phase shifts. Starting from the idea that the bandwidth of the FZPA increases as the number of steps increases, the proposed antenna has been designed considering that the number of steps in the correcting zones tends to infinity. Figure 1 illustrates this concept. It shows the profile of a conventional FZPA with 5 zones and 4 steps per zone and the equivalent profile of the proposed FZPA, where it can be seen that the steps in each zone have been replaced by a NURBS (Non-Uniform Rational B-Splines) surface [7]. Also, note that the shadow regions, which are the transition areas between Fresnel zones, are not completely abrupt.

Hence, the novelty of the proposed antenna is that it is designed by smoothly deforming a flat metallic surface and that it is not composed of

Submitted On: May 24, 2013
Accepted On: September 6, 2014

correcting zones. The modified FZPA present neither terraces nor grooves, and it is defined by continuous parametric surfaces that accurately model the deformations of the metallic surface.

Fig. 1. Schematic profile of a conventional FZPA with 5 zones and 4 steps and schematic profile of the proposed FZPA.

Compared to reflectarray antennas [8, 9], FZPA are easier to manufacture since they do not need any complex layout to reflect the incident field, and FZPA are cheaper since they are made of aluminum and do not require any layer of dielectric substrate. A 60cm x 60cm prototype operating at 10 GHz has been designed and analyzed to validate the benefits of the proposed technology. Although the proposed antenna has not been measured, the full wave Moment Method code that has been used to perform the simulations provides reliable results. The code has been validated with many experimental results.

II. THEORY OF OPERATION

The FZPA operation consists of converting a spherical wave front into a desired scattered wave front by means of an appropriate phase distribution. To achieve this, according to Fig. 2, each point of the original flat surface must introduce a phase shift that is obtained as follows:

$$\phi_i = k_0(d_i - \vec{r_i} \cdot \hat{r_0}) + 2\pi N, \tag{1}$$

where k_0 is the propagation constant in vacuum, $\hat{r_0}$ is the unit vector in the desired direction of the main beam, $\vec{r_i}$ is the position vector from the center of the reflector plane to the i_{th} point of the surface, d_i is the distance from the feed to the i_{th} point and N is an integer number. We obtain the value of N in each $\vec{r_i}$ by imposing that ϕ_i is in the (0, 2π) range.

Most reflectarray antennas use microstrip radiating elements to compensate the phase shift given by (1). The proposed new solution deforms the flat surface to achieve the desired phase distribution. First, the reflector surface is meshed using rectangular patches. The elements of the mesh have the same area that shall be electrically small (less than a half of wavelength) in order we can assume that in each element the amplitude and phase of the current is constant. Once the desired phase distribution ϕ_i is known, the deformed surface can be completely determined by moving each element a certain distance given by (2) if ϕ_i is in the $(0, \pi)$ range and given by (3) if ϕ_i is in the (π, 2π) range.

$$z_i = \phi_i \frac{\lambda}{4\pi}, \tag{2}$$

$$z_i = -\phi_i \frac{\lambda}{4\pi}. \tag{3}$$

As mentioned before, the obtained shaped surface is modeled by NURBS surfaces that exactly fit the deformations that have been conducted on the flat surface. These particular surfaces are able to model accurately any freeform shape, providing an extraordinary realism as they perfectly fit the shape of real objects. Moreover, they are defined as mathematical equations so the computational treatment is not very complicated. NURBS are compatible with several CAD formats and they are invariant under affine transformations.

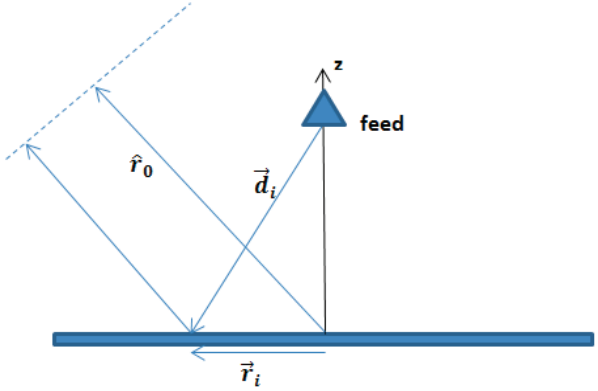

Fig. 2. Diagram of the original flat reflector.

III. VALIDATION AND SIMULATION

A center-fed FZPA has been designed to operate at 10 GHz to radiate a collimated beam in the direction given by θ=10º, ϕ=0º. The total size of the prototype is 20λ x 20λ x 0.5λ. The designed antenna has been fed by using the radiation pattern of a linearly polarized pyramidal horn positioned at x=0, y=0, z=0.45 m. The geometrical model of the proposed antenna is depicted in Fig. 3 and its flat profile can be observed in Fig. 4.

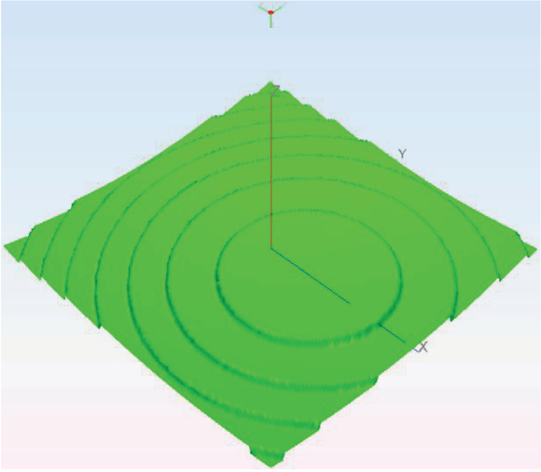

Fig. 3. Geometrical model of the FZPA.

Fig. 4. Side view of the FZPA.

Simulation results based on the Method of Moments (MoM) have been conducted to evaluate the proposed technique. The full wave MoM code Monurbs [10-12] has been used for this purpose. This code has been validated in many benchmark experiments to check its reliability [13-16], showing high accuracy when comparing to measurements. The computed 3D radiation pattern is shown in Fig. 5.

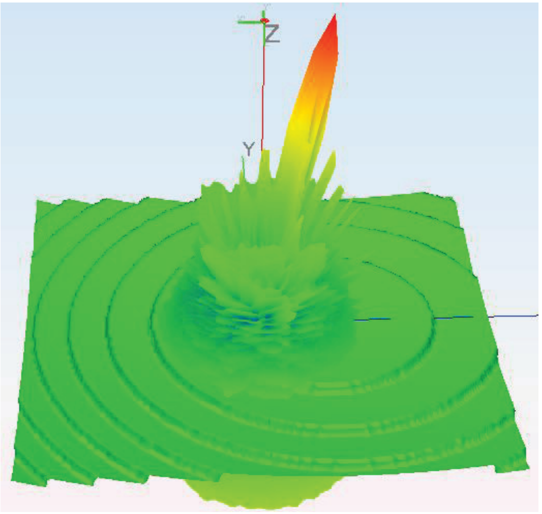

Fig. 5. 3D radiation pattern.

As it can be observed in Fig. 6, the peak gain provided by the FZPA is 33.67 dBi. This implies an aperture efficiency of 46.45%. Figures 7 and 8 depict the E and H planes of the normalized radiation pattern. The side lobe levels of the co-polarized far field radiation pattern are below 18.6 dB regarding the maximum gain level.

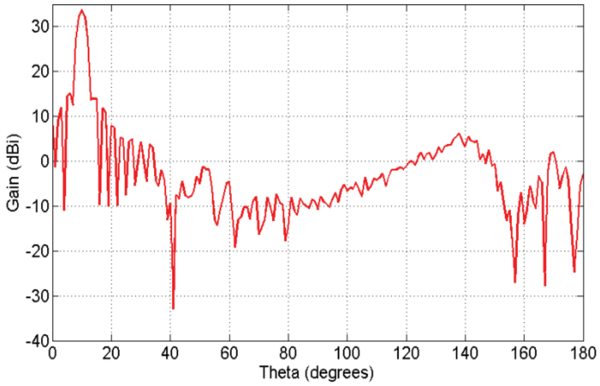

Fig. 6. Gain of the FZPA.

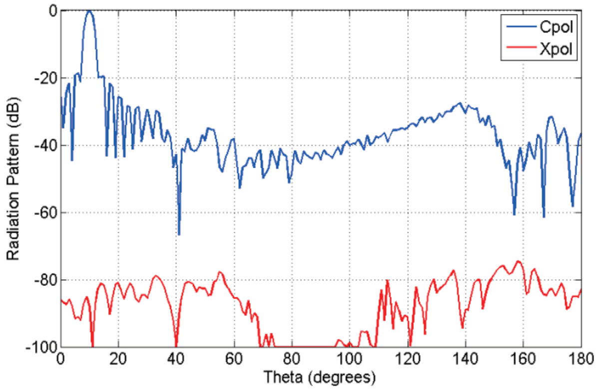

Fig. 7. Normalized far-field radiation pattern. Cut ϕ=0º.

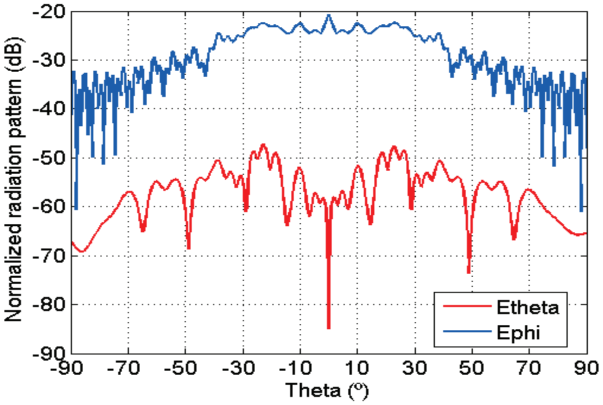

Fig. 8. Normalized far-field radiation pattern. Cut ϕ=90º.

The technique used to design the FZPA has been validated by comparing a previously published similar antenna [17] with a second design. The reference antenna operates at 62.1 GHz, is 150 mm in diameter, 132 mm in focal length, and has an edge illumination level of −12 dB. This design has been analyzed according to the parameters of the reference conventional FZPA antenna. Figure 9 shows the computed gain of the designed antenna. According to Figs. 9 and 10, it can be seen that for the same antenna dimensions and design parameters, the presented antenna with a peak gain of 37.4 dBi and an efficiency of 59.4% surpasses 0.8 dB in gain and 7.7% in efficiency the FZP reported in [17]. Therefore the 3 dB bandwidth of the proposed antenna is also a bit higher than the 22% achieved by the reference antenna.

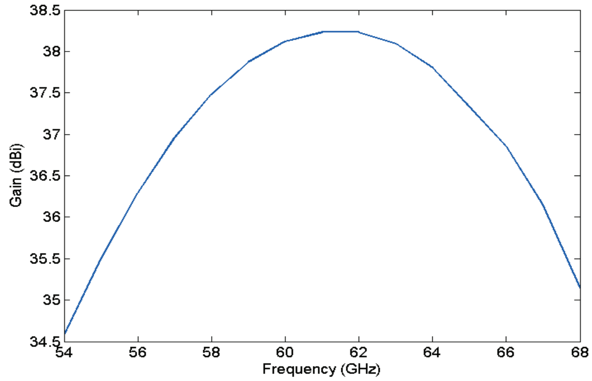

Fig. 9. Computed directive gain against frequency of the FZPA designed using the parameters reported in [17].

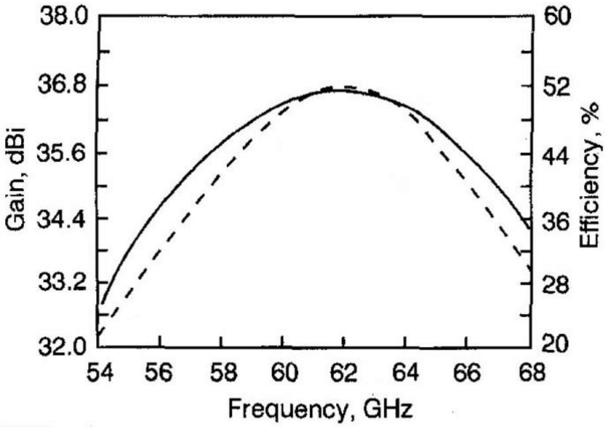

Fig. 10. Directive gain (solid line) and antenna efficiency (dashed line) against frequency of the FZPA reported in [17].

IV. CONCLUSION

A new type of FZPA has been introduced in this paper. This new methodology allows designing low profile reflector antennas with the same advantages as the traditional parabolic reflectors, while remaining a minimum volume. Simulated results reveal that the proposed antenna is very attractive for applications in broadcasting and satellite communications due to their good polarization purity and high gain.

ACKNOWLEDGMENT

This work has been supported in part by the Comunidad de Madrid Project S-2009/TIC1485 and by the Castilla-La Mancha Project PPII10-0192-0083, by the Spanish Department of Science, Technology Projects TEC 2010-15706 and CONSOLIDER-INGENIO No CSD-2008-0068.

REFERENCES

[1] R. Cherrette, S-W. Lee, and R. J. Acosta, “A method for producing a shaped contour radiation pattern using a single shaped reflector and a single feed,” *IEEE Transactions on Antennas and Propagation*, vol. 37, no. 6, pp. 698-706, 1989.

[2] H-H. Viskum and S. B. Sorensen, “A shaped dual reflector optimized for gain, sidelobe performance and low return loss,” *Ninth International Conference on Antennas and Propagation*, (Conf. Publ. No. 407), vol. 1, no. 4-7, pp. 183-186, 1995.

[3] R. W. Wood, “Phase-reversal zone plates and diffraction-telescopes,” *Philosophical Magazine*, series 5, 45, 511, pp. 511-523, 1898.

[4] M. King, J. Rodgers, F. Sobel, F. Wentworth, and J. C. Wiltse, “Quasi-optical components and surface waveguides for the 100 to 300 GHz frequency range,” *Electronic Communications, Inc.*, Report no. 2 on Contract AF19 (604)-5475, Nov. 1960.

[5] H. A. Malliot, “Zone plate reflector antennas for applications in space,” *Proceedings of the Aerospace Applications Conference*, Vail, Colorado, USA, pp. 295-311, Feb. 1994.

[6] J. E. Garrett and J. C. Wiltse, “Antenna pattern characteristics of phase-correcting Fresnel zone plates,” *Proceedings of the IEEE Antennas and Propagation Society International Symposium*, AP-S. Merging Technologies for the 90’s. Digest, Dallas, Texas, USA, pp. 1906-1909, May 1990.

[7] G. Farin, *Curves and Surfaces for Computer Aided Geometric Design*, Academic Press, 1988.

[8] A. Tayebi, J. Gómez, J. R. Almagro, and F. Cátedra, “Broadband high efficiency single-layer reflectarray antenna based on spiral crosses,” *Applied Computational Electromagnetics Society Journal*,

vol. 28, no. 1, pp. 1-7, Jan. 2013.

[9] J. Gómez, A. Tayebi, and F. Cátedra, "Cross-polarization suppression in monolayer reflectarray antennas," *Frequenz*, vol. 67, no. 5-6, pp. 139-143, Apr. 2013.

[10] I. González, E. Garcia, F. Saez de Adana, and M. F. Cátedra, "MONURBS: a parallelized multipole multilevel code for analyzing complex bodies modeled by NURBS surfaces," *Applied Computational Electromagnetics Society Journal*, vol. 23, no. 2, Jun. 2008.

[11] http://www.fasant.com

[12] A. Tayebi, J. Gómez, I. González, L. Lozano, M. J. Algar, E. García, I. Etayo, and F. Cátedra, "Performance comparison between rigorous and asymptotic techniques applied to the analysis of wind turbines," *Applied Computational Electromagnetics Society Journal*, vol. 26, no. 2, Feb. 2011.

[13] I. González, A. Tayebi, J. Gómez, C. Delgado, and F. Cátedra, "Fast analysis of a dual-band reflectarray using two different numerical approaches based on the moment method," *IEEE Transactions on Antennas and Propagation*, vol. 61, no. 4, pp. 2333-2336, 2013.

[14] J. Gómez, A. Tayebi, I. González, and F. Cátedra, "Design of a compact circular waveguide antenna of low polarization level using EBG structures," *Applied Computational Electromagnetics Society Journal*, vol. 26, no. 5, 2011.

[15] I. González, J. Gómez, A. Tayebi, and F. Cátedra, "Optimization of a dual-band helical antenna for TTC applications at S band," *IEEE Antennas and Propagation Magazine*, vol. 54, no. 4, pp. 63-77, 2012.

[16] J. Gómez, A. Tayebi, J. R. Almagro, I. González, and F. Cátedra, "Design and optimization of an EBG antenna with an efficient electromagnetic solver," *International Journal of Antennas and Propagation*, pp. 1-8, 2012.

[17] H. D. Hristov and M. H. A. J. Herben, "Millimeter-wave Fresnel-zone plate lens and antenna," *IEEE Trans. Microw. Theory Tech.*, vol. 43, no. 12, pp. 2779-2785, 1995.

Josefa Gómez was born in 1984. She received the B.S. and M.S. degrees in Telecommunications Engineering from The University Polytechnic of Cartagena, Spain, in 2005 and 2007, respectively, and the Ph.D. degree in Telecommunications Engineering from The University of Alcala, Spain in 2011. She has participated in several research projects with Spanish and European companies. She has been a visiting Ph.D. student at Hong Kong University. Her research interests are design and optimization of antennas, electromagnetic radiation and scattering, on-board antennas analysis and design of graphical user interfaces.

Abdelhamid Tayebi was born in 1983. He received the B.S. and M.S. degrees in Telecommunications Engineering from The University Polytechnic of Cartagena, Spain, in 2005 and 2007, respectively, and the Ph.D. degree in Telecommunications Engineering from The University of Alcala, Spain in 2011. He has participated in several research projects with Spanish and European companies. His research interests focuses on design and optimization of antennas, electromagnetic radiation and scattering, on-board antennas analysis and design of reflectarray antennas.

Felipe Cátedra, IEEE Fellow, received his M.S. and Ph. D. degrees in Telecommunications Engineering from The Polytechnic University of Madrid (UPM) in 1977 and 1982, respectively. From 1976 to 1989 he was with the Radiocommunication and Signal Processing Department of the UPM. He has been Professor at The University of Cantabria from 1989 to 1998. He is currently Professor at The University of Alcalá, in Madrid, Spain. He has worked on about 90 research projects solving problems of Electromagnetic Compatibility in Radio and Telecommunication Equipment, Antennas, Microwave Components and Radar Cross Section and Mobile Communications. He has developed and applied CAD tools for radio-equipment systems such as Navy ships, aircraft, helicopters, satellites, the main contractors being: EADS, ALCATEL, CNES, ALENIA, DASA, SAAB, INTA, BAZAN, INDRA, the Spanish Defence Department, European Spatial Agency, Ericsson, MATRA SPACE, CSELT, KTH, Texas University, Drexel University, Singapore University, Mitsubishi, Kawasaki Heavy Industries, BOSCH, INDRA, GMV, ACCIONA. Recently he promoted the creation of a technology-based company of the University of Alcalá called NEWFASANT (www.fasant.com) for a better transfer of techniques developed by the research team he leads. He has directed about 18 Ph.D. dissertations, has published about 70 papers (IEEE, Electronic Letters, etc.), three books, about 10 chapters in different books, has given short courses and has given around a hundred and thirty presentations in International Symposia.

A New Compact Rectangle-Like Slot Antenna with WiMAX and WLAN Rejection

M. Akbari*[1], M. Khodaee[3], S. Zarbakhsh[1], and Abdelrazik Sebak[2]

[1] Young Researchers and Elite Club
Central Tehran Branch, Islamic Azad University, Tehran, Iran
*akbari.telecom@gmail.com, mo_akba@encs.concordia.ca

[2] Electrical and Computer Department
Concordia University, Quebec H3G 1M8, Canada

[3] Faculty of Eng., Department of Electrical Engineering
Shahid Beheshti University, Tehran, Iran

Abstract **─** In this manuscript, a new CPW-fed slot antenna with two band-notches for ultra-wideband communication systems is proposed. The antenna contains a trapezoid-shaped patch and a slotted ground plane. To achieve two notched bands, both of the inverted L-shaped strip and triangle-shaped element connecting to patch by via are used. The designed antenna is printed on an FR4 substrate with compact size of 20×27 mm^2. Moreover, the antenna has been successfully fabricated and measured, indicating extended impedance bandwidth (3-11.2 GHz, VSWR$\leq$2) and dual band-notched (3.2-3.9 GHz and 5-5.9 GHz) respectively.

Index Terms **─** Coplanar waveguide (CPW) antennas, notched band, ultra wideband (UWB).

I. INTRODUCTION

In recent years, planar structures or printed antennas have attracted much attention due to the set of benefits including simple structure, low profile, easy integration with monolithic microwave integrated circuits (MMICs), and ease of fabrication. In spite of all these advantages, the narrow impedance bandwidth is one of the main challenges of antenna design. Newly, various techniques have been proposed to overcome the narrow bandwidth of these antennas. A big number of antennas with different structures have been experimentally characterized which patch of this type of reported antennas has different shapes such as rectangular, Disc, triangle and oval forms [1-2]. There are many techniques that contain changes in configuration and geometry of patch, feed line, and ground structure which is introduced as the most important of all to enhance the bandwidth and access to UWB bandwidth [3-4]. On the other hand, the frequency range for UWB systems between 3.1 and 10.6 GHz will end up interfering to the existing wireless communication systems, such as the wireless local area network (WLAN) for IEEE 802.11a operating at 5.15–5.35 and 5.725–5.825 GHz, the IEEE 802.16 WiMAX system at 3.3–3.69, 5.25–5.85 GHz; therefore, the UWB antenna with a band-stop performance is needed. For this goal, different techniques with single, dual, and multiple notch functions have been recently reported [5-6]. In this paper, a novel rectangle-like slot antenna with wide impedance bandwidth and dual band-notched characteristic is proposed. By employing both triangle-shaped coupling element and an inverted L-shaped strip, dual band-notch function can be achieved at the central frequencies 3.5 and 5.5 GHz.

II. ANTENNA DESIGN

The configuration and photo of the fabricated antenna are shown in Fig. 1, the proposed antenna has a compact size 20×27 mm^2 which is printed on a FR4 substrate with thickness 1.6 mm and permittivity 4.4. Only reason for using FR4 is its cheap cost. The width of the CPW feedline, Wf, and

Submitted On: November 27, 2013
Accepted On: August 17, 2014

the gap between the ground and feedline, g, are fixed at 2.6 and 0.4 mm respectively. The basic antenna structure contains a trapezoid-shaped patch and a slotted ground plane. As illustrated in Fig. 1, the rectangle-like slot of the ground plane has a width W1 and length L1 and the proposed antenna is connected to a 50 Ω SMA connector for signal transmission. To achieve two notched bands has been used two different techniques, the former an inverted L-shaped strip for filtering 3.2 up to 3.9 GHz, the latter triangle-shaped coupling element on the back side which is connected to patch by a via for generating another notch from 5 up to 5.9 GHz, that both of them seem to be very sharp which will be more examined as follows.

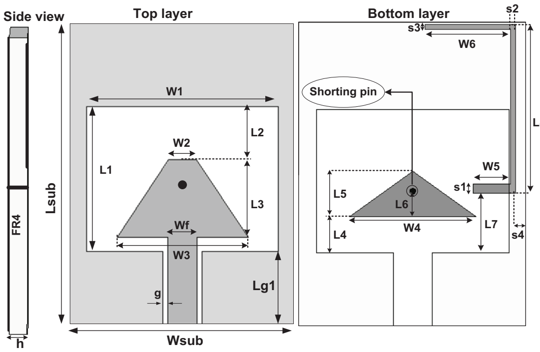

Fig. 1. Geometry of the fabricated antenna.

III. ANTENNA PERFORMANCE AND DISCUSSION

A. Time-domain analysis

Computation of the dispersion that occurs when the antenna radiates a pulse signal is also of interest. The transmit transfer functions of the antennas were used to compute the radiated pulse in different directions when a reference signal was applied at the antenna input. This signal should present an UWB spectrum covering the antenna bandwidth and particularly the FCC mask from 3.1 to 10.6 GHz. It is shown in Fig. 2 an acceptable approximation to a FCC mask compliant pulse can be obtained with a Gaussian seventh derivative. This pulse is represented in the time domain by:

$$G(t) = A.\exp\left(\frac{-t^2}{2\delta^2}\right), \tag{1}$$

$$G^n(t) = \frac{d^nG}{dt^n} = (-1)^n \frac{1}{\left(\sqrt{2}\delta\right)^2}.H_n\left(\frac{t}{\sqrt{2}\delta}\right).G(t), \tag{2}$$

$$H_7(t) = 128t^7 - 1344t^5 + 3360t^3 - 1680t. \tag{3}$$

This signal and its spectrum are represented in Fig. 2. The pulse bandwidth is exactly into mask desired. Luckily, after drawing various Gaussian pulses from the first to eighth derivative, it was obtained that the best pulse for covering FCC mask can be the seventh derivative. Besides, with a bit of tolerance, the sixth and eighth derivative are acceptable. In telecommunications systems, the correlation between the transmitted (TX) and received (RX) signals is evaluated using the fidelity factor (4):

$$F = \max_\tau \left| \frac{\int_{-\infty}^{+\infty} S(t)r(t-\tau)dt}{\sqrt{\int_{-\infty}^{+\infty} S(t)^2 \cdot \int_{-\infty}^{+\infty} r(t)^2 dt}} \right|, \tag{4}$$

where S(t) and r(t) are the TX and RX signals, respectively. For impulse radio in UWB communications, it is necessary to have a high degree of correlation between the TX and RX signals to avoid losing the modulated information. However, for most other telecommunication systems, the fidelity parameter is not that relevant. In order to evaluate the pulse transmission characteristics of the proposed antenna in the case of without notch, two configurations (side-by-side and face-to-face orientations) were chosen. The transmitting and receiving antennas were placed in a d=25 cm distance from each other [7]. As shown in Figs. 3 and 4, although the received pulses in each of two orientations are broadened, a relatively good similarity exists between the RX and TX pulses. Using (4), the fidelity factor for the face-to-face and side-by-side configurations was obtained equal to 0.94 and nearly 0.96 in order. These values for the fidelity factor show that the antenna imposes negligible effects on the transmitted pulses. The pulse transmission results are obtained using CST [8].

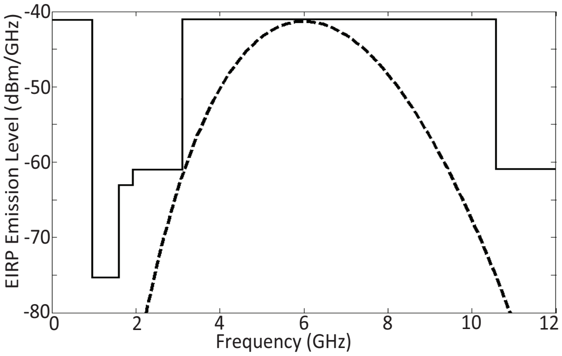

Fig. 2. Power spectrum density compared to FCC mask.

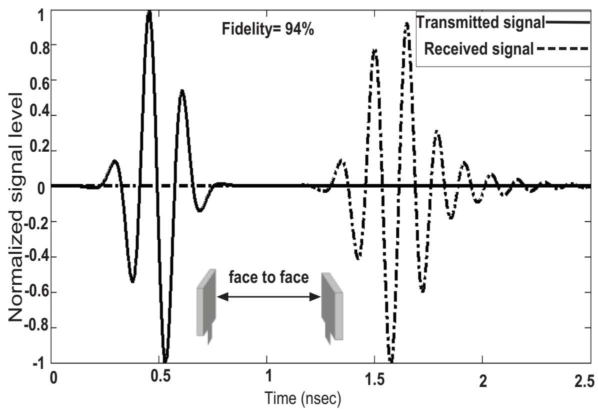

Fig. 3. Transmitted and received pulses in time domain for a UWB link with identical antennas without notches in face-to-face orientation.

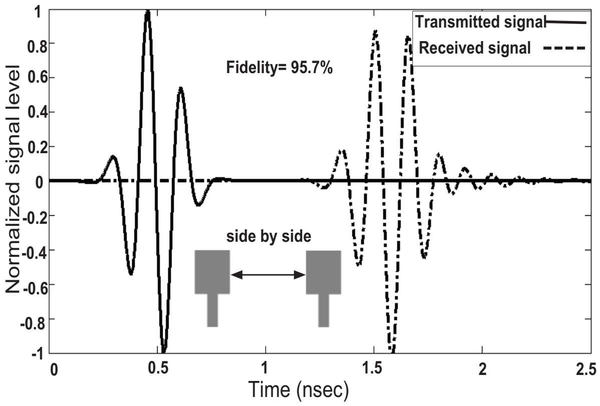

Fig. 4. Transmitted and received pulses in time domain for a UWB link with identical antennas without notches in side by side orientation.

B. Frequency-domain analysis

In UWB systems, the information is transmitted using short pulses. Therefore, it is important to study the temporal behavior of the transmitted pulse. The communication system for UWB pulse transmission must limit distortion, spreading and disturbance as much as possible. Group delay is an important parameter in UWB communication, which represents the degree of distortion of pulse signal. The key in UWB antenna design is to obtain a good linearity of the phase of the radiated field because the antenna should be able to transmit the electrical pulse with minimal distortion. Usually, the group delay is used to evaluate the phase response of the transfer function because it is defined as the rate of change of the total phase shift with respect to angular frequency. Ideally, when the phase response is strictly linear, the group delay is constant;

$$\text{group delay} = \frac{-d\theta(w)}{dw}. \tag{5}$$

As depicted from Fig. 5, the group delay variation for the antenna is presented, which its variation is approximately flat and less than 0.6ns over the frequency band of interest; except dual notched bands, which ensure us pulse transmitted or received by the antenna will not distort seriously and will retain its shape. Hence, the antenna is useful for modern UWB communication systems. Phase S21 for face to face and side by side orientations are also illustrated in Figs. 6 and 7. As previously expected, the plot shows a linear variation of phase in the total operating band except stop bands. It is important to note again, that the distance between both the identical antennas in face to face and side by side orientations is 25 cm which has been extracted from [7]. In the following, the square antenna with different parameters were constructed, and the numerical and experimental results of the input impedance and radiation characteristics are presented and discussed. Triangle-shaped coupling element which is connected to patch by via, and the proposed antenna. Meanwhile, Fig. 8 also illustrates the antenna topology. VSWR (voltage standing wave ratio) characteristics for three antennas mentioned in Fig. 8 are exhibited in Fig. 9. The simulated results are achieved using the Ansoft simulation software high-frequency structure simulator [9].

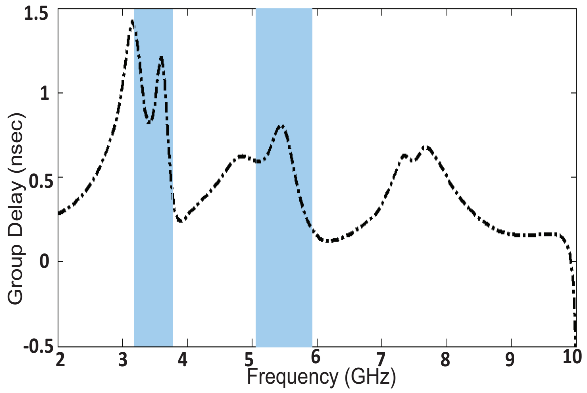

Fig. 5. Group delay of the antenna.

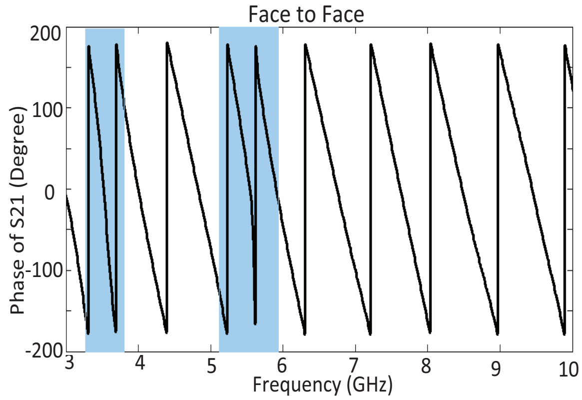

Fig. 6. Simulated phase S21 with a pair of identical antennas for face to face orientation.

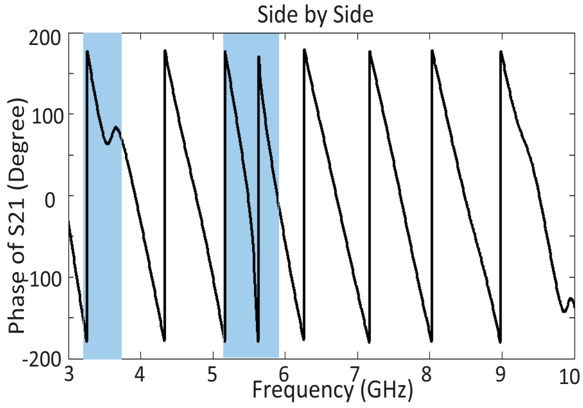

Fig. 7. Simulated phase S21 with a pair of identical antennas for side by side orientation.

The optimal dimensions of the antenna are demonstrated in Table 1. Figure 8 displays the structure of the different slot antennas including: (a) the simple slot antenna without notched bands, (b) the slot antenna with triangle-shaped coupling element and via, and (c) proposed antenna. According to it, by using triangle-shaped coupling element, which is connected to patch by a via shown in Fig. 8 (b), the antenna can filter the WLAN interference band from 5 up to 5.9 GHz. Moreover, the inverted L-shaped strip on the back side, shown in Fig. 8 (c), can create another notched band from 3.2 up to 3.9 GHz. There is an interesting point to note, both of the notched bands obtained are approximately sharp and independent from each other. It means that they have no effect on each other. As depicted in Fig. 10, parameter W6 has a noticeable influence on frequency shifting. With regard to it, with increasing length W6, the center frequency is decreased regularly in a way that with rising 1.5 mm in length W6 centre frequency of the notched band is reduced about 0.5 GHz.

Table 1: Optimal dimensions of the antenna

Wsub	Lsub	h	Wf	W1	W2	W3	W4
20	27	1.6	2.6	16.8	2.4	11.5	11
W5	W6	L1	L2	L3	L4	L5	L6
3.3	7.5	12.7	4.6	6.9	3.2	4	2.25
L7	L8	Lg1	g	S1	S2	S3	S4
5.3	14.9	6.6	0.4	0.8	0.4	0.4	1

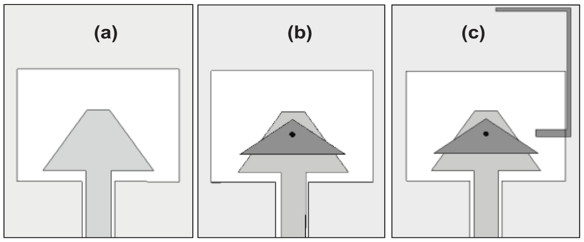

Fig. 8. (a) The simple slot antenna without notched bands, (b) The slot antenna with triangle-shaped element and via, and (c) the proposed antenna.

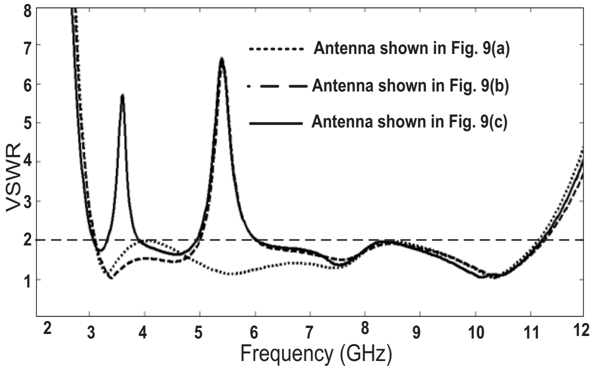

Fig. 9. Simulated VSWR characteristics for antennas shown in Fig. 8.

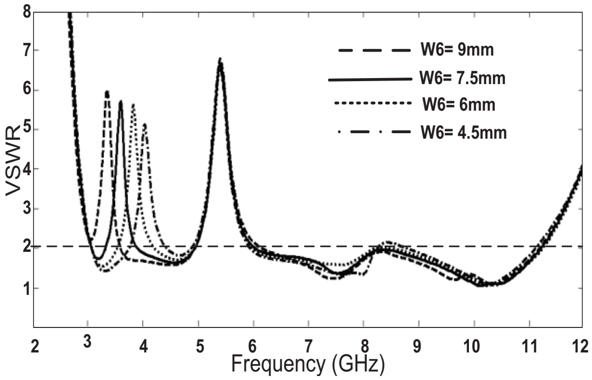

Fig. 10. VSWR characteristics for the antenna with different values W6.

The best value W6 for covering 5.15 to 5.85 corresponds to 7.5 mm. As mentioned before, in this study to generate the band-stop performance on WiMAX band with center frequency 5.5 GHz, is used a triangle-shaped coupling element, which is connected to patch by via. The simulated VSWR curves with different values W4 are plotted in Fig. 11. As exhibited in Fig. 11, when the length W4 increases gradually, center frequency of the notched band is diminished steadily.

Thus, the optimized W4 is 11 mm. From these results, it can be found that the notch frequencies are controllable by changing the lengths W6 and W4. The proposed antenna was fabricated and tested in the Antenna Measurement Laboratory at Iran Telecommunication Research Center.

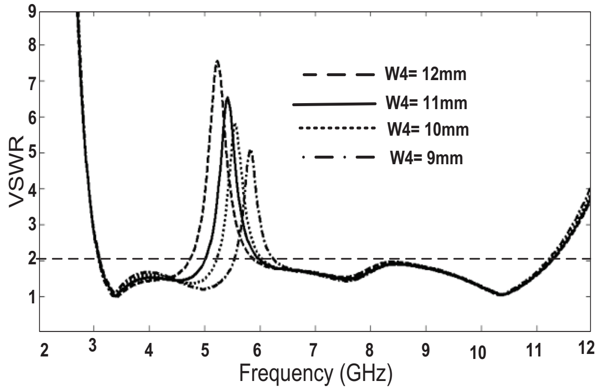

Fig. 11. Simulated VSWR characteristics of the antenna with triangle-shaped element and via with different values W4.

It can also be observed in Fig. 12 (a), by using the triangle-shaped element, the current at 5.5 GHz is more concentrated on it and via. On the other hand, Fig. 12 (b) depicts the current distribution at 3.5 GHz in a way that most current is seen on L-shaped strip indicating its effect in creating the second notched band at centre frequency 3.5 GHz. Figure 13 exhibits the measured and simulated VSWR characteristics of the antenna. The fabricated antenna can cover the frequency band from 3 to 11.2 GHz. The antenna has a compact size of 20×27 mm^2, whereas showing the band rejection performance in the frequency bands of 3.2 up to 3.9 GHz and 5 to 5.9 GHz, respectively. As illustrated in Fig. 13, there is a discrepancy between measured result and simulated data, it is more likely due to the effect of the SMA port. The return loss of the antenna has been measured using an Agilent E8362B network analyzer in its full operational span (10 MHz–20 GHz).

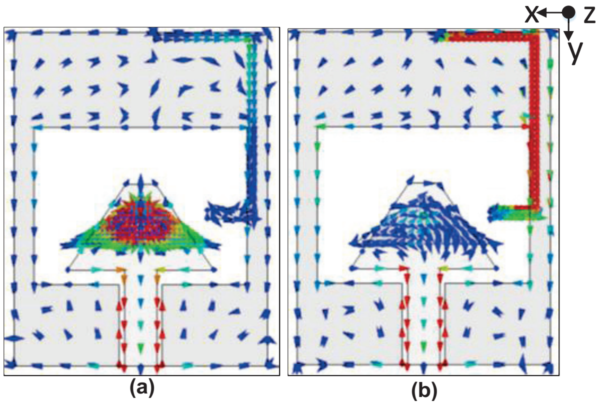

Fig. 12. Simulated current distributions: (a) on the triangle-shaped element and via at 5.5 GHz, and (b) on L-shaped strip at 3.5 GHz.

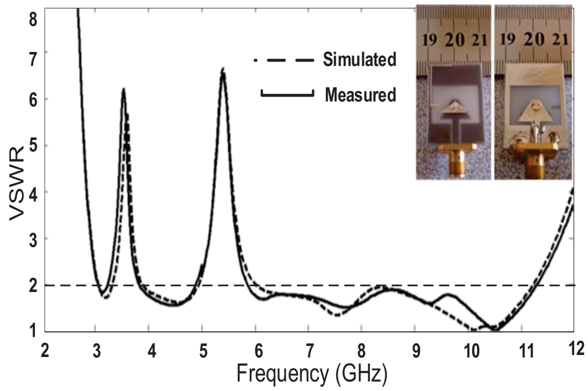

Fig. 13. Measured and simulated VSWR characteristics for the antenna.

Figure 14 shows the measured gain of the antenna with and without stop bands. A sharp fall in gain of the antenna at the centre frequencies of notched bands 3.5, 5.5 GHz, is seen. For other frequencies outside the notched frequency bands, the antenna gain with notch is similar to those without it. Figure 15 depicts the radiation patterns including the co-polarization and cross-polarization in the H-plane (x–z plane) and E-plane (y–z plane) at two frequencies 4.5 GHz and 9 GHz. It can be observed that the radiation patterns in x–z plane are nearly omnidirectional for the two frequencies while radiation patterns in y-z plane or E-plane are about dipole-like shape.

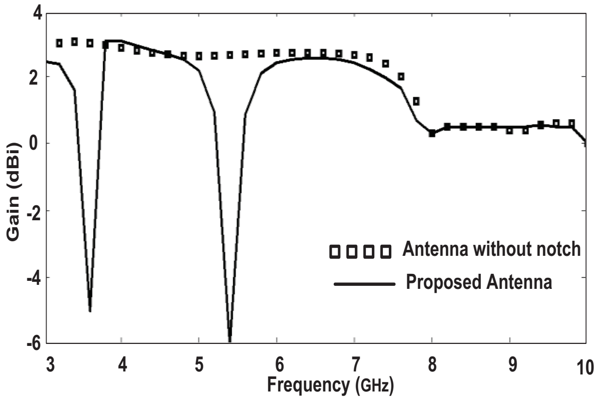

Fig. 14. Measured gain of the antenna without and with notched bands.

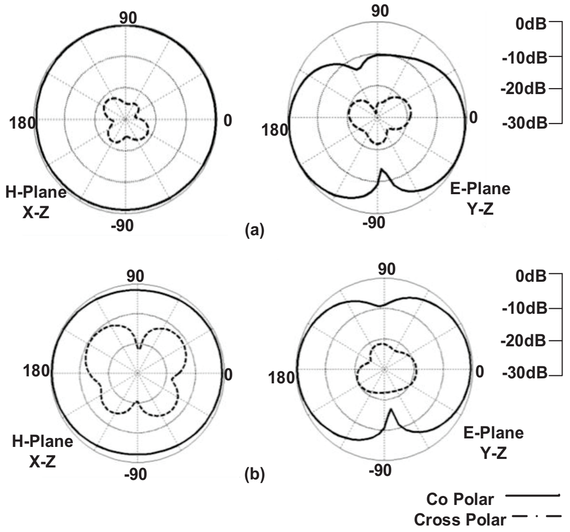

Fig. 15. Radiation patterns of the antenna at: (a) 4.5 and (b) 9 GHz.

IV. CONCLUSION

In this paper, a new CPW antenna with capability of broad impedance bandwidth for UWB applications is presented. The antenna can cover impedance bandwidth from 3 to 11.2 GHz with VSWR≤2 and indicates a good omnidirectional radiation pattern even at higher frequencies. The antenna has a compact size of 20 ×27 mm^2 while exhibiting the band stop performance in the frequency bands from 3.2 to 3.9 GHz and 5 up to 5.9 GHz, respectively. Simulated and experimental results exhibits that the antenna could be a good candidate for UWB application.

REFERENCES

[1] J.-H. Lu and C.-H. Yeh, "Planar broadband arc-shaped monopole antenna for UWB system," *IEEE Transactions on Antennas and Propagation*, vol. 60, no. 7, pp. 3091-3095, 2012.

[2] C.-C. Lin, Y.-C. Kan, L.-C. Kuo, and H.-R. Chuang, "A planar triangular monopole antenna for UWB communication," *IEEE Microwave and Wireless Components Letters*, vol. 15, no. 10, pp. 624-626, 2005.

[3] M. Mighani, M. Akbari, and N. Felegari, "A novel SWB small rhombic microstrip antenna with parasitic rectangle into slot of the feed line," *Applied Computational Electromagnetics Society (ACES) Journal*, vol. 27, no. 1, pp. 74-79, January 2012.

[4] R. Zaker, C. Ghobadi, and J. Nourinia, "Bandwidth enhancement of novel compact single and dual band-notched printed monopole antenna with a pair of L-shaped slots," *IEEE Transactions on Antennas and Propagation*, vol. 57, no. 12, 2009.

[5] R. Emadian, M. Mirmozafari, C. Ghobadi, and J. Nourinia, "Bandwidth enhancement of dual band-notched circle-like slot antenna," *Electronics Letters*, vol. 48, no. 7, pp. 356-357, March 2012.

[6] M. Mighani, M. Akbari, and N. Felegari, "A CPW dual band notched UWB antenna," *Applied Computational Electromagnetics Society (ACES) Journal*, vol. 27, no. 4, pp. 352-359, April 2012.

[7] C. R. Medeiros, J. R. Costa, and C. A. Fernandes, "Compact tapered slot UWB antenna with WLAN band rejection," *IEEE Antennas and Wireless Propagation Letters*, vol. 8, pp. 661-664, 2009.

[8] CST Microwave Studio, ver. 2008. Computer Simulation Technology, Framingham, MA, 2008.

[9] Ansoft HFSS User's Manual, Ansoft Corporation, Beta Release 11.0, April 2007.

Oblique Incidence Plane Wave Scattering from Large Finite Arrays Using EV-AEF Method

Wei Shao, Jia-Lin Li, and Qifei Li

School of Physical Electronics
University of Electronic Science and Technology of China, Chengdu, 610054, China
weishao@uestc.edu.cn, jialinli@uestc.edu.cn, qifei_li@163.com

Abstract **─** An efficient method for calculating scattering patterns of large finite arrays illuminated by an obliquely incident plane wave is presented in this paper. Based on the element-varying active element factor (AEF) technique, this method takes the element mutual coupling and edge effects into account, and it results in accurate solutions. From the periodicity and distribution properties of induced currents, various elements are combined according to a certain rule. The determination of element combination is related to the plane wave incident angle. Thus, the scattering pattern of a large finite array can be calculated with superposition of combined-elements in a relatively small array. Numerical examples of one-dimensional (1-D) and two-dimensional (2-D) arrays verify the accuracy and efficiency of the proposed method.

Index Terms **─** Active element factor, large finite arrays, oblique plane wave, scattering pattern.

I. INTRODUCTION

Direct numerical methods are often used to calculate the scattering field from a small array or an infinite periodic array. Numerical methods, such as the method of moment (MoM) [1], finite element method (FEM) [2], and finite-difference time-domain (FDTD) method [3], lead to an accurate and effective solution for a small array calculation. For an infinite periodic array, only an element is required to be simulated with the Floquet's theorem or periodic Green function [4-5]. The numerical methods, however, become inefficient or even infeasible for rather large finite arrays when considering the mutual coupling effects in the whole array environment. In this case, approximate methods are needed to reduce memory requirements and computing time for array calculation.

An active element pattern (AEP) technique has been proposed to solve radiation problems considering mutual coupling effects between array elements [1]. Based on the AEP, an average active element factor (AEF) with the reduced window array (RWA) approximation is introduced to analyze the plane wave scattering problem of finite arrays on an infinite ground plane [7]. This method changes a large array scattering problem into a superposition of various simplified subarray problems. In [8], an element-varying (EV) AEF method is introduced to analyze normal plane wave scattering patterns of finite arrays on a finite ground plane. From the induced current distribution on an array with odd or even elements, the array is divided into different parts and neglects the weak mutual coupling affected by far elements. In [9] , an improved induced element pattern method (IIEPM) transforms a large finite array problem into two small ones when the normal incidence plane wave is adopted.

In this paper, instead of the case of normal incidence in [8], the scattering of an obliquely incident plane wave from a large finite array is studied with an improved EV-AEF method. Beginning with the induced current distribution in the case of oblique incidence, the whole array elements are divided into relatively small edge combined-elements and interior combined-elements for one-dimensional (1-D) problems. Different from [7], in which exterior equivalent sources are calculated as the incident field to model the edge effects of a finite array, only AEPs of edge combined-elements need to be extracted to

Submitted On: May 11, 2013
Accepted On: December 10, 2014

essentially account for the edge effects in our method. The scattered field from a large finite array with an oblique incident plane wave can be easily calculated by a superposition of the two types of combined-elements in this small array. In addition, the relationship between the current distribution periodicity and incidence angle is analyzed when the oblique plane wave is adopted. To verify the accuracy and efficiency of the proposed method, results of some numerical examples are provided. With the proposed method, therefore, some important features of the radar cross section (RCS) signatures of 1-D and 2-D finite arrays can be examined efficiently.

II. THEORIES

A. Induced current distribution with an oblique plane wave

A 1-D array model illuminated by an oblique plane wave is shown in Fig. 1. In [8] , the induced current density on a 1-D array is symmetrical when the array is illuminated by a normal plane wave. In fact, the induced current density takes on the asymmetric distribution at oblique incidence. Figure 2 plots the induced current density, with FEKO simulation, on four finite arrays of seven, eight, nine, and ten elements, respectively, with the obliquely incident angle of $\theta_0 = 30^0$ and $\varphi_0 = 0^0$.

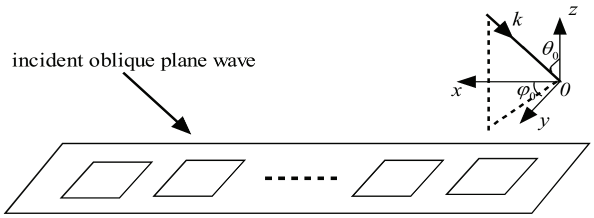

Fig. 1. Obliquely incident plane wave on a 1-D finite array.

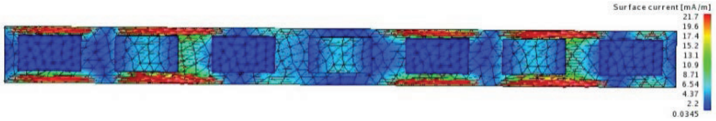

(a) 7-element array

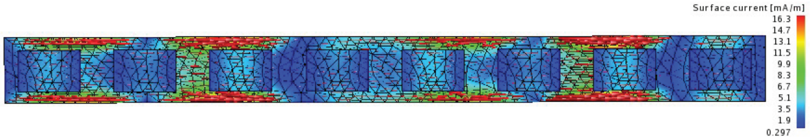

(b) 8-element array

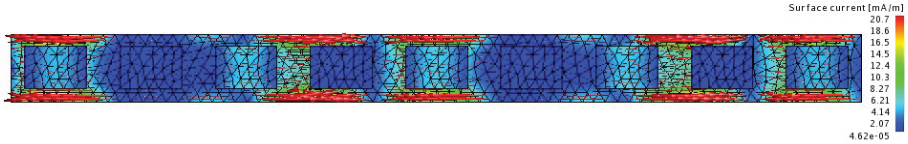

(c) 9-element array

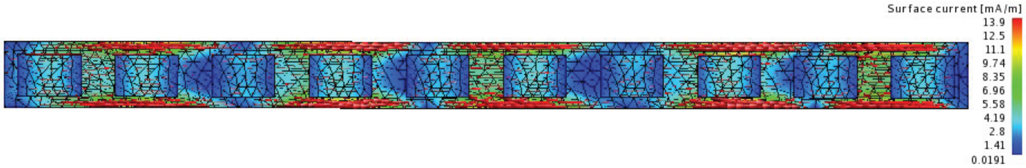

(d) 10-element array

Fig. 2. Current density on 1-D arrays with incident plane wave of $\theta_0 = 30^0$ and $\varphi_0 = 0^0$ (arrows densities denote current densities).

B. Improved EV-AEF method

Based on the EV-AEF method [8] , the far electric field scattered by an array can be expressed as:

$$\boldsymbol{E}_{\text{total}}^{\text{s}} = \sum_{n=1}^{N} \boldsymbol{E}_n^{\text{e}}(\theta,\varphi) e^{\mathrm{j}k\hat{\boldsymbol{r}}\cdot\boldsymbol{r}_n}, \tag{1}$$

where $\boldsymbol{E}_n^{\text{e}}(\theta,\varphi)$ is the AEF field from the *n*th element.

For an oblique plane wave, the concept of combined-element is introduced into the EV-AEF method. A combined-element in Fig. 3 consists of several adjoining elements, and its size is determined by the current distribution periodicity.

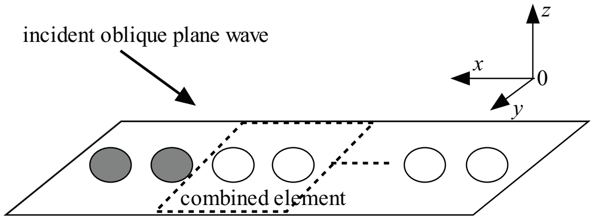

Fig. 3. Combined-element in a 1-D finite array.

Similar to the normal incidence case [8] , only a few neighboring combined-elements are involved in calculating the EV-AEF of a combined-element with an obliquely incident wave. Thus, (1) can be rewritten as:

$$\boldsymbol{E}^{\mathrm{s}}_{\mathrm{total}}(\theta,\varphi)=\boldsymbol{E}_{\mathrm{E}}(\theta,\varphi)+\boldsymbol{E}_{\mathrm{I}}(\theta,\varphi), \tag{2}$$

$$\boldsymbol{E}_{\mathrm{E}}(\theta,\varphi)=\sum_{e=1}^{N_{\mathrm{e}}}\boldsymbol{E}_{e}(\theta,\varphi)e^{\mathrm{j}k\hat{r}\cdot\boldsymbol{r}_{e}}, \tag{3}$$

$$\boldsymbol{E}_{\mathrm{I}}(\theta,\varphi)=\sum_{i=1}^{N_{\mathrm{i}}}\boldsymbol{E}_{i}(\theta,\varphi)e^{\mathrm{j}k\hat{r}\cdot\boldsymbol{r}_{i}}, \tag{4}$$

where $\boldsymbol{E}_{\mathrm{E}}(\theta,\varphi)$ and $\boldsymbol{E}_{\mathrm{I}}(\theta,\varphi)$ are the EV-AEF superposition of all edge combined-elements and of all interior combined-elements, respectively. N_{e} and N_{i} are the amounts of all edge combined-elements and of all interior combined-elements, respectively.

It is noted that, for oblique incident plane wave, only if the resolved component of electric field is along the 1-D array distribution, the periodicity of induced current distribution is observed and our proposed method can be applied to the scattering modeling.

C. Relationship between incident angle and combined-element properties

For the 1-D array illuminated by an oblique plane wave with $\theta_0 = 30^0$ and $\varphi_0 = 0^0$ in Fig. 1, a four-element periodicity of current distribution can be observed in Fig. 2. In the following, how to determine the element number in a current distribution periodicity will be discussed.

When the array is illuminated by an oblique plane wave with $\theta_0 = 30^0$ and $\varphi_0 = 0^0$, as shown in Fig. 4, the phase difference between two adjacent elements is $\Delta\xi = d\sin\theta_0$. When the element spacing $d = \lambda/2$ (λ is the wavelength of plane wave), the phase difference $\Delta\xi=\lambda/4$. Therefore, the phase difference between the 1st element and (N+1)th element is $N\Delta\xi=N\lambda/4$. If N is a multiple of 4, $N\Delta\xi$ will be a multiple of λ. That means that the induced current densities on the 1st element and (N+1)th element have periodic feature.

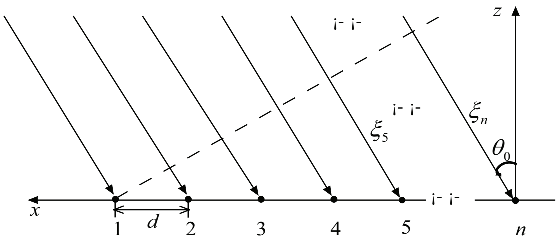

Fig. 4. Phase difference of a 1-D array with an oblique plane wave.

Under the oblique incidence condition, half of elements in a periodicity are chosen to form a combined-element. Thus, when $\theta_0 = 30^0$ and $\varphi_0 = 0^0$, a combined-element consists of two original elements. Figure 5 shows that an 8-element array is divided into edge combined-elements and interior combined-elements. The edge combined-elements fall into two classes: the left one and the right one. And the interior combined-elements also fall into two classes: the odd one and the even one.

For an array at oblique incidence, because the strong mutual coupling only takes place in neighboring combined-elements, the influence of combined-elements far away can be ignored for the EV-AEF calculation of a certain combined-element. Once the EV-AEF of each combined-element in this 8-element model is extracted, the scattering pattern of an arbitrary 4n-element array can be obtained through superposition theory, as shown in Fig. 5.

Similarly, a 9-element array shown in Fig. 6 is used to calculate the scattering pattern of an arbitrary (4n+1)-element array. In the same way, (4n+2)- and (4n+3)-element arrays can also be modeled by using rather small arrays.

Furthermore, when an array is illuminated by oblique plane wave with other angles, for example $\theta_0 = 45^0$ and $\varphi_0 = 0^0$, the phase difference between the 1st element and (N+1)th element is $N\Delta\xi=\sqrt{2}N\lambda/4$. When $N = 14$, this phase difference approximately equals to 5λ , a multiple of the wavelength. Thus, a periodicity of the array involves 14 elements.

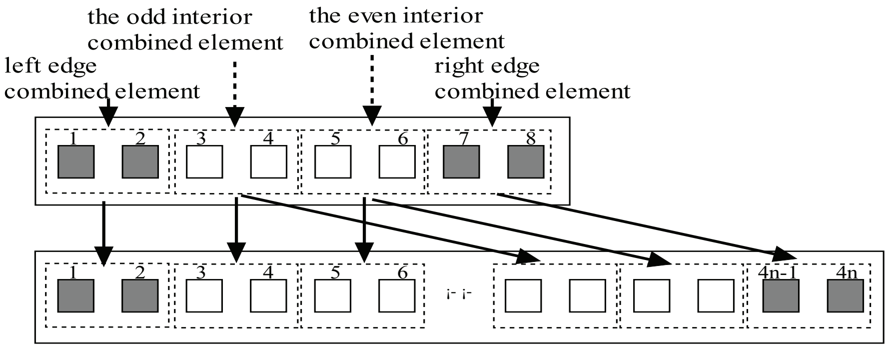

Fig. 5. Illustration of using an 8-element array to calculate a 4*n*-element array.

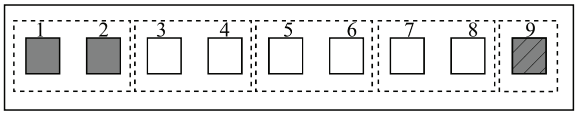

Fig. 6. Combined-elements in a 9-element array with $\theta_0 = 30^0$ and $\varphi_0 = 0^0$.

In general, for a certain incident angle θ_0, if the phase difference between the 1st element and (N+1)th one, $Nd\sin\theta_0$, is a multiple of wavelength λ, the number of elements in a periodicity of the induced current density can be obtained. Since half of elements in a periodicity make up a combined-element, it is required that N has to be an even number. For N=2, 4, 6, … , $Nd\sin\theta_0/\lambda$ is calculated in sequence. Once a calculated result is an integer or very close to an integer, the corresponding N is just the number of elements in a periodicity we want.

III. EXAMPLES AND DISCUSSIONS

A. Far field calculation for 1-D finite arrays

A 1-D 8-element array illuminated by an oblique plane wave with $\theta_0 = 30^0$ and $\varphi_0 = 0^0$ is plotted in Fig. 7. The patch element of array is 26mm × 37mm. The structure parameters are h = 1.58mm and $d = 0.5\lambda_0$, and the relative permittivity of the substrate is chosen as $\varepsilon_r = 2$.

Based on the EV-AEF result of each combined-element in the 8-element subarray, the scattered fields of 24- and 100-element arrays are shown in Figs. 8 (a) and (b), respectively. The results show that the scattered fields with the improved EV-AEF method closely match those with the whole-array simulation in FEKO.

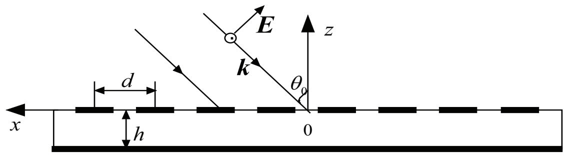

(a) Side view

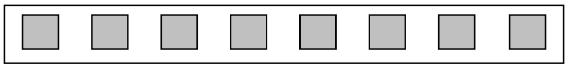

(b) Top view

Fig. 7. 8-element array illuminated by an oblique plane wave.

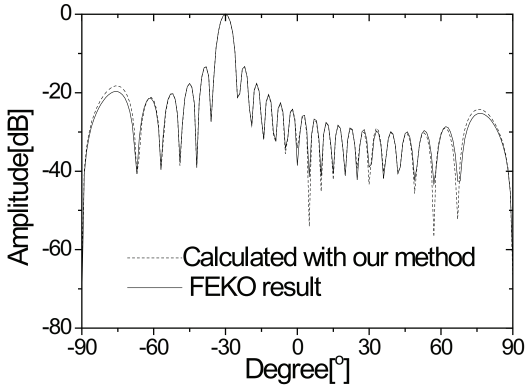

(a) 24-element array

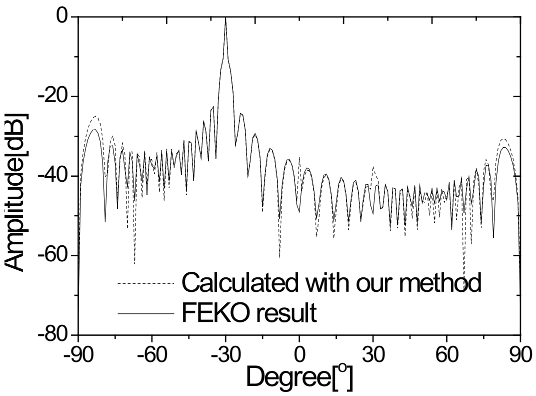

(b) 100-element array

Fig. 8. Scattered fields with the EV-AEF method and FEKO's simulation.

For a (4*n*+1)-element array with an oblique wave of $\theta_0 = 30^0$ and $\varphi_0 = 0^0$, a 9-element subarray is required to calculate the scattered field. Figure 9 plots the scattered fields of a 101-element array whose parameters are the same as that in Fig. 7. The results of scattered field with the improved EV-AEF method and the whole-array FEKO simulation are in good agreement.

Table 1 presents the comparison of computing time between the proposed method and FEKO's simulation. The proposed method shows a significant improvement in computational efficiency. All calculations are performed on a computer with a Dual-Core 2.93 GHz CPU and 2.0 GB RAM.

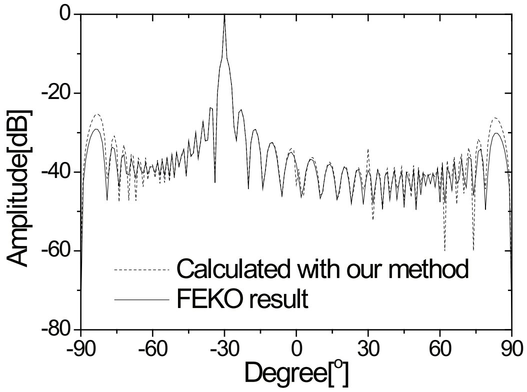

Fig. 9. Scattered fields with the EV-AEF method and FEKO's simulation.

Table 1: Comparison of computing time between the EV-AEF and FEKO's simulation

n-Element Array	*n* = 24		*n* = 100		*n* = 101	
Method	EV-AEF	FEKO	EV-AEF	FEKO	EV-AEF	FEKO
Subarray simulation (s)	4.97	------	4.97	------	7.13	------
Pattern superposition (s)	0.15	------	0.19	------	0.19	------
Total time (s)	5.12	50.02	5.16	5720.94	7.32	7082.52

B. Far feld calculation for 2-D finite array

In order to further prove the validity of the proposed method for computing 2-D finite arrays, an (8×8)-element array illuminated by an oblique plane wave with $\theta_0 = 30^0$ and $\varphi_0 = 0^0$, as shown in Fig. 10, is analyzed. The material and the element parameters are the same as the 1-D 8-element array in Fig. 6. The induced current distribution on the array surface is related to the polarization direction of obliquely incident wave. Along one resolved component of electric fields, *x*-direction in Fig. 10, the current distribution of a 2-D array is with the same regularity of that of a 1-D array. Along the non-polarization direction, the current distribution is dependent of the array environment and does not have periodic feature. The 2-D array elements can be divided into the corner combined-elements, edge combined-elements and interior combined-elements, respectively, as shown in Fig. 10.

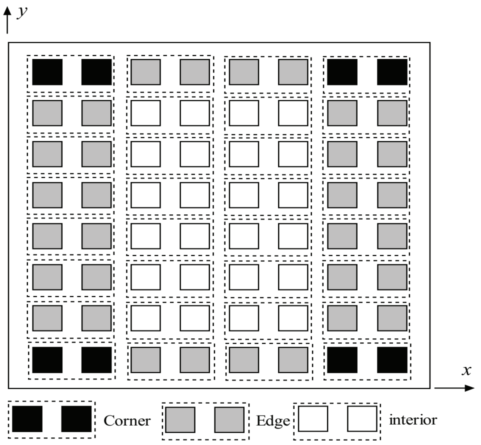

Fig. 10. Combined-elements in a 2-D (8 × 8)-element array.

An (8×3)-element subarray is required to calculate the type of $(4n \times n)$-element arrays. Figure 11 illustrates the scattered fields for the (8 × 8)-element array using the EV-AEF method and whole-array simulation in FEKO.

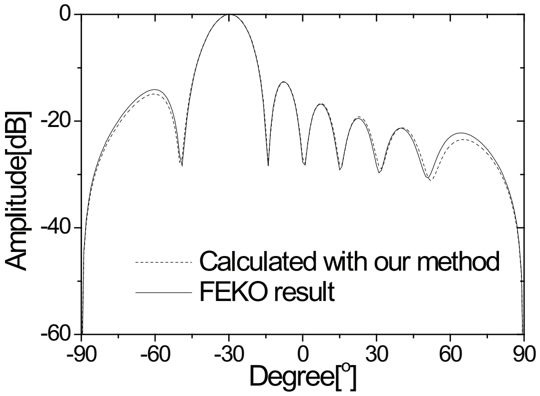

Fig. 11. Scattered fields for 2-D (8 × 8)-element array.

Table 2 shows that the proposed method for the 2-D (8×8)-element array gets a significant improvement in computational efficiency compared to whole-array simulation in FEKO.

Table 2: Comparison of computing time between our method and whole-array simulation

Approach	EV-AEF	FEKO
Subarray simulation (s)	102.16	-------
Pattern superposition (s)	0.17	-------
Total time (s)	102.33	5054.31

IV. CONCLUSION

In this paper, an improved EV-AEF method for calculating scattering patterns from a large finite array at oblique incidence is proposed. The relationship between incident angle of plane wave and combined-element properties is discussed. In order to validate the proposed method, numerical examples of 1-D and 2-D arrays are calculated. The results show that the improved EV-AEF method leads to the much faster solution than the whole-array simulation with good accuracy.

In addition, this work can also extend to non-regular or conformal arrays. Taking a thinned array which is thinned from a full array with the regular lattice of N positions spaced by a uniform distance for example, its element states (positions with element or without element) are unknown and there are a variety of possibilities. For a certain element in the thinned array, the distributions of its neighboring elements are various. Therefore, extracting the AEPs of all element combinations is indispensable.

ACKNOWLEDGMENT

This work is supported in part by the National Natural Science Foundation of China (61271025, 61331007 and 61471105).

REFERENCES

[1] R. F. Harrington, *Field Computation by Moment Methods*, Macmillan, New York, 1968.

[2] J. M. Jin, *The Finite Element in Electromagnetics*. Wiley, New York, 1993.

[3] A. Taflove and S. C. Hagness, *Computational Electrodynamics: The Finite-Difference Time-Domain Method*, 2nd edition. Artech House, Boston, 2000.

[4] F. Xu, Y. Zhang, W. Hong, K. Wu, and T-J. Cui, "Finite-difference frequency-domain algorithm for modeling guided-wave properties of substrate integrated waveguide," *IEEE Trans. Microw. Theory Tech*., vol. 51, no. 11, pp. 2221-2227, 2003.

[5] H. Bahadori, H. Alaeian, and R. Faraji-Dana, "Computation of periodic Green's functions in layered media using complex images technique," *Progress in Electromagnetics Research*, vol. 112, pp. 225-240, 2011.

[6] D. M. Pozar, "The active element pattern," *IEEE Trans. Antennas Propag*., vol. 42, no. 8, pp. 1176-1178, 1994.

[7] F. J. Villegas, Y. Rahmat-Samii, and D. R. Jackson, "Scattering characteristics of finite arrays of cylindrical cavities in an infinite ground plane," *IEEE Trans. Antennas Propag*., vol. 51, no. 9, pp. 2381-2391, 2003.

[8] Q. Li, W. Shao, and H. Li, "Scattering pattern calculation for large finite arrays using the element-varying active element factor method," *Applied Computational Electromagnetics Society Journal*, vol. 26, no. 11, pp. 893-898, 2011.

[9] S. Zhang, S. Gong, Q. Gong, Y. Guan, and B. Lu, "Application of the active element pattern method for calculation of the scattering pattern of large finite arrays," *IEEE Antennas Wireless Propag. Lett*., vol. 10, pp. 83-86, 2011.

Wei Shao received the M. Sc. and Ph. D. degrees in Radio Physics from the University of Electronic Science and Technology of China (UESTC), Chengdu, China, in 2004 and 2006, respectively. He joined the UESTC and is now an Associate Professor there. He has been a Visiting Scholar in the Electromagnetic Communication Laboratory, Pennsylvania State University in 2010. His research interests include the computational electromagnetics and antenna technique.

Jia-Lin Li received the M. Sc. degree from UESTC, Chengdu, China, in 2004, and the Ph. D. degree from the City University of Hong Kong, Hong Kong, in 2009, both in Electronic Engineering. Since Sept. 2009, he has been with the Institute of Applied Physics, School of Physical Electronics, UESTC, where he is currently a Professor. His research interests include the high performance active/passive microwave/millimeter-wave antennas, circuits and systems realized on PCB, multilayer PCB, LTCC, etc.

Qifei Li received the B. E. degree in Chengdu University of Information Technology, Chengdu, China, in 2006. From 2009 to now, she is pursuing the M. Sc. degree in the Institute of Applied Physics at UESTC, Chengdu, China. Her current research interests include the antenna radiation and array scattering.

Dual-Band Active Integrated Antenna with Electronically Controllable for S-Band Applications

Jasem Jamali [1], Masoud Ahmadi [2], Jalil Mazloum [3], Mohammad Ojaroudi [4]

[1] Department of Electrical Engineering
Kazerun Branch, Islamic Azad University, Kazerun, Iran

[2] Faculty of Electrical & Computer Engineering
Shahid Beheshti University, Tehran, Iran

[3] Faculty of Electrical Engineering
Shahid Sattari Aeronautical University of Science and Technology, Tehran, Iran

[4] Young Researchers and Elite Club, Ardabil Branch
Islamic Azad University, Ardabil, Iran
m.ojaroudi@iauardabil.ac.ir

Abstract **─** A novel reconfigurable active feedback antenna for WiMAX/WLAN applications is presented. By using an H-shaped radiating patch with a pair of C-shaped slots in the active feedback antenna, two new resonances can be achieved. Also, the proposed radiating patch has a major advantage in providing tighter capacitive coupling to the line in comparison to known radiating patch. In order to generate DC isolation in the RF path, we use a pair of gap distances in the microstrip loop. Also, by using the [S] parameters of the active element, a novel design of the microwave oscillator is performed. Simulated and experimental results obtained for this antenna show that the proposed Active Integrated Antenna (AIA) has a good return loss and radiation behavior within the WiMAX/WLAN frequency range.

Index Terms **─** C-shaped slot, H-shaped radiating patch, Reconfigurable Active Integrated Antenna (RAIA), WiMAX/WLAN systems.

I. INTRODUCTION

In the last few years, there have been rapid developments in various antenna designs for wireless local area network (WLAN) and worldwide interoperability for microwave access (WiMAX) applications. These antennas include the planar inverted-F antennas (PIFAs) [1], printed patch antenna [2], the CPW-fed antennas [3], and the planar monopole antennas [4]. However, up to now, a printed antenna that has T-shaped notch configuration has not been reported.

It is a well-known fact that, active feedback presents really appealing physical features, such as simple structure, small size, and low cost. Because of all these interesting characteristics, multi-band low noise amplifier is expected to become a key device for the next generation of multi-band and multi-mode wireless radios [5], and growing research activity is being focused on them [6-8]. Various switching based techniques have been proposed to achieve multi-band performance. Some of the topologies use separate oscillators [5] to obtain multi-band response, while others use distinct resonators [6] or matching networks [7] to achieve the same.

In this paper, we propose a novel frequency reconfigurable active integrated antenna with the capability to switch between WLAN and WiMAX modes. The antenna which uses a switchable slotted structure for reconfigurability, has a simple structure and smallest size in comparison to antennas reported in literature [1]-[4]. In the proposed structure, based on electromagnetic coupling (EC), an H-shaped radiating patch with a

Submitted On: April 14, 2013
Accepted On: September 5, 2014

pair of C-shaped slots in the active feedback antenna is used to perturb two resonance frequencies at 2.4 GHZ (WLAN) and 3.5 GHz (WiMAX). This structure has a major advantage in providing tighter capacitive coupling to the line in comparison to known radiating patch [9]. The proposed antenna has three different switchable states: 2.25-10.72 GHz in WLAN mode, 3.34-3.71 GHz in WiMAX mode, and 1.65-1.89 GHz in narrowband mode. Also, the implemented dual-band low noise amplifier exhibited output power level of 12.84 dB at frequency of 2.4 GHz and 10.94 dB at frequency of 3.49 GHz, for various diodes bias conditions.

II. RECONFIGURABLE ANTENNA DESIGN

The proposed passive antenna fed by a 50-Ω feed line is shown in Fig. 1, which is printed on a FR4 substrate of thickness 0.8 mm and permittivity 4.4. The numerical and experimental results of the input impedance and radiation characteristics are presented and discussed. The Ansoft simulation software high-frequency structure simulator (HFSS) [10] is used to optimize the design and agreement between the simulation and measurement is obtained.

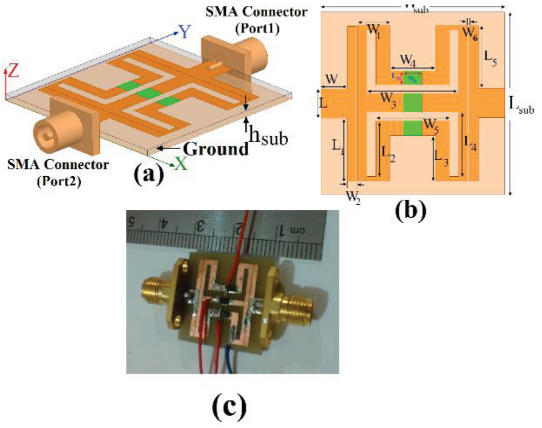

Fig. 1. Configuration of the switchable antenna: (a) side view, (b) top view, and (c) fabricated scheme.

To design a novel reconfigurable antenna, three pin diodes are inserted in the radiating patch of the proposed antenna as displayed in Fig. 1. Three states with different conditions of diodes are specified in Table 1 as states 1, 2 and 3. Figure 2 shows simulated and measured return loss characteristics for the proposed antenna in three states 1, 2, and 3 with pin diodes as depicted in Table 1. As depicted in Fig. 2, in this structure, the H-shaped radiating patch with a pair of C-shaped slots with three p-i-n diodes is used in order to electronically switch between the WLAN (2.4 GHz) and WiMAX (3.45 GHz) frequency bands. Also, when the central diode is biased and the others are off, the proposed antenna has not any radiation performance in the S-band. In addition, this structure has a major advantage in providing tighter capacitive coupling to the line in comparison to known radiating patch [2]. In the proposed configuration, a pair of gap distances are playing an important role in the radiating characteristics of this antenna, because it can adjust the electromagnetic coupling effects between the H-shaped radiating patch and the microstrip transmission line [4].

Table 1: Three states of proposed antenna with different conditions for pin diodes

State	D1	D2	D3
1	On	Off	On
2	On	On	On
3	Off	On	Off

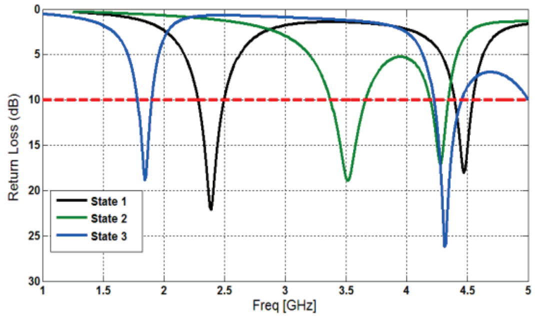

Fig. 2. Simulated return loss characteristics for the passive microstrip antenna with various states of diodes.

The optimal dimensions of the designed passive antenna are as follows: W_{sub}=20 mm, L_{sub}=20 mm, h_{sub}=0:8 mm, W=4 mm, L=1.5 mm, W_1=3 mm, L_1=7 mm, L_2=4 mm, W_2=0.85 mm, L_3=3 mm, W_3=8 mm, L_4=4 mm, W_4=4 mm, L_5=7 mm, W_5=6 mm, W_6=0.15 mm, W_P=2 mm, and L_P=1 mm.

For applying the DC voltage to PIN diodes, metal strips with dimensions of 2 mm × 0.6 mm were used inside the main slot. Moreover, for each PIN diode a 100 pF DC blocking capacitor was placed in the slot to create the RF connection of the

PIN diode and also to isolate the RF signal from the DC. In the introduced design, HPND-4005 beam lead PIN diodes [11] with extremely low capacitance were used. For biasing PIN diodes a 0.7 volts supply is applied to metal strips. The PIN diodes exhibit an ohmic resistance of 4.6 Ω and capacitance of 0.017 pF in the on and off states, respectively. By turning diodes on, the metal strips are connected to the ground plane and become a part of it. Therefore, a part of the slot is short-circuited, and the corresponding resonance is eliminated due to the change in main slot's length. The desired frequency band can be selected by varying the states of PIN diodes which changes the total equivalent length of the slot.

In order to understand the phenomenon behind switching electronically between WLAN and WiMAX resonance frequency, the simulated current distributions on the radiating patch of the proposed antenna for on and off statuses of the p-i-n diodes, are presented in Figs. 3 (a), (b) and (c), respectively. As shown in Fig. 3 (a), at the WLAN resonance frequency (2.4 GHz) the current mainly concentrates on the C-shaped strips edges, and also it can be seen that the electrical current does change its direction along these strips. In addition, the current mainly concentrates on the central strip at the WiMAX resonance frequency (3.5 GHz), as shown in Fig. 3 (b).

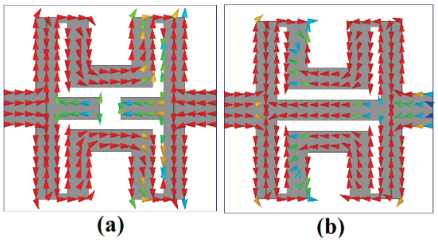
(a) **(b)**

Fig. 3. Simulated surface current distributions on the radiating patch for the proposed antenna shown in Fig. 1: (a) state 1 at 2.4 GHz, and (b) state 2 at 3.5 GHz.

III. RECONFIGURABLE LOW NOISE APMLIFIER DESIGN

Transistor low noise amplifier can be designed using either bipolar or GaAs MESFET devices [12-13]. In order that the amplifier delivers a maximum power to the load, it must be properly terminated at output port to a resistor [14-15]; hence, the need of an input/output matching circuit arises. A short and efficient CAD procedure for the design of reconfigurable dual-band microstrip amplifier is performed. It is based on the scattering-matrix parameters of the active element. The CAD procedure has mainly two steps. The first step is the design of a narrowband high-gain amplifier operating at the first frequency of 2.4 GHz, and the developed full-scale simulation program is used for stability consideration and analytical design of the input and output matching circuits [13]. The second step is to design lengths and widths of the second input and output matching circuits so as to get a narrowband high-gain amplifier operating at the second frequency of 3.5 GHz. Using the [S] parameters of the active element, the design of the microwave amplifier is performed using our full-scale computer simulation program. First, the stability of device can be checked by two stability factors K and |Δ|. The mathematical equations for K and |Δ| are [14]:

$$\Delta = S_{11}S_{22} - S_{21}S_{12}\,, \tag{1}$$

$$K = \frac{1 - |S_{11}|^2 - |S_{22}|^2 + |\Delta|^2}{2|S_{21}S_{12}|}\,. \tag{2}$$

The stability of the used ATF 13786 GaAs transistor at the frequencies of 2.4 GHz and 3.5 GHz is calculated through calculation of the stability factor, K and Δ [15]. The transistor is potentially unstable at the operated frequencies 2.4 GHz and 3.5 GHz (i.e., K=0.5718 and K=0.656, respectively).

The matching networks are designed to get minimum reflection coefficient at the transistor input and output. The analytical design of the terminating circuit and the output matching circuit are performed using the developed computer program [14]. In this design, the input and output matching circuits are designed to transfer the calculated Z_{MS}* and Z_{ML}* to 50 Ω. The input and output matching circuits can be designed using two-section matching circuits (a series transmission line and an open/short single/balanced shunt stub). The analytical design procedure of the matching circuits is as follows:

$$\Gamma_{MS} = \frac{B_1 - \sqrt{B_1^2 - 4C_1^2}}{2C_1}\,, \tag{3}$$

$$\Gamma_{ML} = \frac{B_2 - \sqrt{B_2^2 - 4C_2^2}}{2C_2}\,, \tag{4}$$

$$B_1 = 1 + |S_{11}|^2 - |S_{22}|^2 - |\Delta|^2\,, \tag{5}$$

$$B_2 = 1 + |S_{22}|^2 - |S_{11}|^2 - |\Delta|^2, \quad (6)$$

$$C_1 = S_{11} - conj(S_{22}).\Delta, \quad (7)$$

$$C_2 = S_{22} - conj(S_{11}).\Delta, \quad (8)$$

$$G_{T\max} = \frac{1}{1-|\Gamma_S|^2}|S_{21}|^2\frac{1-|\Gamma_L|^2}{|1-S_{22}\Gamma_L|^2}, \quad (9)$$

$$Z_{in} = Z_0\frac{1-|\Gamma_S|^2+2j|\Gamma_S|\sin(\theta_{\Gamma_S})}{1+|\Gamma_S|^2-2|\Gamma_S|\mathrm{cose}(\theta_{\Gamma_S})}, \quad (10)$$

$$Z_{Out} = Z_0\frac{1-|\Gamma_L|^2+2j|\Gamma_L|\sin(\theta_{\Gamma_L})}{1+|\Gamma_L|^2-2|\Gamma_L|\cos(\theta_{\Gamma_L})}, \quad (11)$$

$$Y_{in} = \frac{1}{Z_{in}}, \quad (12)$$

$$Z_{o1} = \frac{1}{|imag(Y_{in})|}, \quad (13)$$

$$Z_{o2} = \sqrt{\frac{Z_0}{|\mathrm{Re}(Y_{in})|}}, \quad (14)$$

$$Y_{Out} = \frac{1}{Z_{out}}, \quad (15)$$

$$Z_{o3} = \frac{1}{|imag(Y_{Out})|}, \quad (16)$$

$$Z_{o4} = \sqrt{\frac{Z_0}{|\mathrm{Re}(Y_{Out})|}}. \quad (17)$$

A prototype reconfigurable LNA circuit was designed on a FR4 substrate with 0.8 mm thickness for wireless applications. Microstrip lines were used for the input and output matching network, rather than utilizing lumped elements to minimize overall insertion losses. By tuning the length of the microstrip lines, the circuits operate at a different frequency. A schematic diagram of the reconfigurable LNA design is shown in Fig. 4 with the lumped elements, such as capacitors and resistors and the transistor's position. Figure 5 shows hard-wire connected reconfigurable LNA configured at 2.4 GHz which can also be reconfigured to operate at 3.5 GHz. Amplifier biasing circuit passive part is fabricated with available microstrip materials (FR4) using wet etching technique, active part is soldered on the passive substrate. The input and output ports are matched to 50-ohm transmission line, which is a microstrip line with 1.5 mm width. Some pads should be grounded and therefore there are some connections to the reference ground plane using via that is shown in the layout with dark gray circles. The conductive connections inside these holes are made by punching some metallic bars in the holes and soldering them to each face of the board.

Simulated S-parameters results for the proposed LNA for WLAN application at 2.4 GHz, and WiMAX applications at 3.5 GHz are shown in Fig. 6 and Fig. 7, respectively. All design steps for matching networks, stability, and DC biasing were done using schematic wizard of Advanced Design System (ADS) by Agilent Technologies [18] using the model provided by CEL for that transistor.

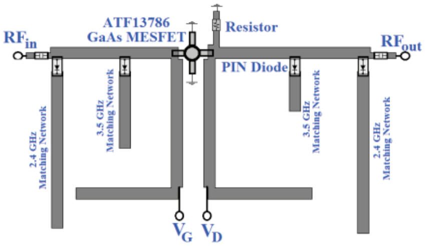

Fig. 4. Reconfigurable LNA concept diagram with two various matching stubs to operate at 2.4GHz and 3.5 GHz.

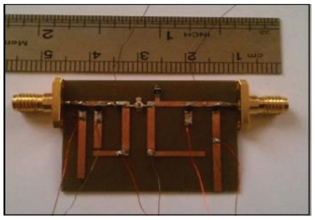

Fig. 5. Fabricated reconfigurable LNA configured at 2.4 GHz which can also be reconfigured to operate at 3.5 GHz.

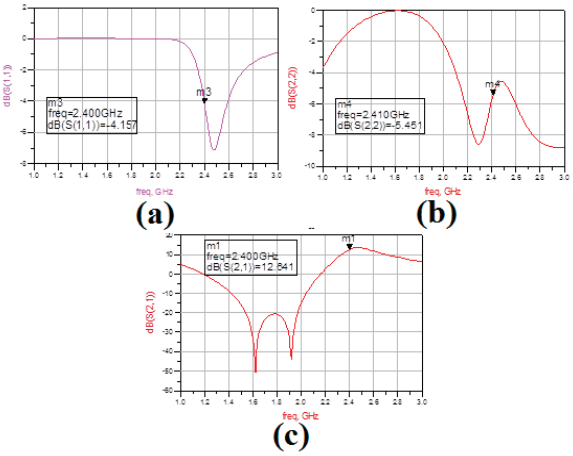

(a) (b) (c)

Fig. 6. Simulated results for the proposed LNA for WLAN application at 2.4 GHz: (a) S_{11}, (b) S_{22}, and (c) S_{21}.

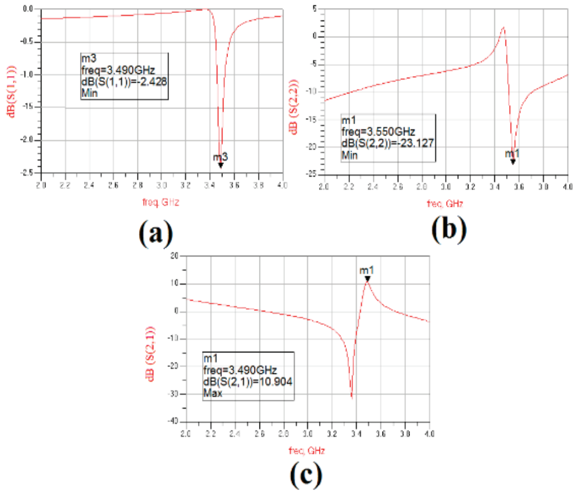

Fig. 7. Simulated results for the proposed LNA for WiMAX application at 3.5 GHz: (a) S_{11}, (b) S_{22}, and (c) S_{21}.

IV. RECONFIGURABLE ACTIVE INTEGARTED ANTENNA

The presented active feedback antenna is shown in Fig. 8, which is printed on an FR4 substrate of thickness 0.8 mm, permittivity 4.4, and loss tangent 0.018. The proposed active feedback antenna structure consists of a rectangular ring with a pair of protruded Γ-shaped strips for radiating element, a microstrip loop, and an oscillator with DC bias circuit and matching circuit for active part. The width of the 50-Ω microstrip line is fixed at 1.5 mm, as shown in Fig. 6. The matching circuit to the left and right of the device controls the coefficient of feedback. On the other side of the substrate, a conducting ground plane is placed. In addition, to satisfy the oscillation-phase requirement, the microstrip loop is fixed to a suitable electrical length, taking the calculated phases of the oscillator and passive antenna into consideration [16].

Figure 9 shows the measured return loss characteristics for the active antenna in comparison of simulated return loss characteristics for the passive microstrip antenna with various states of diodes. The fabricated antenna satisfies the 10-dB return loss requirement within the WiMAX/WLAN frequency range. However, as shown in Fig. 9, there exist a discrepancy between measured data and the simulated results. This discrepancy is mostly due to a number of parameters, such as the fabricated antenna dimensions as well as the thickness and dielectric constant of the substrate on which the antenna is fabricated, the wide range of simulation frequencies and also the effect of pin diode and its biasing circuit.

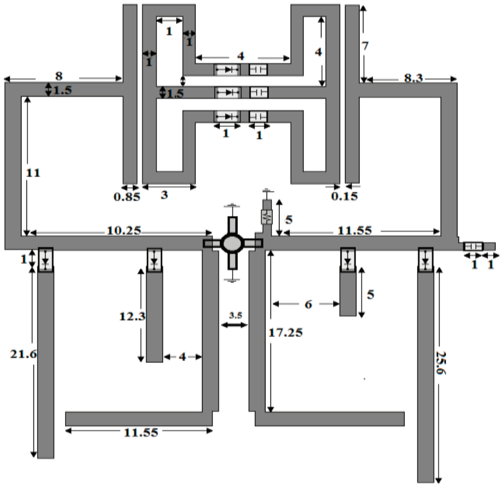

Fig. 8. Configuration of the proposed active integrated antenna (unit: mm).

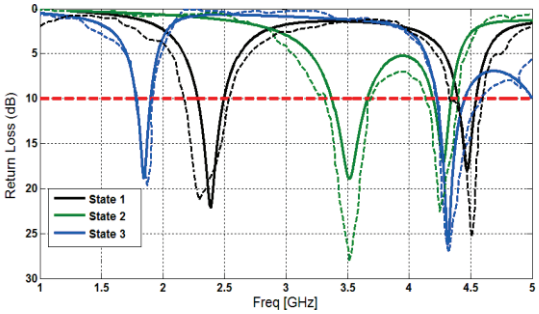

Fig. 9. Measured return loss characteristics for the active antenna in comparison of simulated return loss characteristics for the passive microstrip antenna with various states of diodes (dashed line: measured, solid line: simulated).

The simulated radiation patterns including the co-polarization and cross-polarization for the E-plane (y-z plane) and H-plane (x-z plane) at the resonance frequencies are shown in Fig. 10. The simulated radiation patterns are calculated by using the gap-source technique with the commercial EM simulator HFSS, considering the complete active feedback antenna which has same layout, except with an active transistor [3]. The received cross-polarizations in the E-plane and H-plane of the AIA are approximately 17 and 14 dB lower than the maximum co-polarized radiation, respectively. As seen in Fig. 10, the radiation pattern in the H-plane is asymmetrical, due to the asymmetrical presence of the distributed oscillator-feedback circuitry. The designed feedback-antenna oscillator has stable oscillation. The obtained gain by the amplifier is of 11.2 dB.

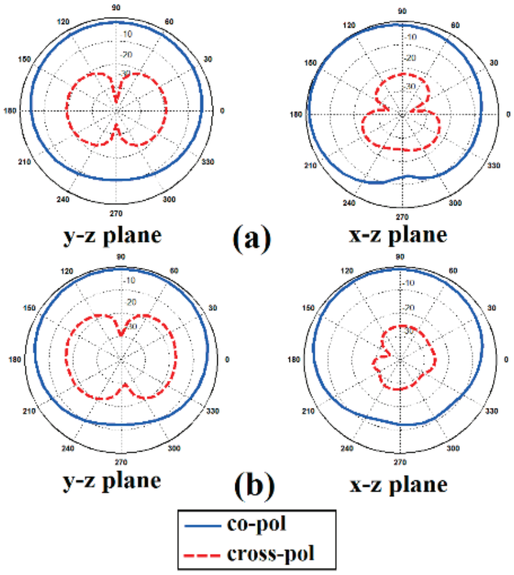

Fig. 10. Simulated radiation patterns of the proposed active integrated antenna.

V. CONCLUSION

As presented above, a novel design of reconfigurable active integrated antenna with electronically controllable is an interesting subject for for WiMAX/WLAN applications. By using an H-shaped radiating patch with a pair of C-shaped slots in the active feedback antenna, two new resonances can be achieved. The proposed antenna has three different switchable states: 2.25-2.72 GHz in WLAN mode, 3.34-3.71 GHz in WiMAX mode, and 1.65-1.89 GHz in narrowband mode. The LNA design based on the AIA concept has been shown to provide an efficient and successful method for designing high efficiency and compact systems. The implemented dual-band low noise amplifier exhibited output power level of 12.84 dB at frequency of 2.4 GHz and 10.94 dB at frequency of 3.49 GHz, for various diodes bias conditions.

REFERENCES

[1] F. R. Hsiao and K. L. Wong, “Compact planar inverted-F patch antenna for triple-frequency operation,” *Microwave Opt. Technol. Lett.*, 33, 459-462, 2002.

[2] J. Lu and H. Chin, “Planar compact U-shaped patch antenna with high-gain operation for Wi-Fi/WiMAX application,” *Applied Computational Electromagnetics Society (ACES) Journal*, vol. 26, no. 1, pp. 82-86, January 2011.

[3] S. Bashiri, C. Ghobadi, J. Nourinia, and M. Ojaroudi, “CPW-fed slot-like sleeve monopole antenna with bandwidth enhancement for UWB wireless communications,” *ACES Journal*, vol. 28, no. 9, pp. 815-820, 2013.

[4] M. Ojaroudi and E. Mehrshahi, “High accuracy time domain modeling of microstrip discontinuities by using modified TDR based on barker codes with flat spectrum and integrated side-lobes,” *ACES Journal*, vol. 28, no. 5, pp. 374-379, May 2013.

[5] K. Chang, “Active integrated antennas,” *Proc. IEEE*, vol. 50, no. 3, March 2002.

[6] P. S. Hall, P. Gardner, and G. Ma, “Active integrated antenna,” *IEICE Trans. Commun.*, E85-B, (9), pp. 1661-1666, 2002.

[7] M. Ojaroudi and N. Ojaroudi, “Ultra-wideband small rectangular slot antenna with variable band-stop function,” *IEEE Transactions on Antenna and Propagation*, vol. 62, no. 1, pp. 490-494, January 2014.

[8] G. Yun, “Compact oscillator-type active antenna for UHF RFID reader,” *Electronic Letters*, vol. 43, no. 6, March 2007.

[9] A. Faraghi, M. N. Azarmanesh, and M. Ojaroudi, “Small microstrip low-pass filter by using novel defected ground structure for UWB applications,” *Applied Computational Electromagnetics Society (ACES) Journal*, vol. 28, no. 4, pp. 341-347, April 2013.

[10] Ansoft High Frequency Structure Simulation (HFSS), ver. 13, Ansoft Corporation, 2010.

[11] HPND-4005, “Beam lead PIN diode,” Avago Technologies.

[12] K. Chang, “Active integrated antennas,” *Proc. IEEE*, vol. 50, no. 3, March 2002.

[13] P. S. Hall, P. Gardner, and G. Ma, “Active integrated antenna,” *IEICE Trans. Commun.*, E85-B, (9), pp. 1661-1666, 2002.

[14] M. Ojaroudi and E. Mehrshahi, “Bandwidth enhancement of small square monopole antennas by using defected structures based on time domain reflectometry analysis for UWB applications,” *ACES Journal*, vol. 28, no. 7, pp. 620-627, July 2013.

[15] E. M. Biebl, “Millimeter wave systems based on active integrated antennas,” *Antennas and Propagation Millenium Conference, European Space Agency*, Davos, 2000.

A Novel Multi-Band Polarization Insensitive Frequency Selective Surface Based on Centrosymmetric L-Shaped Metal Strips

Yun Lin [1], Xiaochun Xu [1], Zheng Dou [1], Xiaoxin Liu [2], and Guohui Yang [2]

[1] College of Information and Communication Engineering
Harbin Engineering University, Harbin, 150001, China
douzheng@hrbeu.edu.cn

[2] School of Electronics and Information Engineering
Harbin Institute of Technology, Harbin, 150001, China
gh.yang@hit.edu.cn

Abstract **─** In this paper, a novel frequency selective surface (FSS) based on rotationally symmetric bended microstrips is investigated. The unit element consists of twelve L-shaped metal strips and a dielectric substrate. Bended L-shaped strips have different equivalent electric lengths corresponding to different resonant frequencies, which result in multi-band frequency characteristic. Meanwhile, the symmetric metal strips make the FSS polarization insensitive. The numerical experiments demonstrate that the FSS structure has fifteen stop-bands in the frequency band from 6 GHz to 20 GHz, and a good polarization stability as well. Moreover, the FSS design such as the inner radius of L-shaped metal strips, the dimensions of dielectric substrate and the width of the bended metal strips significantly effects on the FSS performance. Because of the multi-band property, the FSS designed in this paper has a bright prospect in many modern wireless communication systems and even in 5G communication system in the future.

Index Terms **─** Centrosymmetric bended micrstrip, FSS, multi-band, polarization insensitive.

I. INTRODUCTION

Frequency selective surfaces (FSSs) are usually constructed by using a two-dimensional periodic metallic patterns combined with dielectric substrates [1, 2]. Generally, FSSs can be classified into two categories: (1) dipole array FSS, and (2) slot array FSS, and the former exhibits band-stop characteristic while the later exhibits band-pass characteristic. FSSs have been widely used as spatial filters to totally reflect or just transmit electromagnetic waves in some specified frequency bands [3]. FSSs can be applied in antenna radome, filter, radar cross section (RCS) reduction, directivity enhancement and dichroic sub-reflector. Theoretically, FSS is an infinite array with a periodic structure; however, it is always finite in practical applications. The truncation of the infinite period structure will change the FSS performance, which makes it necessary to utilize sufficient elements to keep the characteristics of infinite FSS [4].

One of the important FSS applications is to work as sub-reflectors for the satellite communication so that a single main reflector can cover the different frequency bands [5, 6]. To enhance the capability of multi-frequency and multi-function antennas, a sub-reflector integrated with FSS is operated normally at multi-band frequencies; meanwhile, FSS is polarization insensitive in multi-bands [7]. In addition, the increasing demands on multi-functionality of antennas for communications also require multi-band polarization insensitive FSSs. To design multi-band insensitive polarization FSS, some ideas such as gradient variation structure and fractal shape are proposed [8, 9]. However, the transmission of gradient variation structure FSS is usually not low enough in stop-bands, while the number of stop-bands of a fractal shape FSS is

Submitted On: February 27, 2014
Accepted On: January 3, 2015

tightly restricted within three. Moreover, most existing multi-band FSSs are sensitive to polarization.

The modern wireless communication system is developing to multi-standard and multi-system, which requires the radio frequency filter in the system to have multi-band function in many cases. In this paper, a novel multi-band polarization insensitive FSS is designed, which has the top layer composed of twelve centrosymmetric bended metal strips. Because rotationally symmetric bended metal strips can resonate at different frequencies, the FSS had fifteen stop-bands in the frequency band from 6 GHz to 20 GHz for both TE and TM wave. In addition, FSS is only 2 mm in thickness, which grants the FSS broad application prospects in fabricating sub-reflector due to its light weight and low cost. And owing to its multi-band property, the FSS designed in this paper could be used in modern wireless communication system and even 5G communication system in the future. Moreover, the pass-bands and stop bands can be easily changed by changing the geometry size of the FSS, which makes the FSS more promising in application.

II. FSS STRUCTURE AND ANALYSIS

A. Basic multi-band polarization insensitive FSS design

A multi-band polarization insensitive FSS with a simple configuration is designed in this section whose unit cell is shown in Fig. 1. The top layer of the FSS is composed by four bended metal strips whose length is $a = 10.0$ mm, width is $w = 1.0$ mm and thickness is 0.035 mm. Two of the metal strips are put in horizontal, while the other two are put in vertical to ensure the FSS polarization insensitive. The spacing between two metal strips is $d = 8.0$ mm. The length of the dielectric substrate is $A = 30.0$ mm and its thickness is $D = 2.0$ mm. The relative permittivity of substrate slab is $\varepsilon_r = 2.2$.

In order to simulate the infinite periodic array of FSS accurately, periodic boundary conditions (PBC) are utilized to top, bottom, left and right boundaries, while open (add space) boundary conditions are utilized to front and back boundaries of the unit cell in electromagnetic (EM) simulation software CST MICROWAVE STUDIO 2012. Frequency domain solver and tetrahedral mesh are used to make the simulation. And for the purpose of getting accurate simulation results, high initial mesh density and adaptive tetrahedral mesh refinement are utilized during the simulation. The transmission of the FSS for TE and TM incident waves is plotted in Fig. 1. The frequency band with transmission of higher than -3 dB is called as a pass-band while that with transmission of lower than -10 dB is defined as a stop-band. It can be seen from Fig. 1, that the FSS has six stop-bands and seven pass-bands in the frequency band from 6 GHz to 20 GHz and has the same responses for TE and TM wave. However, the number of pass-bands is not great enough and some frequency spaces of adjacent pass-bands are too narrow.

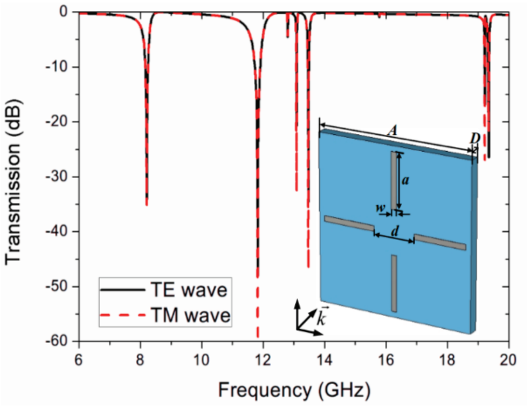

Fig. 1. Transmission coefficients and configuration of the basic FSS unit cell.

B. Improved multi-band polarization insensitive FSS design

In purpose of increasing the pass-bands number and reasonably arranging the frequency spaces of adjacent pass-bands. An improved multi-band polarization insensitive FSS based on centrosymmetric fold lines is proposed in this section, whose configuration is illustrated in Fig. 2. In detail, centrosymmetric L-shaped metal strips are used in the FSS unit cell. According to the electromagnetic wave theory, the resonant frequency of the metal unit cell is relevant to its size, which means the FSS could resonate in case that the total effective length of the unit cell is roughly equal to the wavelength λ of the incident electromagnetic wave. It can be seen from Fig. 2, that the unit cell structure has 6 different effective lengths for incident EM waves (TE wave and TM wave), which makes the FSS have 6 different basic resonant frequencies and 6 corresponding basic stop-bands. Besides, some high-order resonances could also be excited which could further increase the number of stop-bands of the FSS. That is the reason why L-shaped metal strips are selected in the paper.

For the purpose of comparison with the FSS designed in Section II. A, the dimension parameters of the unit cell are given as follow. The thickness of the bended metal strips is 0.035 mm. The lengths of two arms of L-shape are a_1 = 10.0 mm and a_2 = 6.0 mm, and the width of L-shaped metal strips is w = 1.0 mm, as shown in Fig. 1. The inner radius of “L” pattern is r = 4.0 mm, and the rotation angle between two adjacent L-shaped metal strips is α= 30°. The length, thickness and relative permittivity of the dielectric substrate are the same as the FSS designed in Section 2.1.

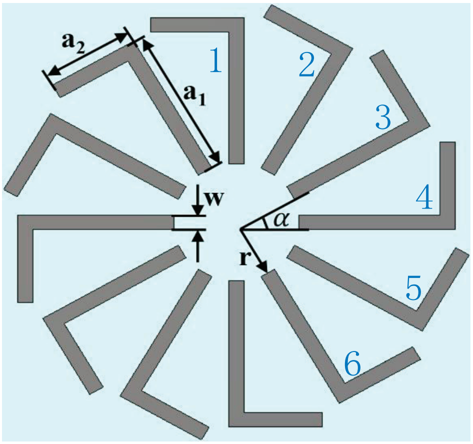

(a) Top view of FSS unit

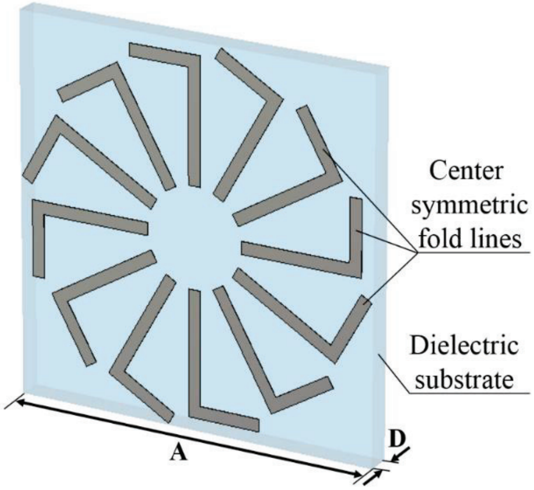

(b) 3-D view of FSS unit

Fig. 2. Configuration of the improved FSS unit cell.

The unit cell is truncated by using PBC in CST MWS 2012 and the simulation settings including boundary conditions and mesh type are same as Section II. A. Figure 3 shows the transmission of the FSS structure for the TE and TM incident waves. It can be seen from Fig. 3, that the FSS structure has fifteen stop-bands and sixteen pass-bands in the frequency band from 6 GHz to 20 GHz, and the frequency ranges of the sixteen pass-bands are illustrated in Table 1. In addition, it can be observed that transmission of the FSS for TE and TM waves is nearly identical, which verifies that the FSS is polarization insensitive.

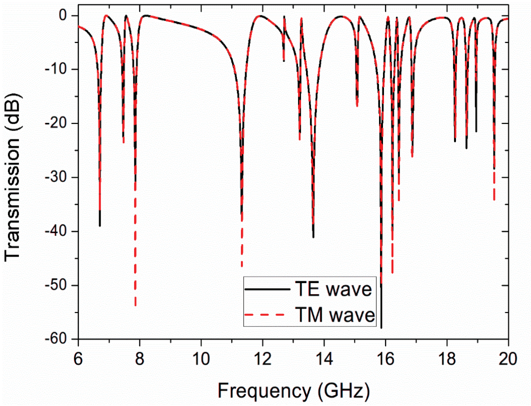

Fig. 3. Transmission coefficients of the improved FSS structure for TE and TM waves.

Table 1: Frequency ranges of sixteen pass-bands

Pass-band Number	1st	2nd	3rd	4th
Frequency Range (GHz)	6.00-6.30	6.78-7.30	7.50-7.70	7.95-10.18
Pass-band Number	5th	6th	7th	8th
Frequency Range (GHz)	11.62-12.76	13.23-13.30	14.10-14.98	15.10-15.42
Pass-band Number	9th	10th	11th	12th
Frequency Range (GHz)	16.02-16.14	16.34-16.40	16.63-16.82	17.10-18.18
Pass-band Number	13th	14th	15th	16th
Frequency Range (GHz)	18.34-18.58	18.74-18.92	18.98-19.47	19.61-20.00

Comparing with the simulation results of the FSS proposed in Section II. A, it can be observed that the improved FSS has 16 stop-bands which is over three times as much as the former one. Meanwhile, the pass-bands of the improved FSS are distributed more evenly in frequency which makes the FSS more valuable in real application. In addition, it can be seen from Fig. 1 to Fig. 3, that in same conditions the stop-bands move to lower frequencies which results from the longer effective lengths of improved unit cell.

In order to explore the multi-band frequency property of the proposed FSS, eight valley points in the transmission pattern are selected as examples. The surface current distributions at the eight frequencies for TE wave are illustrated in Fig. 4. It can be seen from the figure that different L-shaped metal strips resonate at different frequencies. For example, at 6.70 GHz, the two L-shaped metal strips in the vertical direction resonate; while at 7.46 GHz, the two L-shaped metal strips at an angle of 30 degrees to the horizontal direction resonate. The reason why different metal strips resonate at different frequencies is that the length at different angles for TE wave is different, which can be expressed as follows:

$$\begin{aligned} le &= a_1 \cos(90^\circ - \alpha) + a_2 \sin(90^\circ - \alpha) \\ &= a_1 \sin\alpha + a_2 \cos\alpha, \end{aligned} \tag{1}$$

where $\boldsymbol{\alpha}$ is the angle between one L-shaped metal strips with respect to the horizontal axis, and $\boldsymbol{l_e}$ is the equivalent length of L-shaped metal strips. Obviously, the resonant frequencies of L-shaped metal strips increase with decrease of equivalent length $\boldsymbol{l_e}$, which results in the multi-band frequency property. Moreover, the FSS structure has some additional resonant modes besides single L-shaped metal strips resonant modes such as Figs. 4 (g) and 4 (h), which make the FSS have more stop-bands.

To explain the simulation results in detail, physical interpretations are given below.

The reflectivity $\mathbf{S_{11}}$ of the FSS can be described by (2):

$$\left|S_{11}\right| = \left|\frac{Z_{in} - Z_0}{Z_{in} + Z_0}\right|, \tag{2}$$

where $\boldsymbol{Z_{in}}$ is the input impedance of FSS and $\boldsymbol{Z_0}$ is the wave impedance of free space. It can be learned from (2), that $\boldsymbol{Z_{in}} = \boldsymbol{Z_0}$ is necessary to decrease the reflective wave and in that case $\mathbf{S_{21}}$ of the FSS is possible to be kept in a high value.

In the condition that L-shaped strips do not resonate, the incident EM waves can propagate through the FSS easily because the input impedance $\boldsymbol{Z_{in}}$ is close to the free space wave impedance $\boldsymbol{Z_0}$. and the reflectivity $\mathbf{S_{11}}$ is quite small. Then in the condition that L-shaped strips resonate, the input impedance $\boldsymbol{Z_{in}}$ has a sharp change around the resonance frequency which makes the value of $\boldsymbol{Z_{in}}$ not close to $\boldsymbol{Z_0}$ anymore and results in a high reflectivity $\mathbf{S_{11}}$, which means the incident wave cannot propagate through the FSS. In general, the FSS will has a stop-band in case that the unit cell resonates at a frequency. Because of the multi-resonance property of the unit cell, the FSS proposed in the paper has such many pass-bands and stop-bands in the frequency band from 6 GHz to 20 GHz.

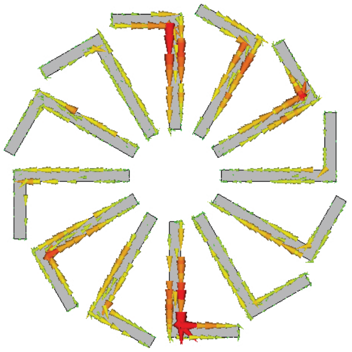

(a) The case at 6.70 GHz

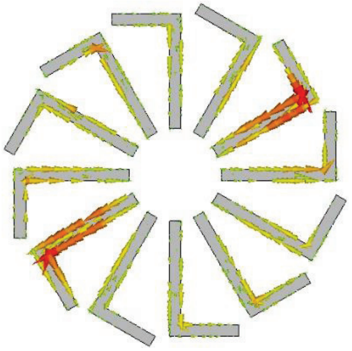

(b) The case at 7.46 GHz

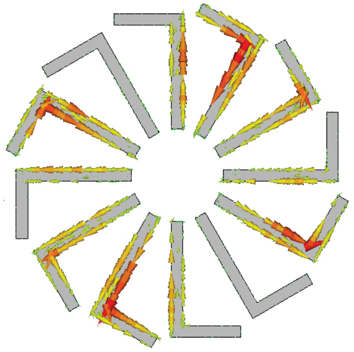

(c) The case at 7.86 GHz

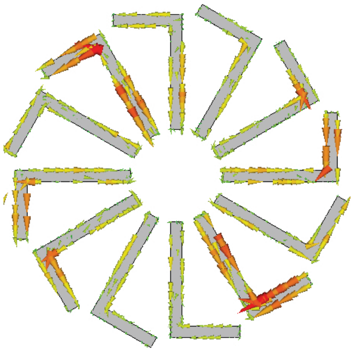

(d) The case at 15.86 GHz

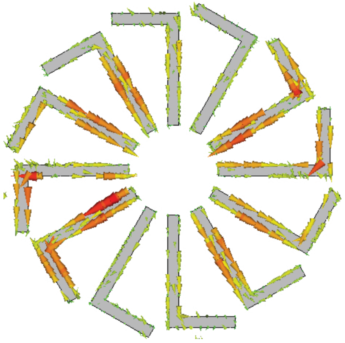

(e) The case at 16.22 GHz

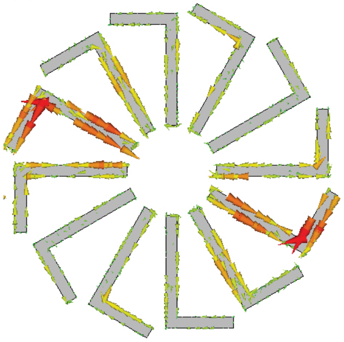

(f) The case at 16.88 GHz

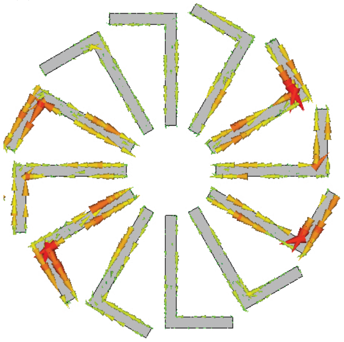

(g) The case at 16.43 GHz

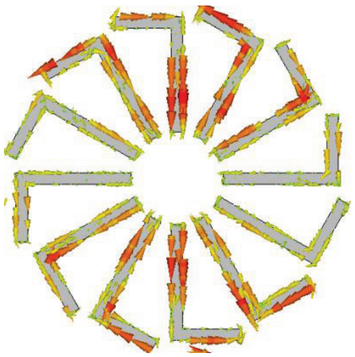

(h) The case at 18.84 GHz

Fig. 4. Surface current distributions at the eight typical frequencies for TE incident wave.

The simulation results of the surface current distributions for TM incident wave are almost the same as those for TE wave. These simulation results verify the polarization insensitive property of the proposed FSS structure.

III. EFFECTS OF THE STRUCTURE PARAMETERS ON THE FSS

A. The distance between symmetric center and one end of fold line *r*

To explore the FSS amplitude-frequency characteristic, we change the inner radius ***r*** from 2.0 mm, 3.0 mm to 4.0 mm. The transmission coefficient in the frequency band of 10-15 GHz for TE wave is illustrated in Fig. 5. It can be seen from Fig. 5, that the trend of resonant frequency varies with different valley points when ***r*** increases. When the frequency at the first valley point increases, the frequencies at the second and the third valley points remain invariant, while the frequency at the last valley point decreases. It is the reason why the FSS structure has some additional resonant modes besides single L-shaped metal strips resonant modes. For these complex resonant modes, the effect analyses of ***r*** on the FSS property are difficult, while for a single L-shaped metal strips resonant mode, the inner radius has little effect on the resonant frequencies.

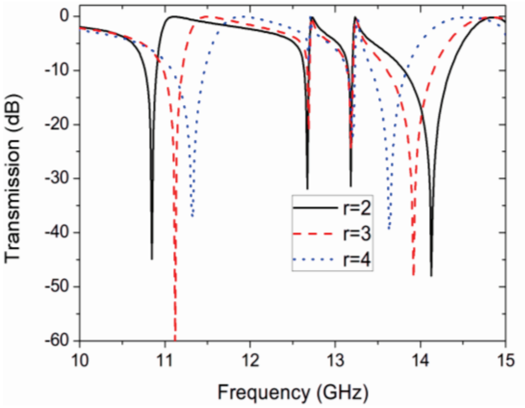

Fig. 5. Transmission coefficients of the FSS structure with different inner radius ***r***.

B. The side length of dielectric substrate *A*

Change the length and width of dielectric substrate ***A*** to be different values from 30.0 mm to 32.0 mm, 34.0 mm to 36.0 mm, and the transmission coefficients of the FSS structure in the frequency band of 9 to 14 GHz for TE wave are plotted in Fig. 6. The resonant frequencies decrease with the increase of ***A*** and the deepness of valley points varies at the same time, which is mainly caused by the coupling of adjacent unit cells. Generally speaking, smaller ***A*** is necessary for its good effects on suppressing grating lobe and widening the band width.

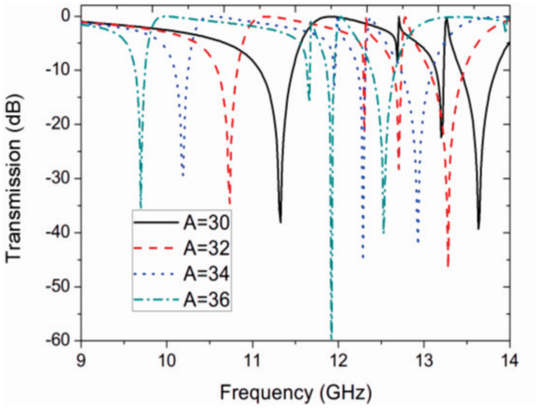

Fig. 6. The transmission of the FSS with different side lengths of dielectric substrate ***A***.

C. Width of fold lines *w*

In this section, we change the width of L-shaped metal strips ***w*** to be different values from 0.4 mm, 1.0 mm to 1.6 mm to investigate the FSS amplitude-frequency characteristic. Figure 6 shows the transmission coefficients of the FSS structure in the frequency band of 10 to 15 GHz for TE wave. It can be seen from Fig. 7, that the trend of resonant frequency is ruleless with the increase of ***w*** due to the multi-resonant modes of the FSS structure. In other words, the width of L-shaped metal strips ***w*** has different effects on the transmission property under different resonant modes. However, it can be summarized that increasing ***w*** is beneficial for deepening the deepness of valley points at resonant frequencies.

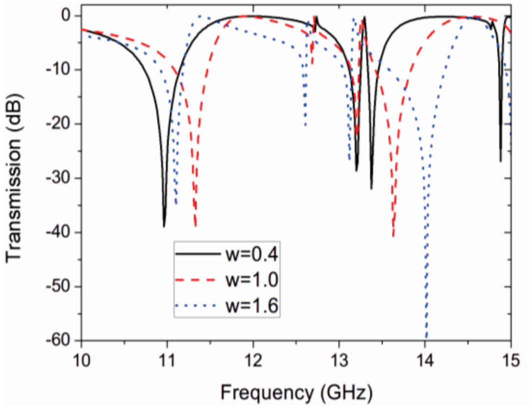

Fig. 7. The transmission of the FSS with different widths of fold lines ***w***.

IV. CONCLUSIONS

In summary, a novel multi-band polarization insensitive FSS based on rotationally symmetric L-shaped metal strips is proposed in this paper. The FSS structure is polarization insensitive due to the symmetric structure; meanwhile, different L-shaped metal strips had different equivalent lengths for electromagnetic wave to resonate at different frequencies that grant the FSS structure an excellent multi-band property. According to simulation results, the FSS structure had fifteen stop-bands and sixteen pass-bands for TE and TM waves in the frequency band of 6 to 20 GHz. In addition, effects of some structure parameters are analyzed, which can provide theoretical basis for practical use. Owing to the great multi-band property and thin, light and flexible features, the FSS designed in this paper is believed to have broad application prospects in modern wireless communication system and even 5G communication system in the future.

ACKNOWLEDGMENT

This work is supported by the Nation Nature Science Foundation of China No. 61301095 and 61201237, and Nature Science Foundation of Heilongjiang Province of China No. QC2012C069.

Meantime, all the authors declare that there is no conflict of interests regarding the publication of this article.

REFERENCES

[1] T.-K. Wu, *Frequency Selective Surfaces*, Encyclopedia of RF and Microwave Engineering: John Wiley & Sons, Inc., 2005.

[2] S. A. Winkler, W. Hong, M. Bozzi, and K. Wu, "Polarization rotating frequency selective surface based on substrate integrated waveguide technology," *Antennas and Propagation, IEEE Transactions on*, vol. 58, no. 4, pp. 1202-1213, 2010.

[3] B. A. Munk, *General Overview, Frequency Selective Surfaces*, John Wiley & Sons, Inc., pp. 1-25, 2005.

[4] H. Y. Yang, S. X. Gong, P. F. Zhang, F. T. Zha, and J. Ling, "A novel miniaturized frequency selective surface with excellent center frequency stability," *Microwave and Optical Technology Letters*, vol. 51, no. 10, pp. 2513-2516, 2009.

[5] S. Monni, A. Neto, G. Gerini, F. Nennie, and A. Tijhuis, "Frequency-selective surface to prevent interference between radar and SATCOM antennas," *Antennas and Wireless Propagation Letters, IEEE*, vol. 8, pp. 220-223, 2009.

[6] J. P. Gianvittorio, J. Romeu, S. Blanch, and Y. Rahmat-Samii, "Self-similar prefractal frequency selective surfaces for multiband and dual-polarized applications," *Antennas and Propagation, IEEE Transactions on*, vol. 51, no. 11, pp. 3088-3096, 2003.

[7] K. Ueno, T. Itanami, H. Kumazawa, and I. Ohtomo, "Characteristics of frequency selective surfaces for a multi-band communication satellite," *IEEE AP-S Int. Symp. Dig.*, pp. 735-738, June 1991.

[8] J. Romeu and Y. Rahmat-Samii, "Fractal FSS: a novel dual-band frequency selective surface," *Antennas and Propagation, IEEE Transactions on*, vol. 48, no. 7, pp. 1097-1105, 2000.

[9] D. J. Kern, D. H. Werner, A. Monorchio, L. Lanuzza, and M. J. Wilhelm, "The design synthesis of multiband artificial magnetic conductors using high impedance frequency selective surfaces," *Antennas and Propagation, IEEE Transactions on*, vol. 53, no. 1, pp. 8-17, 2005.

Yun Lin (S'99-M'03) received his Ph.D. degree in Communication and Information in 2010 from Harbin Engineering University, Harbin, China. He joined the Information and Communication College, HEU, Harbin, China, in 2005, where he is currently a Professor, Vice-Dean of ICEC College, Director of the Smart Communications Lab for ICEC. His research has focused on information fusion, signal processing and EMC on antenna, mm-wave and THz. He has authored and co-authored over 5 papers in refereed journals and conference proceedings.

Xu Xiao-chun stayed in Harbin Engineering University (HEU) to read her B.E. during 2009-2013, and recieved her B.E. in the College of Underwater Acoustic Engineering from HEU in 2013. She reads her M.A. in Harbin Engineering University and is studying Signal Processing.

Zheng Dou (S'97-M'01) received his Ph.D. degree in Communication and Information in 2007 from Harbin Engineering University, Harbin, China. He joined the Information and Communication College, HEU, Harbin, China, in 2001, where he is currently a Professor, Vice-Dean of ICEC College, Director of the Smart Communications Lab for ICEC. He spent one year as a Research Fellow and an Invited Professor at the University of Hertford, Hatfield, UK, and three months as a Visiting Professor at Wright University, USA in 2013. His research has focused on Smart Communications and EMC, which includes all-one platform on Smart

Communications, Architecture and protocols, EMC on antenna, mm-wave and THz, IR-UWB communications and signal processing. Dou has authored and co-authored over 2 papers in refereed journals and over 30 papers in conference proceedings.

Band-Stop Antenna with Enhanced Bandwidth by Using Several Pairs of Inverted L-Shaped Sleeves on the Ground for Wireless Applications

M. Akbari [*1], S. Zarbakhsh [1], N. Rojhani [3], and A. Sebak [2]

[1] Young Researchers and Elite Club, Central Tehran Branch
Islamic Azad University, Tehran, Iran.
*akbari.telecom@gmail.com

[2] Electrical and Computer Department
Concordia University, Quebec, H3G 1M8, Canada

[3] Young Researchers and Elite Club, South Tehran Branch
Islamic Azad University, Tehran, Iran

Abstract **─** A very wideband rectangular monopole antenna with band notched performance for wireless applications is proposed. The very wideband performance is obtained by introducing a new technique on the ground plane including several pairs of inverted L-shaped sleeves which provide a very wide bandwidth. By utilizing two radiating stubs in which an inverted Ω-shaped strip is protruded, band-notched characteristics can be obtained. The measured results exhibit that the antenna is able to covers the bandwidth from 2.5 to 17.5 GHz, excluding the rejected bands from 3.1 to 4 GHz and from 5 to 6 GHz.

Index Terms **─** Antenna, stop band, UWB, very wide band.

I. INTRODUCTION

The impending and widespread requirements from commercial and military domains on wireless systems, in particular UWB systems, have sparked great interest in the field of UWB antenna design [1]. Different sorts of UWB antennas have been studied and proposed [2-4]. However, due to the allocation of the extended frequency range in UWB system (e.g., a portion of the spectrum between 3.1 and 10.6 GHz is dedicated for UWB system by Federal Communications Commission), a UWB antenna is quite susceptible to interference by receiving several narrow band signals of neighboring RF systems, such as 3.5 GHz Worldwide Interoperability for the Microwave Access (WiMAX) and 5.2/5.8 GHz Wireless Local Area Network (WLAN) communication systems. Therefore, it is desirable to design a UWB antenna with multiple band-notched characteristics to avoid the potential interference [1]. In the published literatures, there have been some reports on the UWB antennas with band-notched characteristics [5-7]. Although, the majority of these antennas are designed to generate only one notched frequency band, so that just one narrow band of disturbance can be eliminated. Consequently, these antennas are still open to other potential disturbance from neighboring RF systems. In this paper, a very wide band antenna with band-notched characteristics for Wireless and also UWB applications is proposed. By utilizing the set of new techniques on radiating patch and ground plane, very wide band and band-notched UWB characteristics can be obtained.

II. ANTENNA DESIGN

The configuration of the proposed antenna is demonstrated in Fig. 1. The antenna is designed and fabricated on a FR4 substrate with dielectric constant of 4.4, thickness of 1 mm, and overall dimension of 18mm×12mm. The structure of basic antenna consists of a square radiating patch, a

Submitted On: November 25, 2013
Accepted On: October 6, 2014

ground plane, and a feed line which its width is fixed at 2 mm. Furthermore, the antenna is connected to a 50-Ω SMA connector for signal transmission. The size of the square patch is 10×10 mm^2 and the gap between the patch and ground plane is 4 mm. The dimensions of the ground plane is 12×3 mm^2. This is basic antenna; i.e., Printed Rectangular Monopole Antenna (PRMA) named as Antenna 1. To achieve optimum impedance matching at UWB frequency band, the ground plane with several pairs of inverted L-shaped sleeves play important roles in the broadband characteristics of this antenna, because they can adjust the electromagnetic coupling effects between the patch and the ground plane, and improves its impedance bandwidth without any cost of size or expense. Based on the design shown in Fig. 1, by using two radiating stubs in which an inverted Ω-shaped strip is protruded, band-notched characteristics at 3.5 GHz and 5.5 GHz can be obtained.

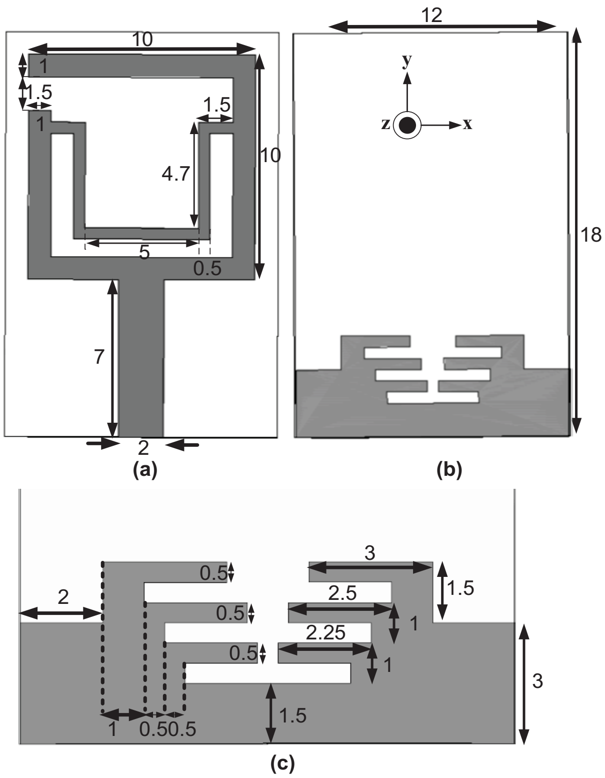

(a) (b)

(c)

Fig. 1. Geometry of the proposed antenna: (a) top layer, (b) bottom layer, and (c) the ground plane with three pairs of inverted L-shaped sleeves.

III. ANTENNA PERFORMANCE AND DISCUSSION

A. Very wideband monopole antenna

In this section, the numerical and experimental results of the input impedance and radiation characteristics are discussed. The simulated results are obtained using the Ansoft simulation software High-Frequency Structure sSmulator (HFSS) [8]. The main idea of the antenna suggested has come from [9], which a pair of inverted L-shaped sleeves has been used. Figure 2 exhibits the simulated reflection coefficient characteristics for the various antenna structures with pairs of inverted L-shaped sleeves on the ground plane. As illustrated in Fig. 2 (a), PRMA without any sleeves has a resonant frequency at 3.5 GHz and its impedance bandwidth is limited from 3 to 5 GHz, while by using a pair of sleeves, Fig. 2 (b), another resonant frequency is obtained at 8.5 GHz causing the impedance bandwidth from 3.2 to 10 GHz. Ultimately, from Fig. 2 (d), can be found that by applying three pairs of sleeves three resonant frequency except the main resonant frequency of PRMA (at around 4 GHz) can be achieved, which it ends up extending impedance bandwidth (133%) from 3.4 to 17 GHz. Therefore, bandwidth is effectively improved at the upper frequency by utilizing several pairs of sleeves shown in Fig. 1 (c).

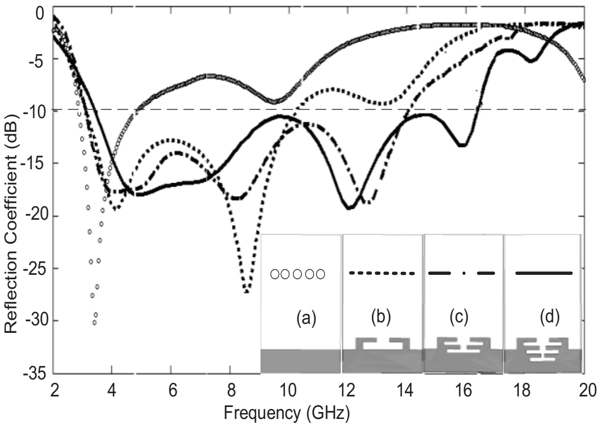

Fig. 2. Simulated reflection coefficient characteristics for the various antenna structures with pairs of inverted L-shaped sleeves on the ground plane: (a) PRMA without any sleeves, (b) with a pair of sleeves, (c) with two pairs of sleeves, and (d) with three pairs of sleeves

Simulated surface current distributions on the various ground structures at 16 GHz is shown in Fig. 3. It can be found that the current is more concentrated on edges of the interior and exterior of each three pairs of the sleeves at 16 GHz. Therefore, the antenna impedance changes at this frequency due to the resonant properties of its coupling. In addition, it is seen that by using this structure, an additional resonant mode occurs at about 16 GHz in the simulation.

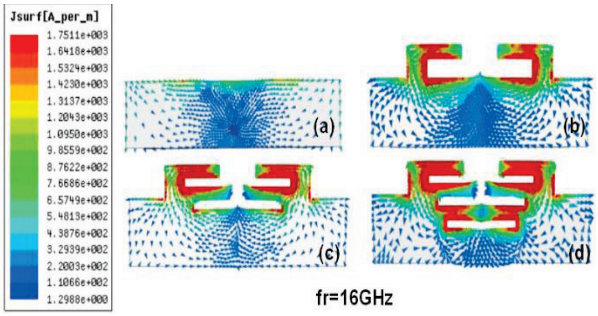

Fig. 3. Simulated surface current distributions on the various ground structures at 16 GHz: (a) PRMA without any sleeves, (b) with a pair of sleeves, (c) with two pairs of sleeves, and (d) with three pairs of sleeves.

B. Very wideband monopole antenna with frequency band-notch characteristics

In this letter, in order to generate the frequency band stop performances, two radiating stubs and an inverted Ω-shaped strip is used as displayed in Fig. 1. The simulated VSWR curves for the antenna structures are plotted in Fig. 4. As shown in Fig. 4, when radiating square patch (PRMA) is varied to radiating stub, impedance matching is nearly ruined. While by changing radiating stub in Fig. 4 (b) to two radiating strips in Fig. 4 (c), not only impedance bandwidth is improved but also a notched band is obtained at center frequency 3.5 GHz. On the other hand, by adding an inverted Ω-shaped strip between the both of radiating strip as shown in Fig. 4 (d), another notched band at center frequency 5.5 GHz is achieved. Therefore, it is found that by using two new techniques, a dual band–notch function can be earned that covers all the 5.2/5.8 GHz WLAN and 3.5/5.5 GHz WiMAX. The simulated peak gain and radiation efficiency are plotted in Fig. 5. The gains are started from -3.8 dBi at 2.5 GHz and ended up 2 dBi at 10 GHz. It is crystal clear that small size is the most important reason for being decrease gain. Besides, due to the rejected bands, -10 dBi and -8 dBi at frequencies 3.7 GHz and 5.5 GHz can be seen.

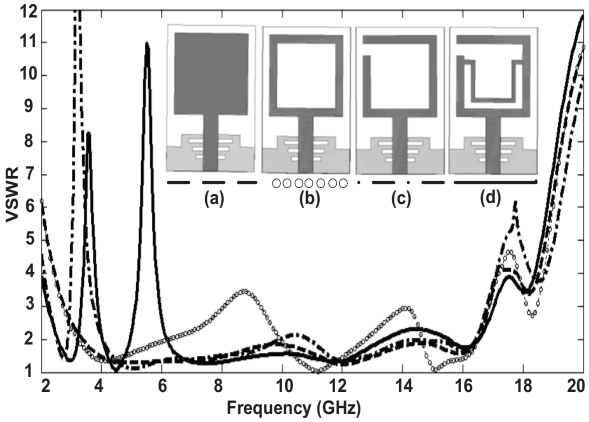

Fig. 4. Simulated VSWR characteristics for the various antenna structures with three pairs of inverted L-shaped sleeves on the ground plane: (a) PRMA, (b) with radiating stub, (c) with two radiating strips, and (d) the proposed antenna.

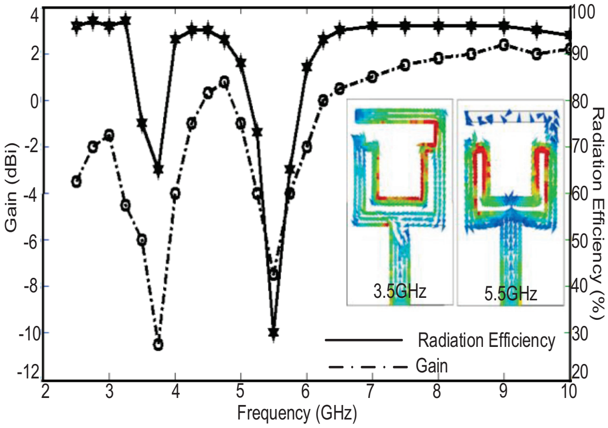

Fig. 5. Simulated gain and radiation efficiency of the proposed antenna and surface current distributions on two radiating strips with an inverted Ω-shaped strip at: (a) 3.5 GHz, and (b) 5.5 GHz.

As expected before, radiation efficiency on over frequency band except notched bands is more than 90%. The mechanism of the band-notched characteristics can be investigated from the currents on the antenna. Then, the simulated current distributions at 3.5 and 5.5 GHz for the proposed antenna are presented in Figs. 5 (a) and (b). It can be found that the currents at 3.5 and 5.5 GHz mainly distributed along two radiating strips at 3.5 GHz and an inverted Ω-shaped strip at 5.5 GHz, respectively. The prototype of the proposed antenna has been constructed and experimentally studied. With the help of the Ansoft HFSS software and an Agilent E8363B Network Analyzer, the simulated and measured VSWR curves are shown in Fig. 6. From the measured results we observed that the impedance band for VSWR≤2 is (150%) from 2.5 to 17.5 GHz, excluding the rejected bands from 3.1 to 4 GHz and from 5.0 to 6.0 GHz. The E-plane and H-plane radiation patterns for the proposed antenna at 4.5 and 7 GHz are shown in Fig. 7. It can be seen that the radiation patterns are bi-directional in the E-plane and almost omni-directional in the H-plane, which indicate good monopole-like radiation characteristics are achieved over the operating bands.

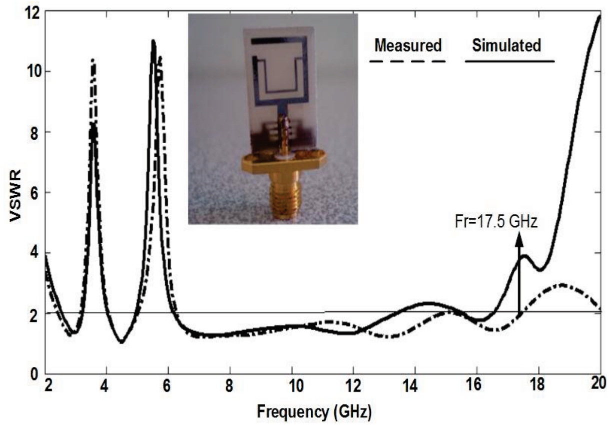

Fig. 6. Measured and simulated VSWR characteristics for the antenna and photo of the fabricated antenna.

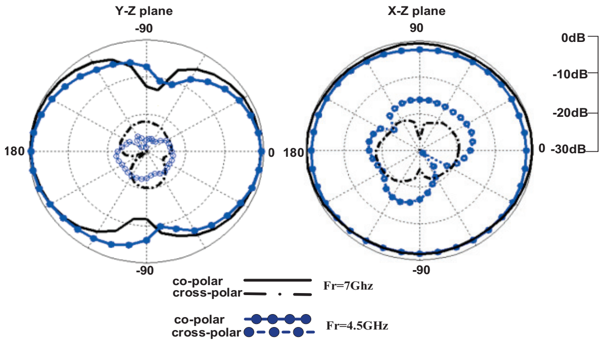

Fig. 7. Radiation patterns of the proposed antenna at 4.5 GHz and 7 GHz: (a) H-plane, and (b) E-plane.

IV. CONCLUSION

In this letter, a new antenna with band-stop characteristics has been proposed for wireless applications. The fabricated antenna is able to cover the frequency band of 2.5 to 17.5 GHz, except two rejection bands around 3.1-4.0 GHz and 5.0-6.0 GHz. The proposed antenna has a simple configuration and is easy to fabricate. Experimental results exhibit that the proposed antenna could be a good candidate for UWB application.

REFERENCES

[1] J. Ding, Z. Lin, Z. Ying, and S. He, "A compact ultra-wideband slot antenna with multiple notch frequency bands," *Microwave Optical Technol. Lett.*, vol. 49, no. 12, pp. 3056-3060, 2007.

[2] M. Akbari, M. Koohestani, C. Ghobadi, and J. Nourinia, "A new compact planar UWB monopole antenna," *International Journal of RF and Microwave Computer-Aided Engineering*, vol. 21, no. 2, 216-220, 2011.

[3] M. Akbari, M. Koohestani, C. Ghobadi, and J. Nourinia, "Compact CPW-fed printed monopole antenna with super wideband performance," *Microwave Opt. Technol. Lett.*, vol. 53, no. 7, 1481-1483, 2011.

[4] M. Mighani, M. Akbari, and N. Felegari, "Design of a small rhombic monopole antenna with parasitic rectangle into slot of the feed line for SWB application," *The Applied Computational Electromagnetic Society*, vol. 27, no. 1, 74-79, 2012.

[5] W. S. Chen and C. H. Lin, "A dual-band rejected cross monopole antenna maintaining omni-direction radiation," *Microwave Optical Technol. Lett.*, vol. 50, no. 10, pp. 2491-2493, 2008.

[6] M. Mighani, M. Akbari, and N. Felegari, "A CPW dual band notched UWB antenna," *Applied Computational Electromagnetics Society (ACES) Journal*, vol. 27, no. 4, pp. 352-359, April 2012.

[7] A. Valizade, J. Nourinia, C. Ghobadi, and M. Ojaroudi, "A novel design of reconfigurable slot antenna with switchable band notch and multi-resonance functions for UWB applications," *IEEE Antennas Wireless and Propag. Lett.*, vol. 11, pp. 1166-1169, 2012.

[8] "Ansoft high frequency structure simulation (HFSS), ver. 13, *Ansoft Corporation*, 2010.

[9] A. R. Zolfagharian, M. N. Azarmanesh, and M. Ojaroudi, "Ultra-wideband small square monopole antenna with variable frequency notch band characteristics using an interdigital slot," *Microwave Optical Technol. Lett.*, vol. 54, no. 1, pp. 262-267, 2012.

Mohammad Akbari was born on February 3, 1983 in Tehran, Iran. He received his B.Sc. degree in Engineering Telecommunication from the University of Shahid Bahonar, Kerman, Iran, in 2007 and M.Sc. degrees in Electrical Engineering Telecommunication from the University of Urmia, Urmia, Iran, in 2011. He has taught courses in microwave engineering, antenna theory, Fields & Waves, and electromagnetic at Aeronautical University, Tehran, Iran. He is currently pursuing the Ph.D. degree jointly at Concordia University, Montreal, Canada. His main field of research contains analysis and design of microstrip antennas, modeling of microwave structures, radar systems, electromagnetic theory and analysis of UWB antennas for WBAN applications, antenna interactions with human body, computational electromagnetics (time- and frequency-domain methods), and microwave circuits and components. He is the author or co-author of approximately 40 peer-reviewed scientific journals and international conference papers. Akbari was awarded the Graduate Concordia Merit Scholarship.

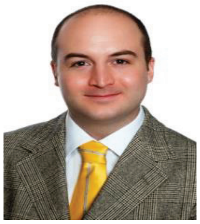

Saman Zarbakhsh was born on January 7, 1984 in Tehran, Iran. He received his B.Sc. degree in Electrical Engineering at Azad University of South Tehran, Tehran, Iran, in 2007 and his M.Sc. degree in Electrical Engineering from Urmia University, Urmia, Iran, in 2010. His research interests contain antenna design, antenna miniaturization and broadband circular polarized antennas. He has taught courses with the Electrical Engineering Department at Azad University of Shahre Rey University, Tehran, Iran.

Neda Rojhani was born on September 21, 1987 in Zahedan, Iran. She received her B.Sc. degree in Electrical Engineering at the University of Sistan and Baluchestan, Zahedan, Iran, in 2010, and she is studying the M.Sc. degree in Electrical Engineering at Islamic Azad University of South Tehran, Tehran, Iran. Her research interests include design of various antennas, antenna miniaturization, and antenna theory.

Abdel Razik Sebak (F'10) received the B.Sc. degree (with honors) in Electrical Engineering from Cairo University, in 1976 and the B.Sc. degree in Applied Mathematics from Ein Shams University, in 1978. He received the M.Eng. and Ph.D. degrees from the University of Manitoba, in 1982 and 1984, respectively, both in Electrical Engineering. From 1984 to 1986, he was with the Canadian Marconi Company, working on the design of microstrip phased array antennas. From 1987 to 2002, he was a Professor in the Electrical and Computer Engineering Department, University of Manitoba. He is a Professor of Electrical and Computer Engineering, Concordia University. His current research interests include phased array antennas, computational electromagnetics, integrated antennas, electromagnetic theory, interaction of EM waves with new materials and bioelectromagnetics. Sebak received the 2000 and 1992 University of Manitoba Merit Award for outstanding Teaching and Research, the 1994 Rh Award for Outstanding Contributions to Scholarship and Research, and the 1996 Faculty of Engineering Superior Academic Performance. He is a Fellow of IEEE. He has served as Chair for the IEEE Canada Awards and Recognition Committee (2002-2004) and the Technical Program Chair of the 2002 IEEE-CCECE and 2006 ANTEM conferences.

Miniaturized LTCC Bandpass Filter with Harmonic Suppression

Chuan Shao [1], Hui Tang [1], Rong Mao [2], Jian-Xin Chen [1], Jin Shi [1], and Zhi-Hua Bao [1]

[1] School of Electronics and Information
Nantong University, Nantong, 226019, China
jjxchen@hotmail.com

[2] North Information Control Group Co., Ltd.
528 Jiangjun Road, Jiangning District, Nanjing, China

Abstract **─** This paper presents a harmonic-suppressed bandpass filter using a 3-dimensional (3-D) half-wavelength transmission line resonator, which is fabricated using low temperature co-fired ceramic (LTCC) technology. Owing to the distributed-element method in this 3-D design, the spurlines can be easily etched on the coupled feed lines to generate an extra transmission zero in the stopband without enlarging the circuit size. As a result, the second harmonic can be rejected to a great extent. For demonstration, a pair of two-order LTCC bandpass filters centered at 2.45 GHz with/without spurlines are designed using the compact 3-D resonator, and the size of the circuits is only 4.4×4.2×1.6 mm^3.

Index Terms **─** Harmonic suppression, LTCC, spurline, transmission zero.

I. INTRODUCTION

In modern communication systems, high-performance, compact and low-cost microwave components are urgently needed. Bandpass filter, as an indispensable passive component in microwave systems, usually suffers from the spurious responses at about twice/three times of the centre frequency of the desirable passband when using half-/quarter-wavelength resonators, which not merely reduces rejection levels in the stopband but also affects passband symmetry. Diverse techniques have been developed to suppress the harmonics and spurious response [1-6], such as discriminating coupling [1], spurline [2-4], and defected ground structure [5] and so on. The harmonic-suppressed filters proposed in [1-6] are planar topologies which may endure the bulky sizes. To achieve miniaturization, low-temperature co-fired ceramic (LTCC) bandpass filters based on lumped/semi-lumped elements have been developed in [7-9]. However, the harmonic suppression of the LTCC filters is seldom discussed. In [9], an extra stepped impedance quarter-wavelength ($\lambda_g/4$) open stub has to be added to reject the second harmonic.

In this paper, a 3-dimensional (3-D) $\lambda_g/2$ resonator is employed for designing LTCC bandpass filters centered at 2.45 GHz. Owing to this multilayer resonator, the size of the LTCC filters can be reduced significantly. Harmonic suppression can be easily achieved by etching the spurlines on the coupled feeding lines without increasing the entire size of the filter.

II. LTCC BANDPASS FILTERS DESIGN

The vertically and horizontally folded transmission line resonator is shown in Fig. 1. As there is a voltage null node at the middle point of the $\lambda_g/2$ resonator, a virtual ground can be set in the symmetrical plane of the 3-D multilayer resonator at the fundamental resonant frequency [10]. In this way, each part of the 3-D resonator has its corresponding ground (actual/virtual ground) to form the return path of the signal, although some striplines are overlapped in the vertical direction (z direction).

Based on the proposed 3-D multilayer resonator shown in Fig. 1, LTCC filters using the 3-D multilayer resonator are designed accordingly. The 3-D view, each layer configuration and the cross-section view of the proposed LTCC bandpass

Submitted On: August 15, 2013
Accepted On: December 11, 2014

filter with etched spurlines are shown in Fig. 2 and each layer configuration is illustrated in Fig. 3.

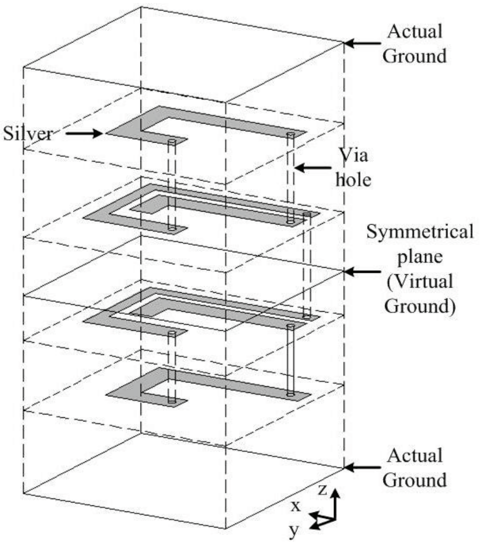

Fig. 1. 3-D structure of the vertically and horizontally folded $\lambda_g/2$ resonator.

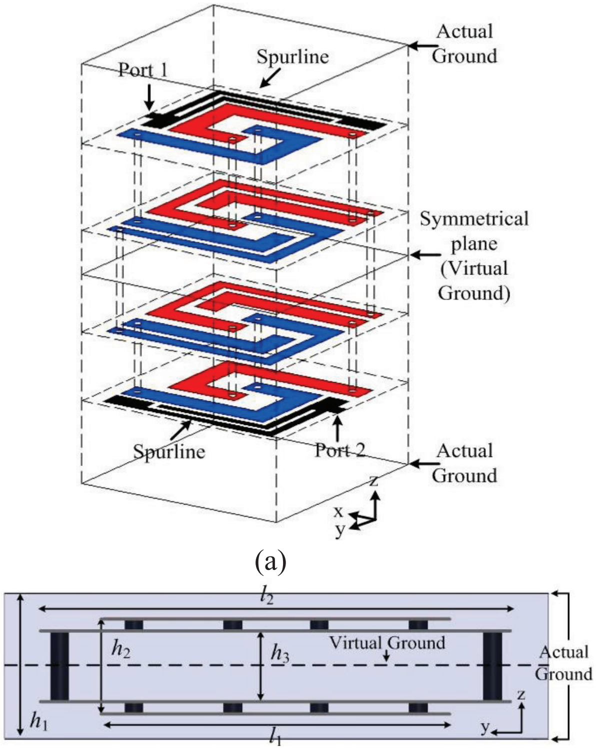

(a)

(b)

Fig. 2. Proposed LTCC bandpass filter with spurline: (a) 3-D view of the proposed LTCC bandpass filter, and (b) cross-section view of the proposed LTCC bandpass filter.

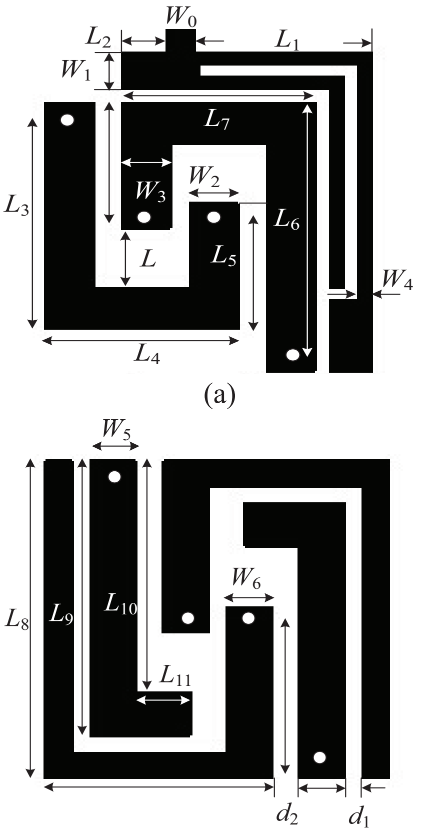

(a)

(b)

Fig. 3. Layer configuration: (a) layer details of layer 1 and layer 4, and (b) layer details of layer 2 and layer 3.

Then, according to the specification of the quasi-elliptic response with 2.45 GHz and FBW=10%, the coupling coefficients and I/O external quality factors calculated from [11] may be expressed as:

$$Q_e = \frac{g_0 g_1}{FBW} = 17.7, \qquad K = \frac{FBW}{\sqrt{g_0 g_1}} = 0.079,$$

where, g_0, g_1 and FBW are the element values of the lowpass prototype filter and fractional bandwidth.

Once the physical dimensions of 3D $\lambda_g/2$ resonator are determined, the parameters with respect to the tap position L_2 and the distance L between the resonators can be obtained by using the design curves as shown in Fig. 4 and Fig. 5.

The proposed filter can obtain two transmission zeros owing to the 0° feed structure [12], realizing good selectivity. The spurlines are introduced by etching them on the coupled feeding lines for second harmonic rejection, as shown in Fig. 2 (a). Meanwhile, unlike the planar configuration in [2-4], the etched spurlines will not enlarge the size of the LTCC filter.

For demonstration and comparison, a pair of LTCC bandpass filters centered at f_0=2.45 GHz with/without spurlines are designed and fabricated on sixteen layers of LTCC Ferro A6-M substrate with dielectric constant of 5.9 with a loss tangent of 0.002. Accordingly, the occupied sizes of the two LTCC bandpass filters are identical; i.e., 4.4×4.2×1.6 mm^3 ($0.088\lambda_g \times 0.084\lambda_g \times 0.032\lambda_g$ at f_0). The simulated results (using Ansoft HFSS) of the LTCC filters with/without spurlines are shown in Fig. 6. It can be seen from Fig. 6 that the etched spurlines on the coupled feeding lines have few effects on the fundamental passband. To suppress the second harmonic and obtain a suppression level of higher than 30 dB from 3 to 6 GHz, the total length of the spurline is optimized to be 4.9 mm, which approximately corresponds to quarter guided wavelength at the frequency of the newly-generated extra transmission zero shown in Fig. 6.

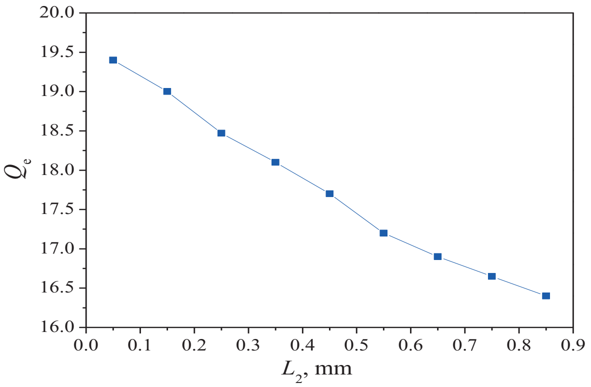

Fig. 4. Simulated external quality factors against the tap position of feeding lines.

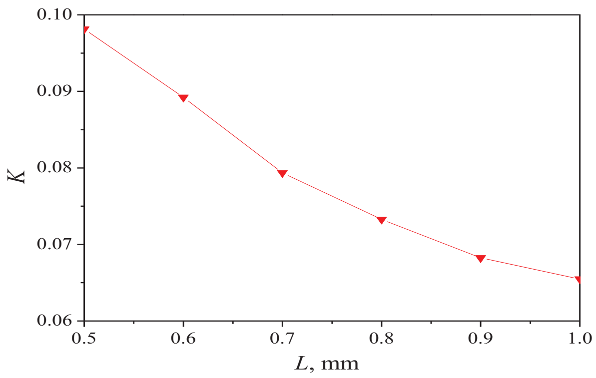

Fig. 5. Simulated coupling coefficients versus the gaps between resonators.

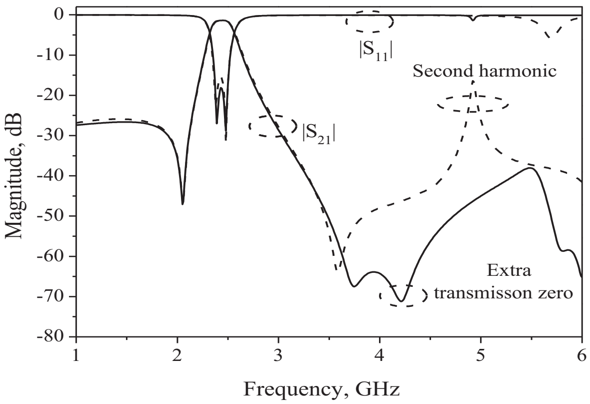

Fig. 6. Simulated results of the LTCC bandpass filters with/without spurlines (dot line: without spurlines, solid line: with spurlines).

III. MEASURED RESULTS

After optimization, the parameters of the LTCC filter with harmonic suppression are determined as follow: W_0=0.3 mm, W_1=0.45 mm, W_2=0.5 mm, W_3=0.5 mm, W_4=0.15 mm, W_5=0.5 mm, W_6=0.5 mm, L=0.7 mm, L_1=1.85 mm, L_2=0.45 mm, L_3=2.7 mm, L_4=2 mm, L_5=1.5 mm, L_6=3.2 mm, L_7=2 mm, L_8=3.7 mm, L_9=3.2 mm, L_{10}=3.7 mm, L_{11}=0.8 mm, d_1=0.2 mm, d_2=0.3 mm, diameter=0.15 mm, l_1=2.8 mm, l_2=3.8 mm, h_1=1.2 mm, h_2=0.8 mm, h_3=0.6 mm. The proposed LTCC bandpass filters with/without spurlines have been mounted on the printed circuit boards (PCBs) for measurement, as shown in Fig. 7. The measurement is carried out by network analyzer Agilent E8363C. According to the measurement, the LTCC filters center at 2.45 GHz. The insertion losses of these two filters are 2.3 dB, and the return losses are both better than 20 dB within the passbands, as can be seen from Fig. 8. As expected, more than 30 dB suppression level from 3 to 6 GHz is realized when the spurlines are employed as shown in Fig. 8. From Fig. 6 and Fig. 8, little disparity can be observed between simulation and measurement of the LTCC filters, which is believed to be caused by the fabrication tolerance in the multilayer and co-fired implementation.

Comparison between the proposed harmonic-suppressed LTCC filter and previously reported LTCC bandpass filters [13-17] is tabulated in Table 1. According to Table 1, it can be seen that the proposed LTCC filter with harmonic suppression shows compact size and comparable harmonic suppression performance.

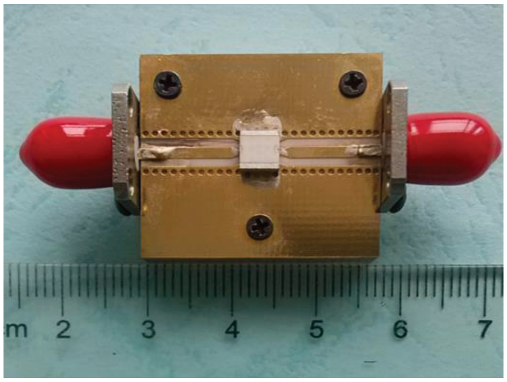

Fig. 7. Photograph of the proposed LTCC bandpass filter mounted on the PCB.

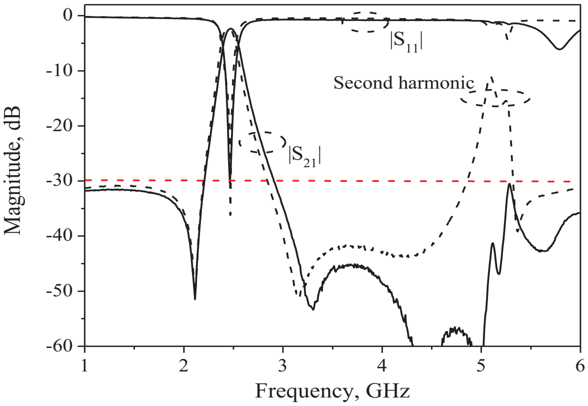

Fig. 8. Measured results of the LTCC bandpass filters with/without spurlines (dot line: without spurlines, solid line: with spurlines).

Table 1: Comparison between previously reported LTCC filters

Ref.	f_0 GHz	Filter Order	Stopband Performance	Electric Size (λ_g^3)
13	4.3	3	2.6 f_0 >20 dB	0.418×0.209× 0.035
14	2.45	3	2 f_0 >40 dB	0.094×0.047× 0.031
15	2.45	2	2.3 f_0 >30 dB	0.123×0.089× 0.017
16	2.55	2	2.2 f_0 >25 dB	0.091×0.069× 0.022
17	1.95	2	1.2 f_0 >10 dB	0.106×0.106× 0.013
This work	2.45	2	>2.45 f_0 >30 dB	0.088×0.084× 0.032

IV. CONCLUSION

In this paper, miniaturized LTCC bandpass filters with/without harmonic suppression are designed and fabricated based on the 3-D distributed-element resonator. Two transmission zeros on both sides of the passband improve the selectivity of the proposed filter. An extra transmission zero is generated by etching spurlines on the coupled feeding lines for harmonic suppression while the circuit size keeps the same. The measured harmonic rejection level of the bandpass filter is higher than 30 dB. The simulated and measured results are presented and show good agreement.

ACKNOWLEDGMENT

The work was supported by the National Natural Science Foundation of China under Grants 61271136 and 61301044, by six types of Talents Project of Jiangsu Province 2011-DZXX-014 and 2013-XXRJ-010, and by the Graduate Research and Innovation Plan Project of the Universities of Jiangsu Province under Grant YKC13007.

REFERENCES

[1] X. Y. Zhang and Q. Xue, "Harmonic-suppressed bandpass filter based on discriminating coupling," *IEEE Microw. Wireless Compon. Lett.*, vol. 19, no. 11, pp. 695-697, Nov. 2009.

[2] A. Torabi and K. Forooraghi, "Miniature harmonic-suppressed microstrip bandpass filter using a triple-mode stub-loaded resonator and spur lines," *IEEE Microw. Wireless Compon. Lett.*, vol. 21, no. 5, pp. 255-257, May 2005.

[3] W. H. Tu and K. Chang, "Compact microstrip bandstop filter using open stub and spurline," *IEEE Microw. Wireless Compon. Lett.*, vol. 15, no. 4, pp. 268-270, Apr. 2005.

[4] M. Hayati and S. Roshani, "A novel wilkinson power divider using open stubs for the suppression of harmonics," *Appl. Comp. Electro. Society (ACES) Journal*, vol. 28, no. 6, pp. 530-538, Jun. 2013.

[5] J.-S. Park, J.-S. Yun, and D. Ahn, "A design of the novel coupled-line bandpass filter using defected ground structure with wide stopband

performance," *IEEE Trans. Microw. Theory Tech.*, 50, no. 7, pp. 2037-2043, Sep. 2002.

[6] L. Gao, X. Y. Zhang, and Q. Xue, "Miniaturised bandpass filter using novel feeding structure for harmonic suppression," *Electron. Lett.*, vol. 48, no. 22, pp. 1414-1415, Oct. 2012.

[7] W.-S. Tung, Y.-C. Chiang, and J.-C. Cheng, "A new compact LTCC bandpass filter using negative coupling," *IEEE Microw. Wireless Compon. Lett.*, vol. 15, no. 10, pp. 641-643, Oct. 2005.

[8] G. Brzezina, L. Roy, and L. MacEachern, "Design enhancement of miniature lumped-element LTCC bandpass filters," *IEEE Trans. Microw. Theory Tech.*, vol. 57, no. 4, pp. 815-823, Apr. 2009.

[9] C.-W. Tang, "Harmonic-suppression LTCC filter with the step-impedance quarter-wavelength open stub," *IEEE Trans. Microw. Theory Tech.*, vol. 52, no. 2, pp. 617-624, Feb. 2004.

[10] J.-X. Chen, C. Shao, Q. Y. Lu, H. Tang, and Z. H. Bao, "Compact LTCC balanced bandpass filter using distributed-element resonator," *Electron. Lett.*, vol. 49, no. 5, pp. 354-356, Feb. 2013.

[11] J. S. Hong and M. J. Lancaster, *Microstrip Filters for RF/Microwave Applications*, New York: Wiley, 2001.

[12] C.-M. Tsai, S.-Y. Lee, and C.-C. Tsai, "Performance of a planar filter using a 0° feed structure," *IEEE Trans. Microw. Theory Tech.*, vol. 50, no. 10, pp. 2362-2367, Oct. 2002.

[13] X. J. Zhang, H. H. Zhang, and X. P. Ma, "Design of compact wideband LTCC filter using pentagonal-shaped SIR," *Electron. Lett.*, vol. 47, no. 5, pp. 327-328, Mar. 2011.

[14] M. Höft and T. Shimamura, "Design of symmetric trisection filters for compact low-temperature co-fired ceramic realization," *IEEE Trans. Microw. Theory Tech.*, vol. 58, no. 1, pp. 165-175, Jan. 2010.

[15] Y.-H. Jeng, S.-F. R. Chang, and H.-K. Lin, "A high stopband-rejection LTCC filter with multiple transmission zeros," *IEEE Trans. Microw. Theory Tech.*, vol. 54, no. 2, pp. 633-637, Feb. 2006.

[16] C. W. Tang and H. C. Hsu, "Development of multilayered bandpass filters with multiple transmission zeros using open-stub/short-stub/serial semilumped resonators," *IEEE Trans. Microw. Theory Tech.*, vol. 58, no. 3, pp. 624-634, Mar. 2010.

[17] V. Piatnitsa, E. Jakku, and S. Leppaevuori, "Design of a 2-pole LTCC filters for wireless communications," *IEEE Trans. Wireless Commun.*, vol. 3, no. 2, pp. 379-381, Mar. 2004.

Chuan Shao received the B.Sc. degree from Nantong University, Nantong, China, in 2012, and is currently working towards the M.S. degree in Electromagnetic Field and Microwave Technology at Nantong University, China. His research interests include microwave filters, etc.

Hui Tang received the M.S. degree from SHU, Shanghai, China, in 2004. Her research interests are RF circuits and antennas.

Rong Mao was born in Suqian, Jiangsu, China in 1983. She received the M.S. degree from Nanjing University of Science & Technology (NUST), Nanjing, China, in 2006. From 2006 to 2013, she has been with The 14th Institute of China Electronics Technology Group Corporation (CETC 14), where she was an Engineer. Since 2013, she has been with North Information Control Group Co., Ltd, where she is also an Engineer there. Her research interests include electronic circuit designs, embedded software design and the control model simulation.

Jian-Xin Chen was born in Nantong, Jiangsu Province, China, in 1979. He received the B.S. degree from Huai Yin Teachers College, Huai'an City, Jiangsu Province, China, in 2001, the M.S. degree from the University of Electronic Science and Technology of

China (UESTC), Chengdu, China, in 2004, and the Ph.D. degree from the City University of Hong Kong, Kowloon, Hong Kong, in 2008. Since 2009, he has been with Nantong University, Jiangsu Province, China, where he is currently a Professor. He has authored or co-authored more than 80 internationally referred journal and conference papers. He holds three Chinese patents and two U.S. patents. His research interests include microwave active/passive circuits and antennas, LTCC-based millimeter-wave circuits and antennas.

Chen received the New Century Excellent Talents in University in 2011. He was the recipient of the Best Paper Award presented at the Chinese National Microwave and Millimeter-Wave Symposium, Ningbo, China, in 2007. He was Supervisor of 2014 iWEM Student Innovation Competition winner in Sapporo, Japan. He is the Reviewer of several international journals, including *IEEE Microw. Wireless Compon. Lett.*, and *IEEE Trans. Microw. Theory Tech.*, etc.

Jin Shi received the M.S. degree from UESTC, Chengdu, China, in 2004, and the Ph.D. degree from CITYU, Kowloon, Hong Kong, in 2010. He is currently a Professor with Nantong University, Jiangsu Province, China.

Zhi-Hua Bao was born in Nantong, Jiangsu Province, China, in 1955. He received his B.S. degree from Chongqing University, Chongqin, China, in 1982, the M.S. degree from Nanjing University of Posts and Telecommunications, Nanjing, China, in 1985. In 1988, he joined Nantong University as a Lecturer, where he is currently a Professor with the School of Electronics and Information. He has authored or co-authored over 60 journal papers. He has owned 4 Chinese patents. His research interests include modern communication theory and technology, communications-specific integrated circuit designs and RF/microwave active and passive circuits.

Distributed Diode Single-Balanced Mixer Using Defected and Protruded Structures for Doppler Radar Applications

H. Ebrahimian, M. Ojaroudi, N. Ojaroudi, and N. Ghadimi

Department of Electrical Engineering
Ardabil Branch, Islamic Azad University, Ardabil, Iran
ebrahimian@iauardabil.ac.ir

Abstract **─** In this paper, a single-balanced diode mixer using defected and protruded structures for wireless application is presented. The operating frequency is selected for WLAN applications. The RF frequency is 2.412-2.484 GHz and the Local Oscillator (LO) is 2.132-2.204 GHz for 269 MHz Intermediate Frequency (IF) output signal. A Branch-Line Coupler is designed for the single-balanced of mixer. Four protruded T-shaped strip are used to obtain good convention gain and suppress unwanted harmonics. Also by using Defected Ground Structure (DGS) with folded T-shaped arms in the filter, a harmonic rejection property is generated. The measured performances of fabricated circuit conventionalize to the simulated results and LO to RF isolation is lower than -20 dB, LO to IF isolation is lower than -28 dB and Radio Frequency (RF) to IF is lower than -37 dB.

Index Terms **─** Defected Ground Structure (DGS), folded T-shaped arms, protruded T-shaped strip, single-balanced diode mixer.

I. INTRODUCTION

As a part of signal recovery circuit, a down-conversion mixer circuit is a necessary part. The conventional design technique for a balanced-diode mixer will be combined with the low-pass response of DGS to overcome the leakage RF and LO as well as other unwanted harmonics. A three-port down-conversion mixer convert signal of High Frequency (RF) from low-noise amplifier and LO stable signal from local oscillator .The mixing output signal at the output port consists of the signal whose designed frequency is a difference frequency between RF and LO, which is desired signal so called Intermediate Frequency (IF) and other unwanted signal products. For affordable technology, a hybrid mixing circuit can be designed by using diode or transistor [1]. The diode mixing circuit is simple and can be used up to millimeter wave. There are many publications of balanced-diode mixer, focusing is a LO leakage elimination by using either radial stub or conventional low-pass filter [2]-[5]. The use of band-rejection like stub limits the operating range of LO while the conventional Low-Pass Filter (LPF) offers very good RF and LO suppression, but not the higher harmonics.

In this paper, we propose a novel single balanced diode mixer with harmonic rejection property. By using four protruded T-shaped strip in the ordinary branch-line coupler, an excellent isolation -33 dB at 2.4 GHz can be achieved. Also by using DGS with folded T-shaped arms in the filter, a harmonic rejection property is generated. The proposed mixer circuit was designed by using a simulator to design ADS, in part of DGS design by HFSS and export S-parameter for using in ADS simulator for design mixer circuit. The measurement of power spectrum of mixer was performed using spectrum analyzer.

II. SINGLE-BALANCED DIODE MIXER CONFIGURATION

In this paper, we simulated and manufactured single-balanced diode mixer using defected ground structure and protruded T-shaped strips for wireless applications by using 2 simulators, Advance Design System (ADS) [6] and High Frequency Structures Simulators (HFSS) [7]. The presented miniature packaged mixer with the integrated band-reject filter is shown in Fig. 1, which is printed on Rogers

Submitted On: June 6, 2013
Accepted On: September 6, 2014

RT/Duroid 5880 substrate with 0.635 mm in thickness and with a relative dielectric constant of 2.2. In this structure we used Silicon Schottky diodes HSMS-2862. Mixer design for wireless LAN range with 2.412-2.484 GHz for RF, 269 MHz for IF output. The proposed design simplification of single-balanced diode mixer using DGS and the design are separated in 4 parts, design of branch-line coupler with protruded strip, design of matching circuit, design of defected ground structure, and circuit integration.

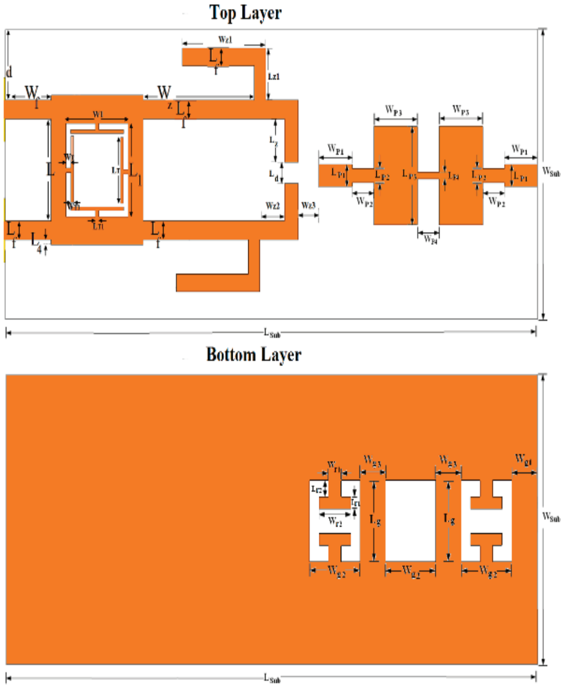

Fig. 1. Schematic of proposed single-balanced diode mixer using defected and protruded structures.

Quadrature hybrid mixers are used in microwave systems though their inherently poor LO-to-RF isolation, poor spurious-response rejection, and the fact that a poor RF-source VSWR at the LO frequency can unbalance themixer, they are distinctly inferior to 180-deg mixers. However, the practical advantages that the microstrip-line impedances used to realize a branch-line hybrid are easy to achieve, and the branch line is slightly smaller than ring hybrid at the same frequency. Also, the RF and LO ports of the branch-line hybrid mixer are on the same side of the hybrid, which is often an advantage in creating a compact circuit. The filter is used to reduce the out of band harmonics generated by the rectifying Schottkey diode. The width of the 50-Ω microstrip line is fixed at 0.9 mm. The matching circuit to the left and right of the device controls the degree of reflection. On the other side of the substrate, a conducting ground plane is placed. In addition, to satisfy the isolation requirement, the microstrip strips are fixed to a suitable electrical length [8].

The final values of presented single-balanced diode mixer design parameters are specified in Table 1.

Table 1: The final dimensions of the designed single-balanced diode mixer

Param.	mm.	Param.	mm.	Param.	mm.
W_f	10	L_f	1	W_1	12
L	18	W_1	14	L_1	16
W_T	1	L_T	12	W_{T1}	1
L_{T1}	1	L_4	1	d	5
L_z	8	L_d	2	Wz1	12
Wz2	2	Wz	15	Wz3	1
Lz1	4	W_{sub}	30	L_{sub}	71
W_{P1}	4	L_{P1}	6	W_{P2}	3
L_{P2}	2	W_{P3}	6	L_{P3}	14
W_{P4}	3	L_{P4}	1	L_g	10
W_{g1}	6	W_{g2}	8	W_{g3}	4
W_T	2	L_T	2	W_{T1}	6
L_g	10	W_{g1}	6	W_{g2}	8
W_{g3}	4	W_{r1}	2	L_{r1}	2
W_{r2}	6	L_{r2}	2		

III. MIXER COMPONENTS DESIGN

A. Design of branch-line coupler

Microwave branch-line coupler is one of the fundamental building blocks for balanced mixers. The schematic of the proposed branch-line coupler is shown in Fig. 2. This presented microstrip coupler was designed on a Rogers RT/Duroid 5880 substrate with 0.635 mm in thickness and with a relative dielectric constant of 2.2. The lines between the ports show the phase shift between them. This component has a 90 degree phase delay between ports 2 and 4 and between ports 1 and 3.

Ports 1 and 2 and ports 3 and 4 are mutually isolated pairs. The presented structure consists of a branch-line with four protruded T-shaped strips and a ground plane. As shown in Fig. 3, the proposed coupler can obtain excellent isolation 33 dB at 2.4 GHz [9]-[10].

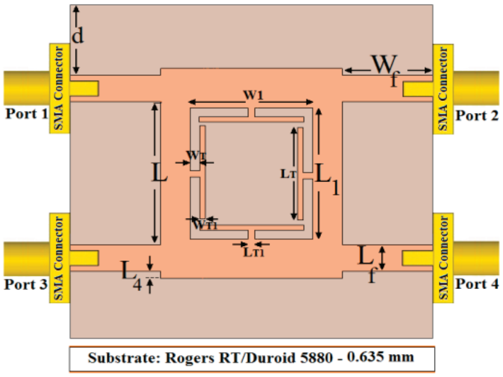

Fig. 2. Schematic of proposed branch-line coupler with four protruded T-shaped strips.

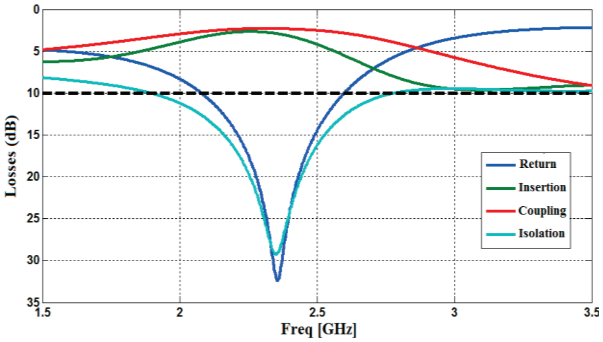

Fig. 3. Simulated losses for the proposed coupler.

B. Design of matching circuit

The matching circuits are designed to get minimum reflection coefficient at the diodes input. The analytical design of the input matching circuits is performed using the developed computer program [12]. The impedance transforming properties of transmission lines [13] can be used in the matching networks. A microstrip line can be used as a series transmission line, together with a short or open circuited shunt stub can transform a 50 Ω resister into any values impedance. We designed a series transmission line with open stub, and the series transmission line with short stub is chosen. Matching schematic for single-balanced diode mixer is shown in Fig. 1. Length of open circuit series stub (50 Ω) = 12.4569 mm, and width of open circuit series stub = 0.9 mm, length of balanced shunt stub (50 Ω) = 6.318 mm, width of balanced shunt stub = 0.9 mm.

C. Microstrip low-pass filters by using DGS structre with folded T-shaped arms

In this paper, two novel low-pass filters using Defected Ground Structure (DGS) slot with a pair of folded T-shaped arms are presented. The resonant frequency of the slot can be easily controlled by changing the folded T-shaped dimensions, without changing the area taken by the structure. Using this slot, two quasi-elliptic low-pass filters were designed, fabricated and tested. The experimental results show good agreement with simulation results and demonstrate that excellent stop-band performance could be obtained through the proposed low-pass filter. The filter has a cut-off frequency of about 2.4 GHz.

Defected Ground Structure (DGS) evolved from Photonic Band Gap (PBG) is realized by etching defected pattern and slot in the ground plane. The etched defect in ground plane disturbs the shield current distribution in the ground plane. This disturbance can increase the effective capacitance and inductance of a transmission line respectively. Thus, an LC equivalent circuit can represent the proposed unit DGS circuit [14]. The proposed DGS slot is shown in Fig. 2. The slot is etched in the ground metallization under the microstrip line. This slot has a major advantage in providing tighter capacitive coupling to the line in comparison to known microstrip DGS structures. Moreover, the resonant frequency of the structure can be controlled by changing the distance between the folded T-shaped arms. The resonant frequency of the slot can also be modified by changing the overall slot size this slot, however, shifts the cut-off frequency of the filter down. To shift the cut-off frequency back, it is necessary to reduce the inductance of the narrow stripline that is located over the slot. This can easily be done by increasing the width of the strip [14].

The microstrip low-pass filter, Fig. 4, was designed on both substrate sides by opening apertures in the ground metallization under the high-impedance transmission line. Replacing some of the apertures by the proposed folded T-shaped arms structure introduces transmission zeroes. The number of transmission zeroes is equal to the number of apertures with folded T-shaped arms.

Figure 5 shows the top and bottom layouts of the designed filter with central aperture replaced by the proposed folded T-shaped arms structure. Figure 6 shows the measured and simulated return and insertion loss of the filter. As shown in Fig. 6, a transmission zero, which improves behavior of the filter stop band, is observed at 6.42 GHz.

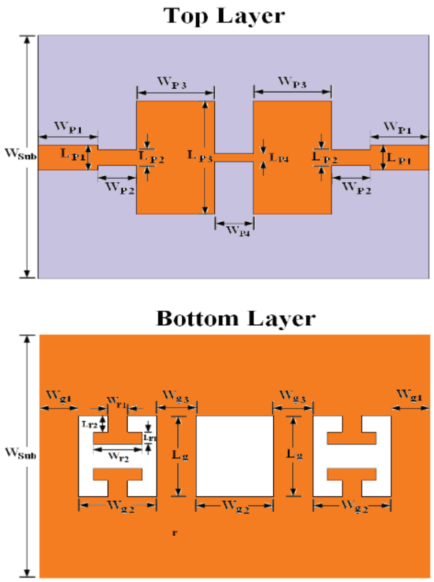

Fig. 4. Top and bottom layouts of a fifth-order low-pass filter with two DGS slots with folded T-shaped arms.

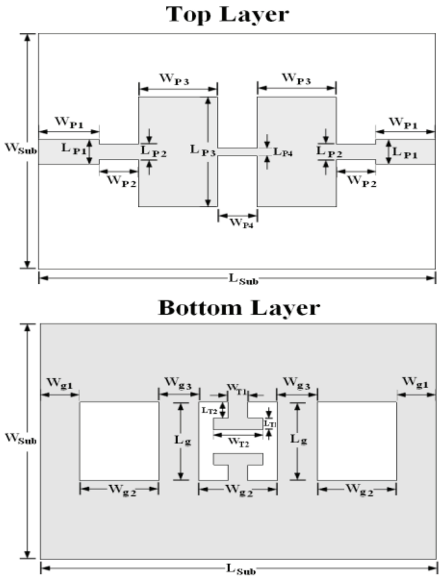

Fig. 5. Top and bottom layouts of a fifth-order low-pass filter with one DGS slot with folded T-shaped arms.

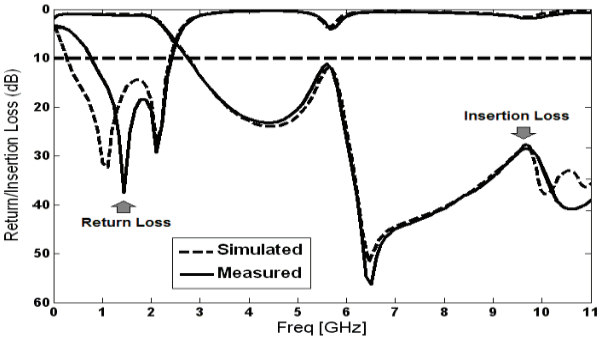

Fig. 6. Return and insertion loss of a fifth-order low-pass filter with one transmission zero.

In order to improve the stop-band behavior of filter responses, two rectangular slots with T-shaped arms inserted in the positions of the two apertures, as shown in Fig. 4. Another important parameter of this structure is the exterior length of the T-shaped open stubs L_{r1}. Figure 7 shows the insertion loss for different values of L_{r1}. It is found that by inserting the four T shaped strip of suitable dimensions at the ground plane, additional transmission zero at 10 GHz is created and hence much wider insertion loss bandwidth with multi transmission zeros can be produced, especially at the higher band.

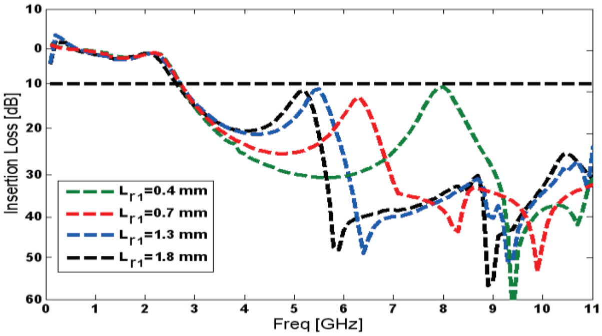

Fig. 7. Simulated insertion loss characteristics for various values of L_{r1}.

The proposed filter with optimal design, as shown in Fig. 8, was built and tested in the Antenna Measurement Laboratory at Iran Telecommunication Research Center (ITRC). Figure 6 shows the simulated and measured insertion and return loss of the filter. As shown in Fig. 9, two transmission zeros are introduced to the filter response at about 5.28 and 8.72 GHz. Consequently, a wide stop-band was achieved.

Additionally, the proposed DGS low-pass filter also has characteristics of wider and deeper stop-band than those of conventional low-pass filters [15]. In order to confirm the accurate measurement characteristics for the designed structure, it is recommended that the manufacturing and measurement processes need to be performed carefully. Moreover, SMA soldering accuracy and substrate quality need to be taken into consideration.

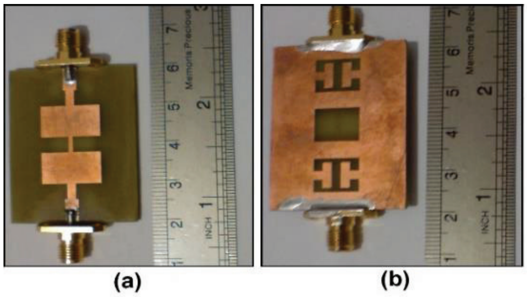
(a) (b)

Fig. 8. Top (above) and bottom (below) layouts of fabricated low-pass filter.

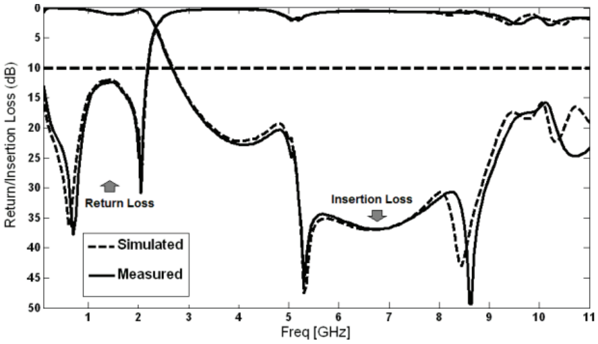

Fig. 9. Return and insertion loss of a fifth-order low-pass filter with two transmission zeroes.

IV. SINGLE-BALANCED DIODE MIXER MEASURMENTS

The proposed single-balanced diode mixer design, as shown in Fig. 10, was built and tested. For finding power spectrum in ADS simulator, we must edit equation for finding power at output port shown below:

$$P_{Out}(dBm) = 10\log(0.5 \times real(V_{load} \times conj(L_{load} \times i))) + 30\,, \quad (1)$$

P_{out}(dBm) is a power output at IF port in unit dBm, V_{load} is a voltage at output load at IF port, and I_{load} is a current at output load.

When we apply three design parts for single balanced diode mixer using DGS shown in Fig. 1, the power spectrum of mixer generate input RF at 2.448 GHz with power -10 dBm and input LO at 2.168 GHz with power 0 dBm.

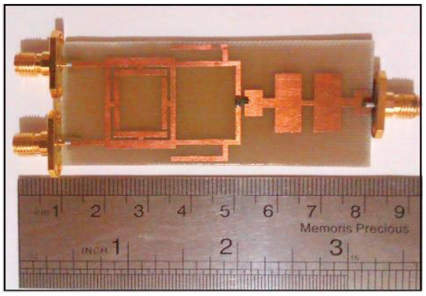

Fig. 10. Photograph of the realized single-balanced diode mixer.

For measured output power spectrum, the first sweep generator set at RF signal of 2.448 GHz with power -10 dBm and connected to RF port of mixer, then feed on LO signal of 2.168 GHz with power 0 dBm and connected to LO port of mixer. Output port is connected to the spectrum analyzer. The IF spectrum is shown in Fig. 11.

The port to port isolation parameters define how much signal leakage occurs between pairs of ports. LO to RF, LO to IF and RF to IF are shown in Fig. 12. LO to RF isolation is lower than -28 dB, LO to IF isolation is lower than -20 dB and RF to IF is lower than -37 dB.

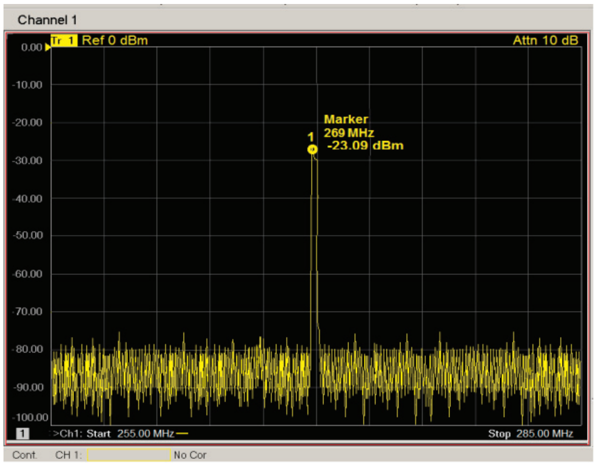

Fig. 11. Measurement of IF power spectrum of the proposed mixer.

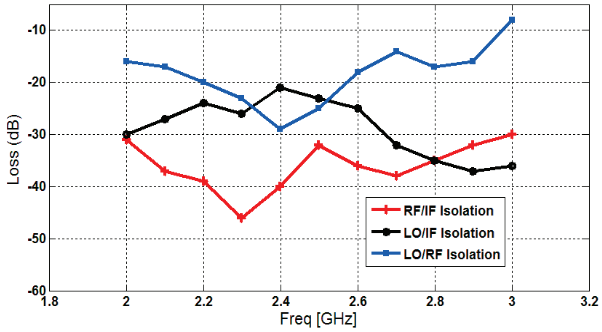

Fig. 12. Port to port isolation (LO to RF, LO to IF and RF to IF).

V. CONCLUSION

As presented above, a novel design of a down-conversion single-balanced diode mixer using defected structures for WLAN applications has been designed. By using four C-shaped slots in top and bottom arms in the branch-line coupler, an excellent isolation -33 dB at 2.4 GHz can be achieved. Also in this paper, two compact quasi-elliptic low-pass filters by using novel DGS slot with folded T-shaped arms are designed and fabricated. A mixer circuit was designed by using a simulator to design ADS, in part of DGS design by HFSS and export S-parameter for using in ADS simulator for design mixer circuit. The measurement of power spectrum of mixer was performed using spectrum analyzer. The mixer design based on the defected structures concept has been shown to provide an efficient and successful method for designing high isolation and compact systems.

ACKNOWLEDGMENT

This work is supported by Ardabil Branch, Islamic Azad University, Ardabil, Iran.

REFERENCES

[1] A. R. Rofougaran, M. Rofougaran, and A. Behzad, “Radios for next-generation wireless networks,” *IEEE Microwave Magazine*, 6, March 2005, pp. 38-43.

[2] C. Florian, F. Scappaviva, M. Feudale, V. A. Monaco, and F. Filicori, “A V band singly balanced diode mixer for space application,” *13th Gass® Symposium-Paris*, vol. 54, 2005, pp. 441-444.

[3] A. Dal, P. Jun-Seok, K. Chul-Soo, K. Juno, Y. Quian, and T. Itoh, “A design of the low-pass filter using the novel microstrip defected ground structure,” *IEEE Transaction on Microwave Theory & Techniques*, vol. 49, no. 1, January 2001, pp. 86-89.

[4] L. Hai-Wen, L. Zheng-Fan, S. Xiao-Wei, and M. Jun-Fa, “An improved 1-D defected ground structure for microstrip line,” *IEEE Microwave and Wireless Component Letters*, vol. 14, no. 4, April 2004, pp. 624-627.

[5] G. Gonzalez, *Microwave Transistor Amplifiers Analysis and Design*. 2nd ed., New Jersey: Prentice Hall, 1984.

[6] Advanced Design System (ADS), Agilent Corporation, 2009.

[7] Ansoft High Frequency Structure Simulation (HFSS), ver. 13, Ansoft Corporation, 2010.

[8] B. Catli and M. M. Hella, “A low-power dual-band oscillator based on band-limited negative resistance,” *IEEE Radio Frequency Integrated Circuits (RFIC) Symposium*, June 2009, pp. 251-254.

[9] F. Ferrero, C. Luxey, R. Staraj, G. Jacquemont, and V. F. Fusco, “Compact quasi-lumped hybrid coupler tunable over large frequency,” *Electron. Lett*., 2007, 43, (19), pp. 1030-1031.

[10] L. Marcaccioli, C. Lugo, M. M. Tentzeris, J. Papapolymerou, and R. Sorrentino, “A novel reconfigurable coupler for intelligent SOP RF front-ends,” *Proc. European Microwave Conf*., Paris, France, October 2005, vol. 1, pp. 4-6.

[11] V. Stoiljkovic, S. Suganthan, and M. Benhaddou, “A novel dualband center-fed printed dipole antenna,” *in Proc. IEEE Antennas Propag. Soc. Int. Sympi*., 2, (2003), 938-941.

[12] Y. Dakeya, T. Suesada, K. Asakura, N. Nakajima, and H. Mandai, “Chip multiplayer antenna for 2.45 GHz-band application using LTCC technology,” *Int. IEEE MTT-S Microwave Symp. Dig*., 3, (2000), 1693-1696.

[13] J. Mazloum, A. Jalali, and M. Ojaroudi, “Miniaturized reconfigurable band-pass filter with electronically controllable for WiMAX/WLAN applications,” *Microwave and Optical Technology Letters*, 56, (2), pp. 509-512, 2014.

[14] A. Faraghi, M. Ojaroudi, and N. Ghadimi, “Compact microstrip low-pass filter with sharp selection characteristics using triple novel defected structures for UWB applications,” *Microwave and Optical Technology Letters*, 56, (4), pp. 1007-1010, 2014.

[15] A. Faraghi, M. N. Azarmanesh, and M. Ojaroudi, “Small microstrip low-pass filter by using novel defected ground structure for UWB applications,” *ACES Journal*, vol. 28, no. 4, pp. 341-347, April 2013.

Dual-Band Compact Array of Printed Dipole Antennas

Mahmood Rafaei-Booket [1] and Amir Jafargholi [2]

[1] School of Electrical and Computer Engineering
Tarbiat Modares University (TMU), Jalal Ale Ahmad Highway, P.O. Box: 14115-111, Tehran, Iran
mahmood.rafaeibooket@modares.ac.ir

[2] Institute of Space Science and Technology
Amirkabir University of Technology, 424 Hafez Ave., P.O. Box: 15875-4413, Tehran, Iran
jafargholi@ieee.org

Abstract **─** Compact array of printed dipole antennas loaded with reactive elements is proposed. A novel and practical applications of the metamaterial (MTM) inclusion in dipole antenna designs is presented. The simulation results show a reasonable reduction in mutual coupling between antenna elements and provide a possible way to reduce the element separation. A prototype of the proposed array antenna is fabricated and tested. Measurement shows that the isolation with inter-antenna spacing of less than 0.075λ (at f=0.9 GHz) through the first frequency band (811 MHz–955 MHz) is above 12.5 dB, while the proposed design provides more than 15 dB isolation with inter-antenna spacing of less than 0.133λ at f=1.6 GHz (1325 MHz–1880 MHz).

Index Terms **─** Compact array, printed dipole antenna.

I. INTRODUCTION

The increasing demands on compact multifunctional devices have necessitated the development of miniaturized/multi-frequency printed dipoles which can be integrated into familiar devices such as laptop computers and mobile phones [1]. Due to unique electromagnetic properties [2-6], MTMs have been widely considered in monopole and dipole antennas to improve their performance [7-12].

The applications of composite right/left handed (CRLH) structures to load the printed dipole have been investigated both numerically [13] analytically [14], and experimentally [15 and 16]. However, main drawbacks of this method are low gain and low efficiency.

In the field of array antenna, there is a great interest to reduce the array size while it may be worked properly. Due to increasing mutual coupling effects in such compact array antennas, one of the researcher interests is to reduce mutual coupling between densely packed array elements, so that array elements can be designed separately, without consideration of mutual coupling arising from neighboring elements. The strong mutual coupling between array elements imposes a tremendous limitation on the practical packing density of arrays.

There are various methods that can be utilized to improve array isolation, using EBG structures [17-19], defected ground structure (DGS) [20], coupling element [21], using meta-surface [22], modified ground plane [23], artificial substrate [24], slotted-complementary split-ring resonators (SRR) [25], soft-surface [26], and MTM isolator [27 and 28].

However, in all mentioned methods, the designer has to make changes in antenna ground plane or using additional structures. These changes increase the complexity as well as time and cost factors of design and manufacturing processes.

In [9], a compact printed dipole antenna is proposed using reactive loading, which is inspired by ENG-MTM inclusions. The antenna has a broad bandwidth which is significantly wider than the bandwidth of other miniaturized MTM loaded dipole antennas. Due to enhancement of both antenna gain and bandwidth in [9], one may chose

Submitted On: August 21, 2013
Accepted On: December 11, 2014

it as a good candidate for compact, broadband array antennas.

Using the compact printed dipole antenna of [9] as an element of a simple linear array antennas, in contrast to all mentioned methods, the proposed miniaturized array provides isolation enhancement, without need to make any change in ground plane or using any additional structure. This fact consequently leads to simple low profile, low cost and low weight array antennas. A prototype of the proposed antenna is fabricated and tested. It is found that the proposed method may result more than 12.5 dB isolation with inter-antenna spacing of less than 0.075λ at f=0.9 GHz and 0.133λ at f=1.6 GHz (25 mm) demonstrating that significant improvement in isolation between antenna elements can be obtained. The commercial software Ansoft HFSS is adopted for the simulations. The numerical simulation results show good agreement with the measurements.

II. ANTENNA DESIGN, SIMULATION AND FABRICATION

An array of closely spaced loaded dipole antenna which is also worked with reduced mutual coupling is presented here. It is well-known that the dipole antennas exhibit significant mutual effects when they implemented in side-by-side arrangement. These effects are much higher than collinear configuration, since in side-by-side arrangement, the antennas are placed in the direction of maximum radiation [1]. Hence, in this paper, the side-by-side arrangement is used to show the effects of proposed method on the correlation coefficients.

As described in [9], to miniaturize a printed dipole antenna, someone may use a reactive loading method based on ENG-MTM inclusions. The behavior of a dipole antenna loaded with MTM inclusions has been examined in [9]. It has been revealed that embedding epsilon negative (ENG)-inclusions in a simple dipole antenna can provide an opportunity to design miniaturized/multi-band antenna. Results show that placing proposed MTM cells in close proximity of a printed dipole antenna makes it miniaturized. The dimensions of the proposed MTM cell is optimized to meet the specifications of the mobile bands (890.2 MHz–914.8 MHz, and 1710 MHz–1784 MHz) while maintaining its compact size.

The antenna radiation efficiency at the first resonance frequency is significantly higher than those reported for other miniaturized printed dipoles in the literature [13]. It is worthwhile to point out here that the subject of single-cell MTM loading is not new and has been studied by other authors [15].

In [9, Fig. 2], the return loss of symmetrically loaded and unloaded dipole antennas is shown. The proposed antenna has a broad bandwidth of 15.96% at 940 MHz (which is significantly wider than the bandwidth of other miniaturized MTM loaded dipoles [14]) and 32.35% at 1.7 GHz.

According to [9], again the array is considered to print on a FR4 substrate with a thickness of 0.8 mm and a dielectric constant of 4.4. All the dimensions are the same as the antenna described in [9]. Figure 1 (a) and Fig. 1 (b) show a single cell MTMs and array element respectively. The printed dipole array is fabricated to validate the simulation results, (see Fig. 2). Figure 1 (c) shows a photograph of the fabricated array antenna.

According to Fig. 2, the dipole array antenna along with the loading elements provides good matching at both expected frequency bands. In Fig. 2 (a), although the simulated and measured results are in reasonable agreement, slight frequency shift in some frequencies is observed. Frequency shift in microstrip antenna may be attributed to the fabrication process and dielectric constant tolerance in a frequency regime. This phenomenon is more critical in multiband microstrip antenna which was observed in copious previous works. From the measurement result, the isolation and the 10 dB return-loss bandwidth at first resonance frequency (0.9 GHz) are above 12.5 dB and 144 MHz (16.3%) respectively. It is found that the design may provide more than 15 dB isolation with inter-antenna spacing of less than 0.133λ at f=1.6 GHz (25 mm), demonstrating that significant improvement in isolation between antenna elements can be obtained.

The simulation results for the antenna gain and radiation efficiency are also illustrated in Fig. 2 (b). It seems clear that the antenna radiation efficiency is high through the entire frequency band (>75%). Moreover, the gain of the proposed antenna is about -5 to -2 dBi. As revealed in this figure, the antenna radiation is good while it matched through the broad band frequency.

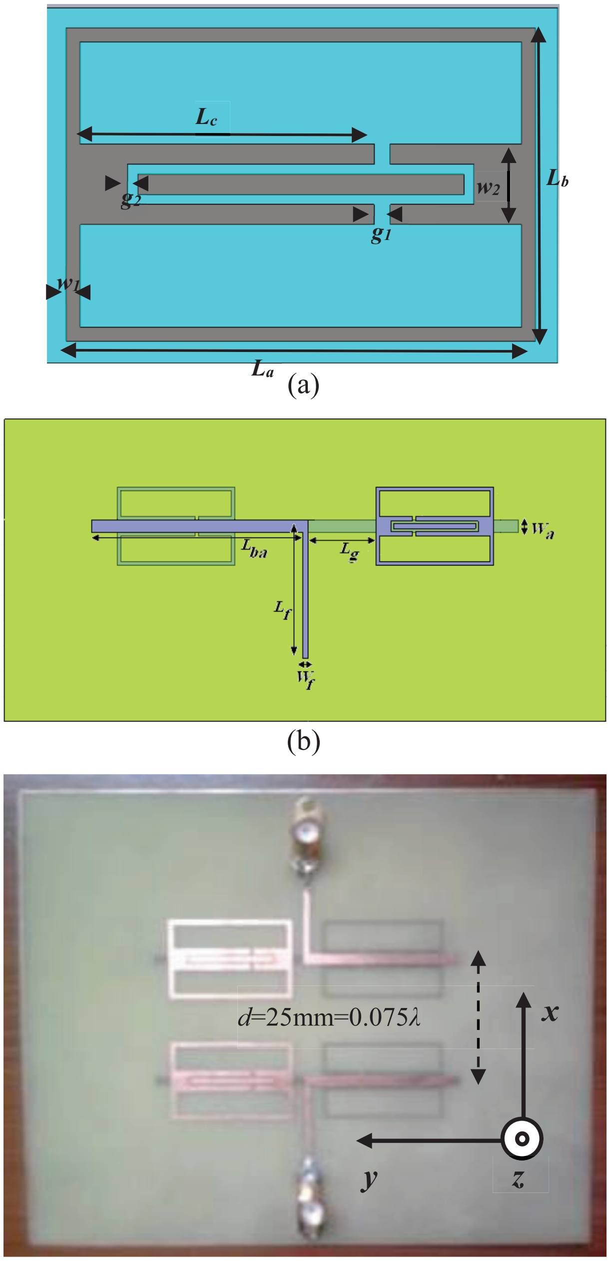

(a)

(b)

(c)

Fig. 1. Array of printed dipoles symmetrically loaded with single cell MTM: (a) single cell parameters: L_a=23.54 mm, L_b=15.55 mm, L_c=14.78 mm, w_1=0.7 mm, g_1=0.8 mm, w_2=4 mm, g_2=0.5 mm, L_s=26.75 mm, and w_s=2.5 mm as the width of the antenna arms; (b) antenna element, [9]: L_{ba}=42.05 mm, L_f=27.5 mm, L_g=12.52 mm, W_a=2.5 mm, W_f=0.8 mm; (c) prototype: d=25 mm≈0.075λ at f=0.9 GHz and ≈0.133λ at f=1.6 GHz.

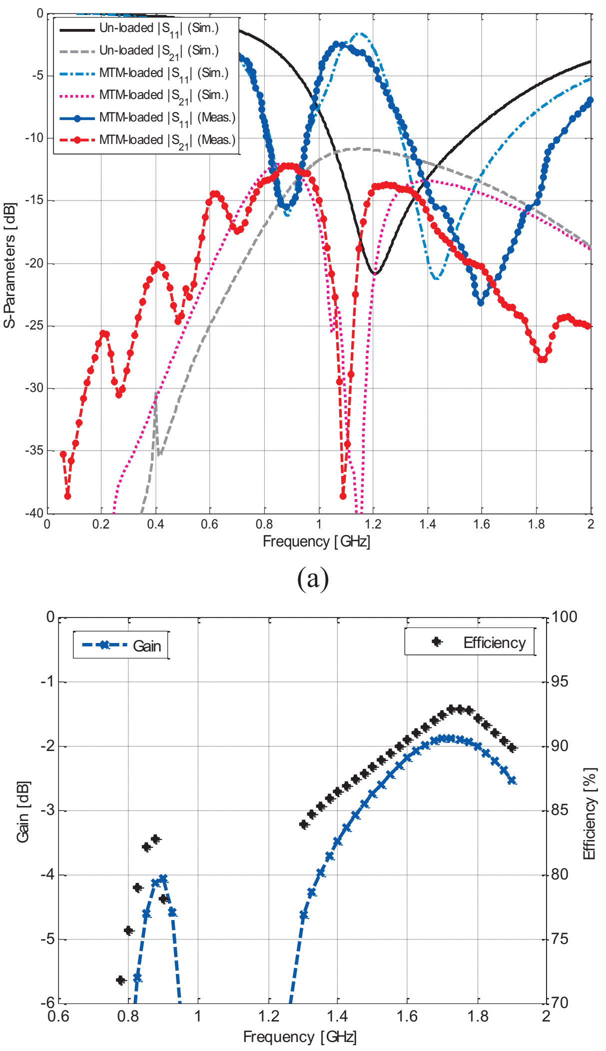

(a)

(b)

Fig. 2. (a) Return loss and isolation of array of printed dipoles unloaded and symmetrically loaded with single cell MTM, simulation and measurements comparison, and (b) gain and radiation efficiency of the printed dipoles symmetrically loaded with single cell MTM.

In Fig. 3, the simulation results of reflection and correlation coefficients of an array of printed dipoles symmetrically loaded with single cell MTM, versus frequency with regards to array element distance, d, has been depicted. Comparing simulation results with un-loaded dipole array antennas, Fig. 2 (a), it is clear that, MTM loaded array shows a dual band behavior while the antenna isolation is enhanced at least 5 dB. The isolation may enhance about 10 dB while the array distance increases as it is shown at 32 mm (0.096λ).

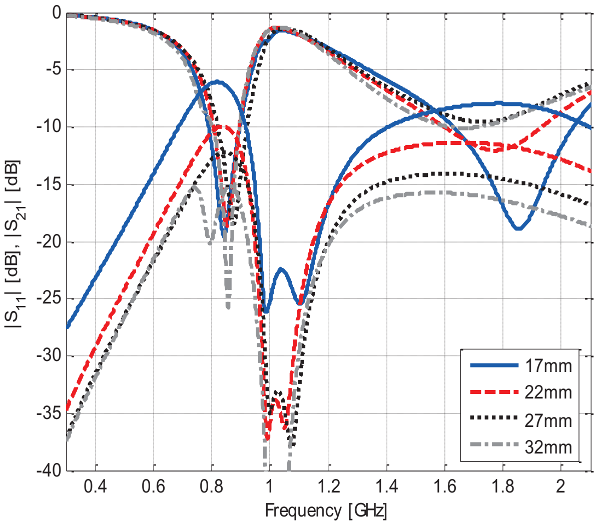

Fig. 3. Simulation results of reflection and correlation coefficients of an array of printed dipoles symmetrically loaded with single cell MTM, versus frequency with regards to array element distance, *d*.

It should be noted that, although in side-by-side arrangement, the distance between the antennas are usually considered as arms separation (25 mm≈0.075λ); here, due to significant coupling between MTM cells, someone may consider the inter-antenna spacing of 10.5 mm (0.0315λ). This fact is depicted in Fig. 4.

However, using MTM cells, the correlation between the ports is decreased. This phenomenon is clearly seen in Fig. 4, while it seems that the surface current confined around the arms of dipoles and MTM cell regions. This causes to reduce coupling factor between loaded printed dipoles. This fact is confirmed when comparing the radiation pattern of loaded and un-loaded dipole array antennas, Figs. 5 and 6. The radiation patterns for each port of un-loaded array antennas have been shown in Fig. 5. The maximum gain of the antennas are about -8 and -7 dBi at *f*=0.9 GHz and *f*=1.6 GHz respectively, while its cross-polarizations are about 14 and 22 dB lower than its main lobes. The radiation patterns of each port of array of MTM loaded printed dipole antennas are also shown in Fig. 6. The maximum gain of the antennas are about -4 and -2 dBi at *f*=0.9 GHz and *f*=1.6 GHz respectively. The cross-polarization levels at these frequencies are about 20 and 25 dB lower than their main lobes which are better than un-loaded printed antennas. Moreover, reducing surface current causes to increase radiation gain in the case of MTM loaded printed dipole antennas.

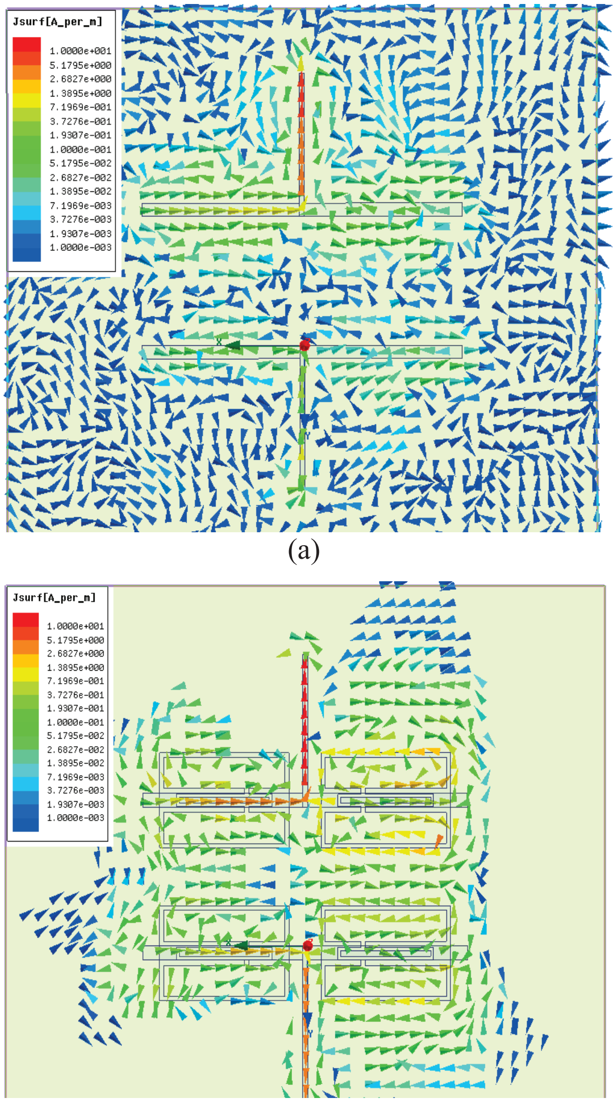

(a)

(b)

Fig. 4. Simulation results for the vector surface current of the array of printed: (a) un-loaded, and (b) symmetrically loaded with single cell MTM dipoles at *f*=0.9 GHz.

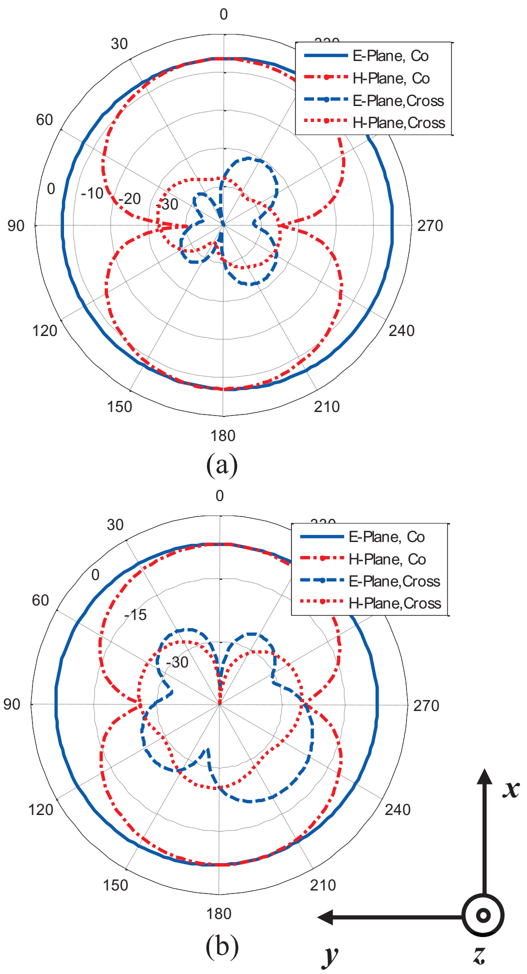

(a)

(b)

Fig. 5. Simulation results for the radiation pattern of the array of printed dipoles for both Co- and Cross- polarizations, *f*=0.9 GHz at: (a) port 1, and (b) port 2.

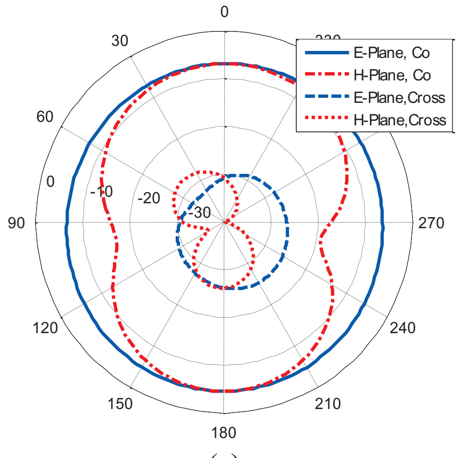

(a)

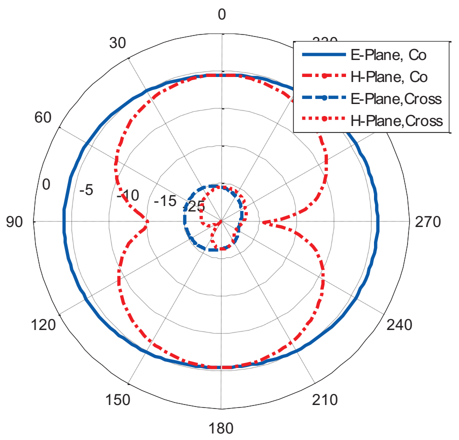

(b)

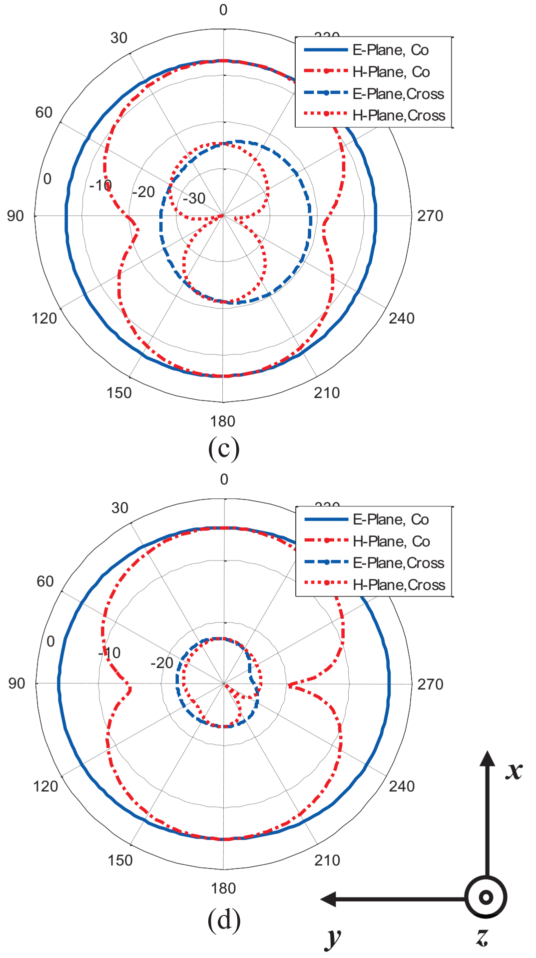

(c)

(d)

Fig. 6. Simulation results for the radiation pattern of the array of printed dipoles symmetrically loaded with single cell MTM for both Co- and Cross-polarizations at port 1: (a) *f*=0.9 GHz, and (b) *f*=1.6 GHz; and at port 2: (c) *f*=0.9 GHz, and (d) *f*=1.6 GHz.

III. CONCLUSION

A compact printed array of dipole antenna has been proposed. The proposed antenna provides isolation enhancement, without need to make any change in ground plane or using any additional structure. This fact consequently leads to simple low profile, low cost and low weight array antennas. Simulations show that the proposed array antenna provides isolation above 15 dB with inter-antenna spacing of less than 0.075λ. A prototype of the proposed array antenna is fabricated and tested. The simulation results have been confirmed by measurements.

REFERENCES

[1] C. A. Balanis, *Advanced Engineering Electromagnetics*, New York: Wiley, 1989.

[2] M. Rafaei Booket, M. Veysi, Z. Atlasbaf, and A. Jafargholi, "Ungrounded composite right/left handed metamaterials: design, synthesis, and applications," *IET Microwave Antenna Propag*., vol. 6, no. 11, pp. 1259-1268, 2012.

[3] M. Veysi and A. Jafargholi, "Directivity and bandwidth enhancement of proximity-coupled microstrip antenna using metamaterial cover," *Applied Computational Electromagnetics Society, ACES Journal*, vol. 27, no. 11, pp. 925-930, Nov. 2012.

[4] A. Jafargholi and A. Jafargholi, "Ultrawide-band negative refraction based on moving media concept," *Applied Computational Electromagnetics Society, ACES Journal*, vol. 27, no. 11, pp. 931-937, Nov. 2012.

[5] M. Veysi, M. Kamyab, S. M. Mousavi, and A. Jafargholi, "Wideband miniaturized polarization dependent HIS incorporating metamaterials," *IEEE Antennas Wireless Propag. Lett*., vol. 9, 764-766, 2010.

[6] M. Veysi, M. Kamyab, J. Moghaddasi, and A. Jafargholi, "Transmission phase characterizations of metamaterial covers for antenna application," *Progress In Electromagnetic Research Letter*, vol. 21, 49-57, 2011.

[7] Q. Liu, P. S. Hall, and A. L. Borja, "Efficiency of electrically small dipole antennas loaded with left-handed transmission lines," *IEEE Trans. Antennas Propag*., vol. 57, no. 10, 3009-3017, 2009.

[8] A. Jafargholi, M. Kamyab, M. Rafaei, and M. Veysi, "A compact dual-band printed dipole antenna loaded with CLL-based metamaterials," *International Review of Electrical Engineering*, vol. 5, no. 6, 2710-2714, 2010.

[9] M. Rafaei Booket, A. Jafargholi, M. Kamyab, H. Eskandari, M. Veysi, and S. M. Mousavi, "A compact multi-band printed dipole antenna loaded with single-cell MTM," *IET Microwave Antenna Propag*., vol. 6, no. 1, pp. 17-23, 2012.

[10] A. Jafargholi, M. Kamyab, and M. Veysi, "Artificial magnetic conductor loaded monopole antenna," *IEEE Antennas Wireless Propag. Lett*., vol. 9, pp. 211-214, 2010.

[11] A. Jafargholi and M. Kamyab, "Dipole antenna miniaturization using single-cell metamaterial," *Applied Computational Electromagnetics Society, ACES Journal*, vol. 27, no. 3, pp. 261-270, Mar. 2012.

[12] A. Jafargholi and M. Kamyab, "Full-wave analysis of loaded dipole antennas using mode-matching theory," *Applied Computational Electromagnetics Society, ACES Journal*, vol. 26, no. 11, 915-921, 2011.

[13] H. Iizuka and P. S. Hall, "Left-handed dipole antennas and their implementations," *IEEE Trans. Antennas Propag*., vol. 55, no. 5, 1246-1253, May 2007.

[14] M. R. Booket, M. Kamyab, A. Jafargholi, and S. M. Mousavi, "Analytical modeling of the printed dipole antenna loaded with CRLH structures," *Progress In Electromagnetics Research B*, vol. 20, 167-186, 2010.

[15] J. Zhu, M. A. Antoniades, and G. Eleftheriades, "A compact tri-band monopole antenna with single-cell metamaterial loading," *IEEE Trans. Antennas Propag*., vol. 58, no. 4, 1031-1038, Apr. 2010.

[16] N. Amani, M. Kamyab, and A. Jafargholi, "Compact, dualband t-junction zeroth-order resonant antenna with extended bandwidth," *21st Iranian Conference on Electrical Engineering, ICEE*, May 2013.

[17] C. Caloz, H. Okabe, T. Iwai, and T. Itoh, "A simple and accurate model for microstrip structures with slotted ground plane," *IEEE Microwave Wireless Comp. Lett*., vol. 14, no. 4, pp. 133-135, Apr. 2004.

[18] E. R. Iglesias, Ó. Q. Teruel, and L. I. Sánchez,

"Mutual coupling reduction in patch antenna arrays by using a planar EBG structure and a multilayer dielectric substrate," *IEEE Trans. Antennas Propag.*, vol. 56, no. 6, 1648-1655, Jun. 2008.

[19] F. Yang and Y. Rahmat-Samii, "Microstrip antennas integrated with electromagnetic band-gap (EBG) structures: a low mutual coupling design for array applications," *IEEE Trans. Antennas Propag.*, vol. 51, no. 10, 2936-2946, Oct. 2003.

[20] V. Lucarini, J. J. Saarinen, K.-E. Peiponen, and E. M. Vartiainen, "Kramers-Kronig relation in optical materials research," *Springer Series in Optical Sciences*, 2004.

[21] A. C. K. Mak, C. R. Rowell, and R. D. Murch, "Isolation enhancement between two closely packed antennas," *IEEE Trans. Antennas Propag.*, vol. 56, no. 11, 3411-3419, Nov. 2008.

[22] E. Sáenz, I. Ederra, R. Gonzalo, S. Pivnenko, O. Breinbjerg, and P. de Maagt, "Coupling reduction between dipole antenna elements by using a planar meta-surface," *IEEE Trans. Antennas Propag.*, vol. 57, no. 2, 383-394, Feb. 2009.

[23] C. Chiu, C. Cheng, R. D. Murch, and C. R. Rowell, "Reduction of mutual coupling between closely-packed antenna elements," *IEEE Trans. Antennas Propag.*, vol. 55, no. 6, 1732-1738, Jun. 2007.

[24] I. Ederra, B. Pascual, A. Labajos, J. Teniente, R. Gonzalo, and P. de Maagt, "Experimental verification of the reduction of coupling between dipole antennas by using a woodpile substrate," *IEEE Trans. Antennas Propag.*, vol. 54, no. 7, 2105-2112, 2006.

[25] M. M. Bait-Suwailam, O. F. Siddiqui, and O. M. Ramahi, "Mutual coupling reduction between microstrip patch antennas using slotted-complementary split-ring resonators," *IEEE Antennas Wireless Propag. Lett.*, vol. 9, pp. 876-878, 2010.

[26] Ó. Q. Teruel, L. I. Sánchez, and E. R. Iglesias, "Soft surfaces for reducing mutual coupling between loaded PIFA antennas," *IEEE Antennas Wireless Propag. Lett.*, vol. 9, pp. 91-94, Sep. 2010.

[27] K. Sarabandi and Y. J. Song, "Subwavelength radio repeater system utilizing miniaturized antennas and meta-material channel isolator," *IEEE Trans. Antennas Propag.*, vol. 59, no. 7, 2683-2690, Jul. 2011.

[28] C. C. Hsu, K. H. Lin, and H. L. Su, "Implementation of broadband isolator using metamaterial-inspired resonators and a T-shaped branch for MIMO antennas," *IEEE Trans. Antennas Propag.*, vol. 59, no. 10, 3936-3939, Oct. 2011.

Mahmood Rafaei-Booket received the B.S. degree in Electrical Engineering from Urmia University (with honors), Urmia, Iran, in 2007 and the M.S. degree in Fields and Waves Communication Engineering from the Electrical Engineering Department from K. N. Toosi University of Technology (with honors), Tehran, Iran, in 2010. He is currently working towards the Ph.D. degree at Tarbiat Modares University, Tehran, Iran. For his Master's degree, he has done theoretical studies on the analysis of metamaterial structures loaded on the printed dipole antenna. From September 2008 to December 2009, he was working with Sharif University on various antenna designs, calculation of RCS as analytically. From April 2011 to March 2013, he was working with Iran Telecommunication Research Center in the design of GEO satellite antennas. In addition, he was involved in design and simulation of reflectarray antennas. In April 2013, he joined the Shahid Ghandi Research Center of K. N. Toosi University of Technology, where he is currently working on antenna miniaturization and cloaking techniques by using of metamaterial structures, anisotropic materials and Graphene. His research interests are diffraction analysis and numerical simulation of periodic structures with focus on metamaterials, Frequency Selective Surfaces, Graphene Absorbers, and Artificial Magnetic Conductors using Method of Moments and derivation of the dyadic Green's function for multilayer structures with anisotropic, chiral, bi-anisotropic, ferrite and periodic substrates.

Rafaei-Booket was first ranked student in B.S. and a recipient of the 13th Khawarizmi Youth Award on Oct. 2011. He received the Zanjan

University scholarship in 2013 and currently he is a University Lecturer in the Electrical and Computer Engineering Department of the Zanjan University.

Amir Jafargholi received the B.S., M.S. and Ph.D. degrees in Electrical Engineering from K. N. Toosi University of Technology, Tehran, Iran, in 2005, 2007 and 2011 respectively. During the first half of 2012, he was a Research Associate and in the same year he was appointed as an Assistant Professor in the Institute of Space Science and Technology, Amirkabir University of Technology, Iran. His research is generally in applied electromagnetic - and particularly in antennas, array and phased array antennas - for applications in wireless and satellite communications. At present, his interests focus on the applications of metamaterials in the analysis and synthesis of antennas and phased array antennas. He is the author of Metamaterials in Antenna Engineering, Theory and Applications (LAP Academic Publishing, Germany, 2011). He also has authored or co-authored over 30 journal papers, 3 book chapters and 40 refereed conference papers. He has supervised or co-supervised over 15 Ph.D. and M.Sc. theses.

Jafargholi was a recipient of a Student's Best Thesis National Festival award for his B.S. thesis, in May 2006. He was a recipient of the 22nd Khawarizmi International and 13th Khawarizmi Youth Award in Jan. 2009 and Oct. 2011, respectively. He was also the recipient of Research Grant Awarded in Metamaterial 2010. Jafargholi has been a member of the IEEE Antennas and Propagation Society since 2011. He is also a member of Iranian National Elite Foundation since 2011. Currently he is the Scientific Editor of the Journal of Electrical Industries.

Circularly Polarized Square Slot Antenna Using Crooked T-Shape Technique

Saeid Karamzadeh [1,3], Vahid Rafii [2], Mesut Kartal [3], and Morteza Dibayi [2]

[1] Department of Electric and Electronics Engineering
Istanbul Aydin University, Istanbul, Turkey
karamzadeh@itu.edu.tr

[2] Young Researchers and Elite Club, Urmia Branch
Islamic Azad University, Urmia, Iran
vhdrafiei@gmail.com, m.dibayi@gmail.com

[3] Department of Electric and Electronics Engineering
Istanbul Technical University, Istanbul, Turkey
kartalme@itu.edu.tr

Abstract **─** This paper presents the investigation results on a novel circularly polarized square slot antenna (CPSSA) designed to operate at a frequency of 5.5 GHz. In order to realize the proposed antenna, miniature circular polarized square slot antenna is used with L-shape and crooked T-shape grounded strips located at the slots opposite corners to reduce cross-polarization. The antenna is fed by coplanar waveguide. The 3 dB axial-ratio of the CPSSA extends to approximately 2 GHz. The CPSSA was designed to operate over the frequency range between 3 and 11.1 GHz corresponding to an impedance bandwidth of 115% for VSWR<2. Acceptable agreement between the simulation and measured results validates the proposed design.

Index Terms **─** Circularly polarized, coplanar waveguide feed, planar antenna, slot antenna.

I. INTRODUCTION

Recently, circularly polarized planar patch antennas have gain more attention in the field of wireless communication. CPW-fed print slot antennas have many advantages, such as low profile, lightweight, ease of integration and wider impedance bandwidth; moreover, circularly polarized is much superior to linearly polarized duo to its agility of choosing polarization at the receiving locations and have good performance of anti-interference in bad weather [1-15]. For generating circular polarization (CP) radiation using a single feed, many microstrip antenna designs have been reported [1-9]. The obtained CP bandwidth (3-dB axial-ratio bandwidth), however, is usually narrow and less than 2%. When the same microwave substrate is used, corresponding printed slot antennas usually have a much wider CP bandwidth than single-feed circularly polarized microstrip antennas [2].

To benefit from broadband and low profiles, various shapes and designs of broadband circularly polarized slot antennas have been developed to overcome both the narrow impedance and axial-ratio bandwidths (ARBWs) by applying different techniques on patch and ground structures [2-4]. In [9], by embedding two inverted-L-shaped grounded strips around two opposite corners of slot, circular polarization is obtained. The idea of embedding a T-shaped grounded metallic strip that is perpendicular to the axial direction of the CPW feed line is used in [4], and a corrugated slot antenna with a meander line is presented in [10]. In [11], a square slot antenna with a lightning-shaped feed line and inverted-L grounded strips is presented. To produce the circular polarization, the arc-shaped grounded metallic strip is utilized in [12-13].

In this letter, a novel design of a CPW-fed

Submitted On: May 22, 2013
Accepted On: October 20, 2014

circularly polarized square slot antenna composed of a square ground plane, an inverted-L-shape strips, two crooked T-strips and a vertical stub is presented. In this design, 3-dB AR bandwidth can reach as large as 2000 MHz (5-7 GHz) which is about 33.3%, to cover the WLAN/WiMAX band. The proposed design also has the VSWR≤2 impedance bandwidth of 8100 MHz (3-11.1 GHz) which is about 115%. Details of the proposed antenna design and experimental results of the broadband operation are presented. The proposed of this article is designed an ultra-wide band antenna with utilizing of novel methodology which can be provided broadband circular polarization. The simultaneous use of the crooked T-shape and L-shape techniques has readied the above conditions.

II. ANTENNA CONFIGURATION

The geometrical layout and photograph of the proposed CPW-fed broadband CPSS antenna is shown in Fig. 1. The proposed antenna is printed on a square microwave substrate FR4, with a side length of 25 mm, a thickness of 0.8 mm and a dielectric constant of relative permittivity ε_r=4.4. The antenna is fed by a 50 Ω CPW feeding line, where the signal strip and gaps have widths of 3.1 and 0.3 mm, respectively.

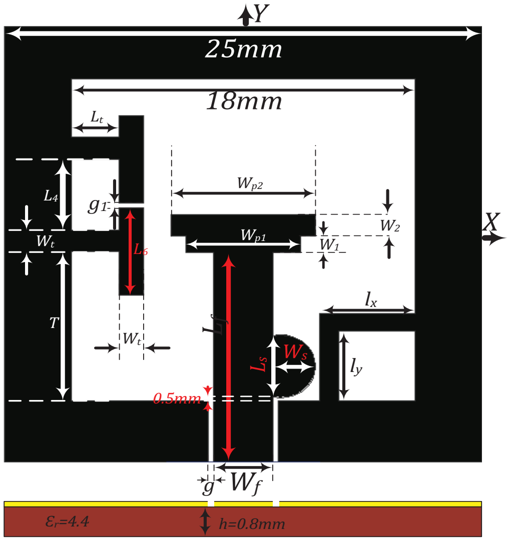

Fig. 1. Configuration of the proposed CPSSA structure. Dimensions of the structure's parameters are: W_f=3.1, L_f=8, g=0.3, h=0.8, W_t=1.25, W_{p1}=6, W_{p2}=7.6, L_s=3.5, W_s=3.5, g_1=0.4, L_4=4, W_1=1, W_2=1.2, L_t=2.5, l_x=5, l_y=4, L_6=4.5 (units in mm).

III. EXPERIMENTAL RESULTS AND DISCUSSION

The simulated CPSSA structures have been fabricated using conventional printed circuit board (PCB) techniques. In each step of the design procedure, the full-wave analyses of the proposed antenna were performed using Ansoft HFSS (ver.11) based on the finite element method (FEM) to find optimized parameters of the antenna structure [13].

As indicated in Fig. 2, five improved designs of the proposed CPSS antenna are presented. The antenna design is started by applying a simple strip feed line (step 1) and then improved through adding the vertical tuning stub formed by extending the feed section to the right (+y-direction) by a width of W_s=3.5mm and a length of L_s=3.5mm (step 2). Our simulations show that width (W_s) of the tuning stub has great effect on improving the impedance matching in the 3 dB AR band. A further improvement is achieved by adding two embedded rectangular strip patches with W_{p1}, W_{p2}, W_1 and W_2 dimensions (step 3). -10 dB impedance matching curves of the antenna are presented in Fig. 3. As it is observed from Fig. 3, by employing a simple strip as the feed line, a great impedance mismatch is experienced (step 1) and consequently, any bandwidth of the antenna under -10 dB is available.

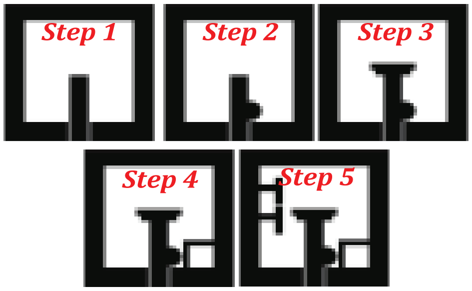

Fig. 2. Five improved prototypes of the antenna.

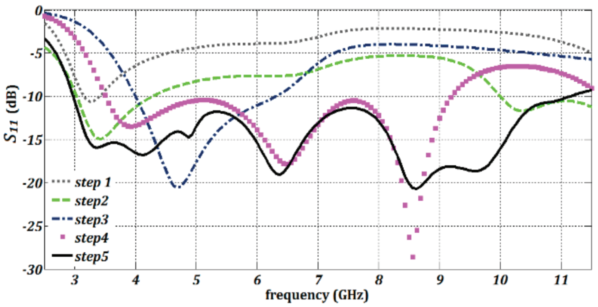

Fig. 3. Improved S_{11} of the antenna (step 1~5).

By adding the vertical tuning stub and two embedded rectangular strip patches on the feed line, antenna operates between 4~6.3 GHz. The simulation results show that embedding rectangular strip patches on the feed line (step 1 - step 5) and adjusting the parameters, an improvement on the impedance bandwidth as well as CP characteristic can be accomplished for the proposed antenna. To obtain CP operation by exciting two orthogonal polarizations, the design is improved by adding an inverted-L strip to the right bottom corner of the structure. This structure is presented as step 4 in Fig. 2. According to simulation results for step 4, we have found that choosing ly and lx of the inverted-L strips equal to 5 mm (0.275L), not only increases the ARBW but also improves impedance bandwidth. S_{11} variations of step 4 is presented in Fig. 3.

Considering the CP characteristic of the antenna, the changing regulation of the right hand side feed is similar to that of left hand side one. Through Fig. 4, it can be observed that by adding an inverted-L strip to the antenna structure, a small improvement in the axial ratio of the antenna is created and antenna operates CP about 2.6% (7.4~7.6 GHz). To further improve the CP characteristic of the antenna, two crooked T-shape strips are sequentially added to the structure (step 5). As it is seen from Fig. 3, adding two crooked T-shape strips to step 5 make the antenna operate UWB; and it can be seen in Fig. 4, that the ARBW of the antenna is increased to 5~7 GHz for step 5.

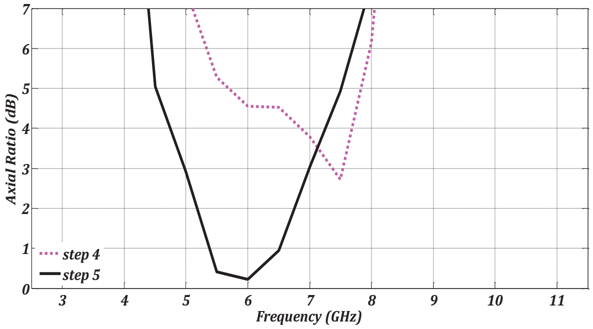

Fig. 4. Improved axial ratio of the antenna (step 4~5).

Through extensive simulations, it was found that length of the crooked T-shape strips (L_6) should be selected as 0.25L, and the distance between them (L_4) should be 0.22L, to attain the 33.3% ARBW. Changing the length or distance between these strips will degrade the axial ratio and subsequently CP characteristic of the antenna seriously. Considering Fig. 5, it is understood that increasing the distance of L_4 will decrease axial ratio bandwidth. The simulation results of surface current distribution for antenna in step 5 are shown in Fig. 6. As indicated in Fig. 6, the current distribution of proposed antenna at counterclockwise. It is observed that the surface current distribution in 180˚ and 270˚ are equaling magnitude and opposite in phase of 0˚ and 90˚. If the current rotates in the clockwise (CW) direction, the antenna can radiate the right-hand circular polarization (RHCP).

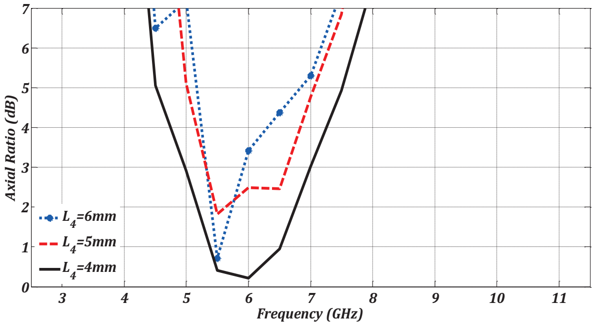

Fig. 5. Axial ratio for different value of L_4.

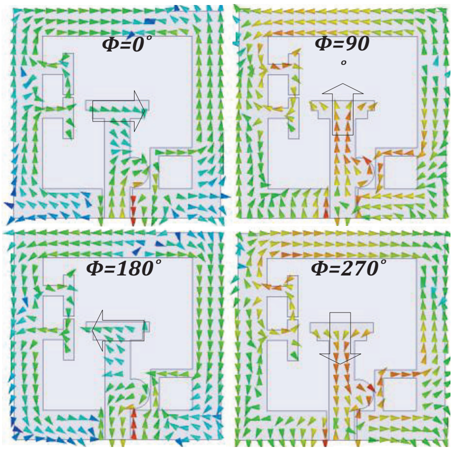

Fig. 6. Distribution of the surface current on the feed and ground of the CPSS antenna at 5.5 GHz in 0˚, 90˚, 180˚ and 270˚ phase.

An Agilent 8722ES vector network analyzer was used to measure S_{11} and impedance bandwidth for simplification in the antenna design. The simulated and measured S_{11} of the proposed antenna is shown in Fig. 7. As seen in Fig. 7, the simulated and measured impedance bandwidth of antenna are 115% (from 3 GHz to 11.1 GHz) and 119% (from 2.9 GHz to 11.5 GHz), respectively. The difference between measured and simulated impedance bandwidth are originating from different substrate specifications and fabricated problems.

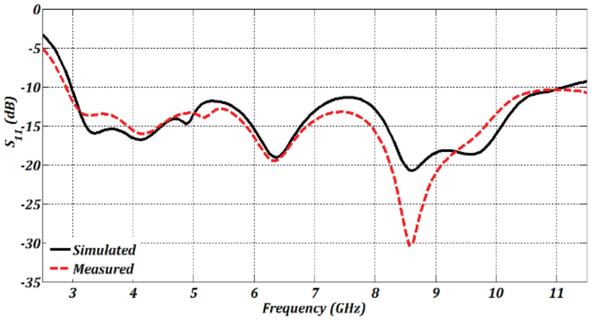

Fig. 7. Measured and simulated S_{11}.

Figure 8 indicated the close correspondence between the measured and simulated curves of gain and AR for the proposed antenna with optimized values presented in Fig. 1. As plotted in Fig. 8, the simulated ARBW of the suggested antenna is from 5000 MHz to 7000 MHz (33.3%), and the measured ARBW of antenna is from 5050 to 7100 (33.7%). Also, the measured peak gain of antenna is 4.25 dBic at 10 GHz. The average measured gain of the antenna is about 3.5 dBic.

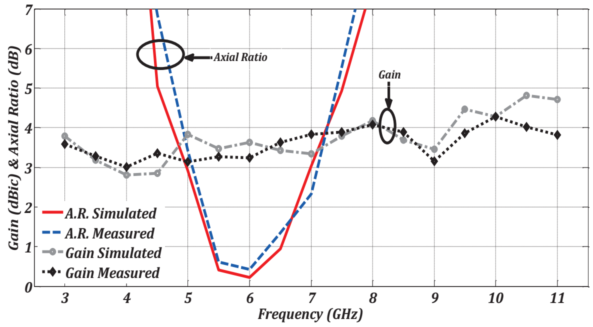

Fig. 8. Measured and simulated gain and axial ratio of the CPSSA.

The measured results of the normalized radiation patterns of the CPSS antenna are presented in Fig. 9. The radiation pattern is left-hand circular polarization (LHCP) for z>0 and RHCP for z<0, as can be deduced from surface current distributions in Fig. 6. The proposed antenna has a compact size of 25 mm × 25 mm. When compared with the previous CPSSA structures presented in Table 1, our proposed antenna shows significantly increased impedance bandwidth and axial-ratio bandwidth; i.e., the impedance and AR bandwidths are, respectively, more than three and two fold wider than the previous designs. Dielectric substrate used is FR4 with ε_r=4.4, tanδ=0.024. The impedance bandwidth is for a frequency range where the VSWR≤2; and ARBW is the 3-dB axial-ratio bandwidth.

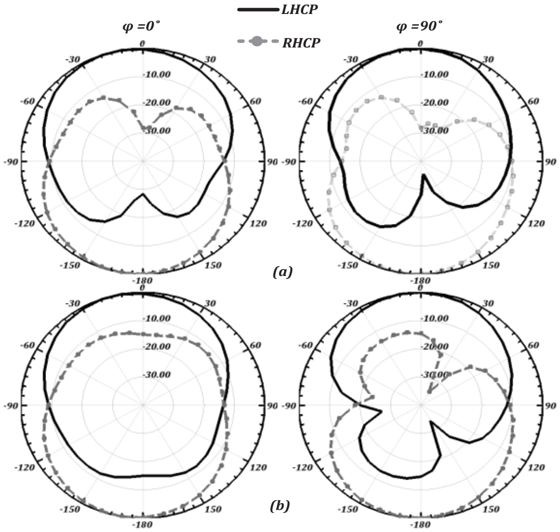

Fig. 9. Measured normalized radiation patterns of the CPSS proposed antenna at: (a) 5.5 GHz, and (b) 6 GHz.

Table 1: Comparison of the proposed CPSS antenna size and measured characteristics with other references

Ref.	Size (mm^3)	BW (GHz)	ARBW (freq. range) (GHz)	Peak Gain (dBic)
[3]	70×70×1.60	0.85 (1.75-2.6)	0.4 (1.7-2.1)	3.7
[4]	70×70×1.60	0.20 (1.5-1.7)	0.3 (1.5-1.8)	3.5
[5]	70×70×1.60	0.80 (1.6-2.4)	0.2 (1.8-2.0)	3.5
[14]	25×25×0.80	1.90 (4.6-6.5)	0.8 (4.9-5.7)	3.6
[15]	25×25×0.8	7.8 (3.1-10.9)	2 (4.5-6.5)	3.2
This work	25×25×0.80	8.6 (2.9-11.5)	2 (5-7)	4.25

The suggested antenna with optimal structure, as shown in Fig. 10, was fabricated and tested in the Antenna Measurement Laboratory at Iran Telecommunication Research Center (ITRC).

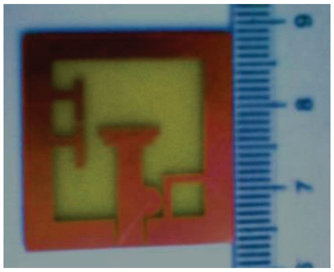

Fig. 10. Photograph of fabricated Antenna.

IV. CONCLUSION

This paper presents circularly polarized square slot antenna (CPSSA) fed by coplanar waveguide (CPW) with a crescent shaped patch. All of the important parameters that are determinant in antenna characteristics were depicted one by one while keeping the others fixed. The attributes of the proposed CPSSA include a relatively simple structure, low fabrication cost, and UWB operation across 3-11.1 GHz. The measured results show the impedance bandwidth is 115% for VSWR<2, and axial-ratio < 3 dB is 33.3%. An antenna gain of around 3.5 dBic has been obtained.

REFERENCES

[1] J. Pourahmadazar and S. Mohammadi, "Compact circularly-polarised slot antenna for UWB applications," *Electron. Lett.*, vol. 45, no. 15, pp. 837-838, August 12, 2011.

[2] J. Pourahmadazar, C. Ghobadi, J. Nourinia, N. Felegari, and H. Shirzad, "Broadband CPW-fed circularly polarized square slot antenna with inverted-L strips for UWB applications," *IEEE AWPL*, vol. 10, April 2011.

[3] J. Y. Sze, K. L. Wong, and C. C. Huang, "Coplanar waveguide-fed square slot antenna for broadband circularly polarised radiation," *IEEE Trans. Antennas Propag.*, vol. 51, pp. 2141-2144, August 2003.

[4] J. Y. Sze and Y. H. Ou, "Compact CPW-fed square aperture CP antenna for GPS and INMARSAT applications," *Microw. Opt. Technol. Lett.*, vol. 49, no. 2, pp. 427-430, February 2007.

[5] C. C. Chou, K. H. Lin, and H. L. Su, "Broadband circularly polarized cross-patch-loaded square slot antenna," *Electron. Lett.*, vol. 43, no. 9,pp. 485-486, April 2007.

[6] J. Y. Sze, J. C. Wang, and C. C. Chang, "Axial-ratio bandwidth enhancement of asymmetric-CPW-fed circularly-polarised square slot antenna," *Electron. Lett.*, vol. 44, no. 18, pp. 1048-1049, August 28, 2008.

[7] J. Y. Sze and C. C. Chang, "Circularly polarized square slot antenna with a pair of inverted-L grounded strips," *IEEE Antennas Wireless Propag. Lett.*, vol. 7, pp. 149-151, 2008.

[8] P. S. Hall, J. S. Dahele, and J. R. James, "Design principles of sequentially fed, wide bandwidth, circularly polarised microstrip antennas," *Proc. Microw. Antennas Propag.*, vol. 136, pp. 381-389, August 1989.

[9] S. Fu, S. Fang, Z. Wang, and X. Li, "Broadband circularly polarized slot antenna array fed by asymmetric CPW for L-band applications," *IEEE AWPL Lett.*, vol. 8, pp. 1014-1015, September 2009.

[10] J. Pourahmadazar and V. Rafii, "Broadband circularly polarized slot antenna array for L and S-band applications," *Electron. Lett.*, vol. 48, no. 10, pp. 542-543, 2012.

[11] J. Huang, "A technique for an array to generate circular polarization with linearly polarized elements," *IEEE Trans. Antennas Propag.*, vol. AP-34, no. 9, pp. 1113-1119, September 1986.

[12] S. Gao, Q. Yi, and A. Sambell, "Low-cost broadband circularly polarized printed antennas and array," *IEEE Antennas and Propagation Magazine*, vol. 49, no. 4, pp. 57-64, August 2007.

[13] A. Mousazadeh, M. Naser-Moghaddasi, F. Geran, S. Mohammadi, and P. Zibadoost, "Broadband CPW-fed circularly polarized square slot antenna with arc-shaped and inverted-L grounded strips," *Applied Computational Electromagnetics Society (ACES) Journal*, vol. 28, no. 4, pp. 314-320, April 2013.

[14] V. Rafii, J. Nourinia, C. Ghobadi, J. Pourahmadazar, and B. S. Virdee, "Broadband circularly polarized slot antenna array using sequentially rotated technique for C-band applications," *IEEE Antennas and Wireless Propagation Letters*, vol. 12, pp. 128,131, 2013.

[15] S. Karamzadeh, V. Rafii, M. Kartal, O. N. Ucan, and B. S. Virdee, "Circularly polarised array antenna with cascade feed network for broadband application in C-band," *Electronics Letters*, vol. 50, no. 17, pp. 1184,1186, August 14, 2014.

Small Low Power Rectenna for Wireless Local Area Network (WLAN) Applications

Sajjad Jahanbakhsh, Mohammad Ojaroudi, and Sekhavat Kazemi

Department of Electrical Engineering, Germi Branch
Islamic Azad University, Germi, Iran
sa_jahanbakhsh@yahoo.com, m.ojaroudi@iaugermi.ac.ir, kazemi.sekhavat@yahoo.com

Abstract **─** In this paper, a novel design of small low power rectenna operating on WLAN band with high harmonic rejection is presented. By using rotated E-shaped strip in the radiating patch, a new resonance at lower frequency (2.4 GHz) can be achieved. Also, by cutting a rectangular slot with protruded interdigital strip inside the slot in the feed line, a frequency band-stop performance can be achieved. The proposed structure has a major advantage in high harmonic rejection. The rectenna with integrated monopole antenna can eliminate the need for a Low Pass Filter (LPF) placed between the antenna and the diode as well as produce higher output power, with maximum conversion efficiency of 74% using a 1 KΩ load resistor at a power density of 0.3 mW/cm².

Index Terms **─** Wirless Power Transmiton System, Rectifier-Antenna (Rectenna), Protruded Interdigital Strip.

I. INTRODUCTION

The evolution of the wireless power transmission system has required simple configuration, light and easy integration with Monolithic Microwave Integrated Circuits (MMICs) and narrowband antennas for the special system application [1]. Recently, considerable research efforts have been directed toward low-profile, low-power, energy efficient, and self-sustainable sensor networks aiming to harvest ambient energy from vibrations, solar energy, as well as microwave energy from existing employed communication networks [2]-[4]. The initial development of rectenna focuses on its efficiency for great power reception and conversion. But in the last few years, excluding high power applications, wireless power transfer has been often used in microwave radiation with relatively low power densities [5,6]. This approach offers the possibility to use the rectenna as an energy module in a WSN. Indeed, the rectenna efficiency at low power level is an important feature (0 dBm, and 10 dBm), because it would allow one to power a node or a tag located far away from the RF transmitting source. For this purpose, we must take into account several considerations, such as the size, and good conversion efficiency.

During the last years, there are various antenna designs, which enable antennas with low profile, lightweight, flush mounted, and WLAN devices. These antennas include the Planar Inverted-F Antennas (PIFAs) [7], printed dipole antenna [8], the chip antennas [9], and the planar monopole antennas [10]. However, up to now, a printed antenna that has T-shaped notch configuration has not been reported. Rectifying antenna (rectenna), which can convert RF energy to DC power, plays an important role in free space Wireless Power Transmission (WPT). Over the last century, the development of rectenna for Space Solar Power Transmission (SSPT) [11] as well as WPT [12] had great achievement with specific functions, and the applications; e.g., actuator [13] or wireless sensors [14]. The typical rectenna in the prior literatures [15] basically consists of four elements: antenna, Low Pass Filter (LPF), diodes, and RC filter. The initial development of rectenna focuses on its directivity and efficiency for great power reception and conversion; hence, large array was usually adopted for microwave power reception.

In this letter, we propose a novel a microstrip rectenna with harmonic rejection property. By

Submitted On: June 6, 2013
Accepted On: July 25, 2014

using rotated E-shaped strip in the radiating patch, a new resonance at lower frequencies (2.4 GHz) can be achieved. Also, by cutting a rectangular slot with protruded interdigital strip inside the slot in the feed line, a frequency band-stop performance can be achieved. In the proposed rectenna structure, the design of the antenna is first presented followed by the rectifier circuit optimization and measurements. Finally, the complete rectenna performance is evaluated. This structure has a major advantage in providing tighter capacitive coupling to the line in comparison to known radiating patch [11]. In the proposed configuration, a pair of gap distances are playing important role in the radiating characteristics of this antenna, because it can adjust the electromagnetic coupling effects between the interdigital radiating patch and the microstrip transmission line.

II. RECTENNA DESIGN AND CONFIGURATION

The presented miniature packaged rectenna with the integrated band-reject filter is shown in Fig. 1, which is printed on an FR4 substrate of thickness 0.8 mm, permittivity 4.4, and loss tangent 0.018. The proposed rectenna structure consists of a microstrip monopole antenna for radiating element, an integrated band-reject filter, and a rectifier with DC filter and matching circuit for active part. The filter is used to reduce the out of band harmonics generated by the rectifying Schottky diode. An HSMS-2862 microwave Si Schottky detector diode pair was used to design the rectenna. The width of the 50-Ω microstrip line is fixed at 1.5 mm. The matching circuit to the left and right of the device controls the degree of reflection. On the other side of the substrate, a conducting ground plane is placed. In addition, to satisfy the efficiency requirement, the microstrip strips are fixed to a suitable electrical length, taking the calculated phases of the rectifier and passive antenna into consideration [7]. The proposed antenna is connected to a 50-Ω SMA connector for signal transmission.

In rectenna design, the antenna and rectifier circuits are typically designed separately. The antenna is designed using Electromagnetic (EM) simulation, and its parameters are then included in a nonlinear circuit simulation tool such as a Harmonic Balance (HB) simulator used to design the rectifier [5]. In this work, the complete antenna Thevenin equivalent circuit in the receiving mode is computed including the open-circuit voltage and incorporated in the harmonic balance analysis to optimize the rectenna parameters [7]. The equivalent circuit parameters can be efficiently calculated from the antenna analysis in the transmit mode using commercial EM simulators. This allows one to directly include the input power density and incoming wave direction in addition to the antenna impedance matrix in the rectenna design. The method is demonstrated by designing a dual-polarized aperture-coupled patch rectenna that has a compact size due to the use of a cross slot at the patch surface [8]. Preliminary details of the proposed rectenna design without utilizing the complete Thevenin equivalent circuit of the antenna are given in [9]. The aperture-coupled feeding structure makes the design suitable for implementation on flexible or textile-based substrates. Additionally, the method can be easily extended to rectenna array configurations.

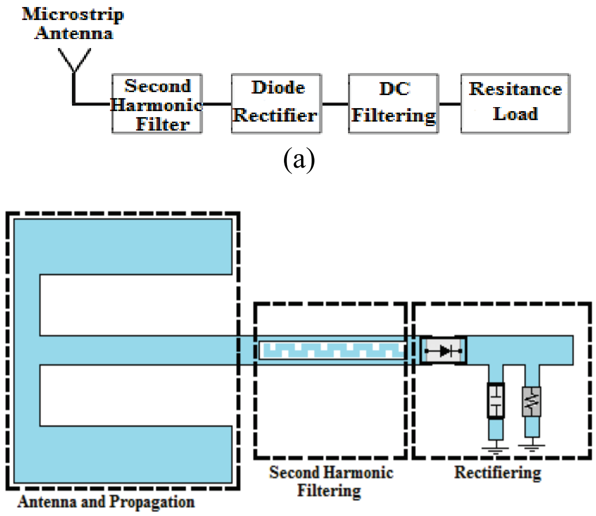

(a)

(b)

Fig. 1. Schematic of proposed rectenna with filter: (a) simplified block diagram, and (b) realized microstrip structure.

A. Antenna and defected microstrip line design

The presented small monopole antenna fed by a microstrip line is shown in Fig. 2, which is printed on an FR4 substrate of thickness 0.8 mm, permittivity 4.4, and loss tangent 0.018. The proposed monopole antenna structure consists of a rotated E-shaped radiating patch, a 50 Ω microstrip feed line with a rectangular slot with an interdigital strip protruded inside the slot, and a ground plane. The proposed antenna is connected to a 50- Ω SMA connector for signal transmission.

Regarding Defected Microstrip Structures (DMS), the creating slots in the microstrip feed-line provide an additional current path. Moreover, this structure changes the inductance and capacitance of the input impedance, which in turn leads to change the bandwidth. The DMS applied to a microstrip line causes a filtering characteristic of the structure transmission with a filter frequency controllable by changing the shape and size of the slot [3]. In this structure, the protruded interdigital strip perturbs the resonant response and also acts as a half-wave resonant structure. At the notch frequency, the current flows are more dominant around the protruded interdigital strip, and they are oppositely directed between the protruded strip and the microstrip feed-line [4]. As a result, the desired high attenuation near the notch frequency can be produced.

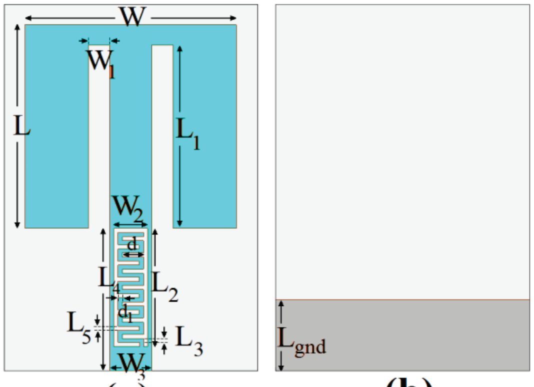

(a) (b)

Fig. 2. Geometry of proposed microstrip-fed monopole antenna: (a) top view, and (b) bottom view.

The proposed DMS with their equivalent circuit models are shown in Figs 3 (a) and (b), respectively, which is printed on a FR4 substrate of thickness 0.8 mm. This defected structure on the feed-line will perturb the incident and return current and induce a voltage difference on the ground plane and microstrip feed-line. These two effects can be modeled as a series LC circuit, such as band-stop filter response due to its frequency response [9]. Figure 4 shows the effects of the rectangular slot with an interdigital strip protruded inside the rectangular slot, on the return loss in comparison to the same antenna without it. It can be observed in Fig. 4, that by using a rectangular slot with an interdigital strip protruded inside the slot with variable dimensions in the microstrip feed-line, a band-stop performance can be created.

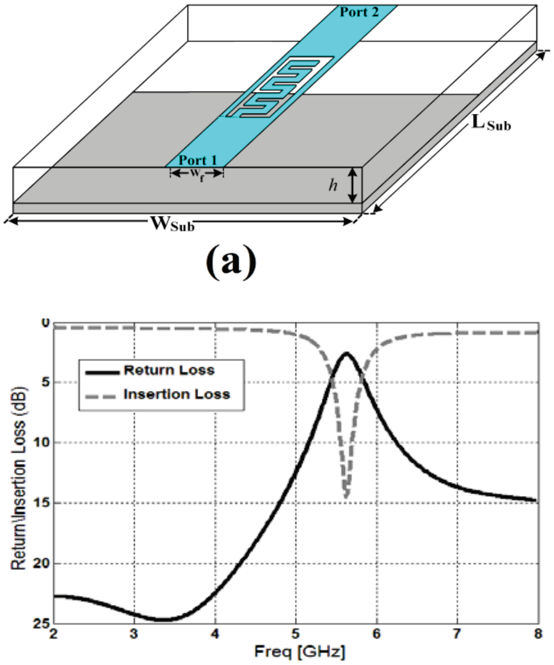

(a)

(b)

Fig. 3. (a) Geometry of the proposed Defected Microstrip Structure (DMS), and (b) simulated return/insertion loss characteristics for the proposed defected microstrip structure.

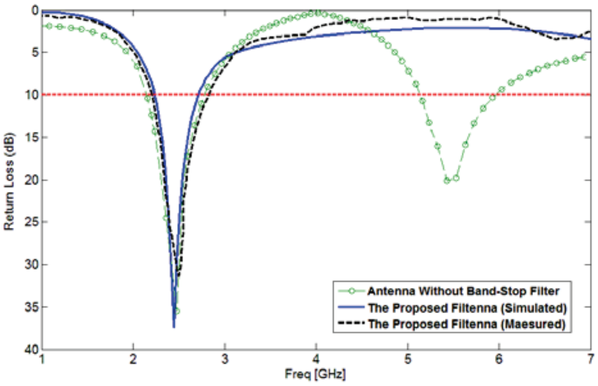

Fig. 4. Return loss comparisons for the ordinary rotated E-shaped antenna and the proposed antenna.

In order to understand the phenomenon behind this new resonance and out of band harmonic generation, the simulated current distributions on the top layer for the proposed antenna are shown in Fig. 5. As shown in Fig. 5 (a), at the first resonance frequency (2.4 GHz) the current mainly concentrates on the rotated E-shaped strip in the radiating patch, and also as shown in Fig. 5 (b), at the notch frequency (5.5 GHz) the current flows are more dominant around of the protruded interdigital strip. As a result, the desired high attenuation near the notch frequency can be produced [3]-[5].

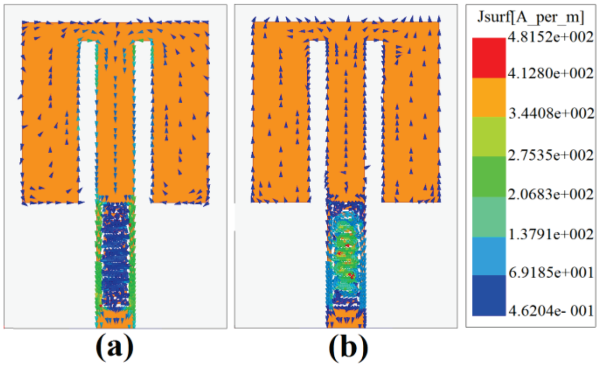

Fig. 5. Simulated surface current distributions on the radiating patch: (a) at the first resonance frequency (2.4 GHz), and (b) the second resonance frequency (5.5 GHz).

B. Rectifier design

In this study, the Schottky diode is used in the rectification of RF energy for the rectenna. The Schottky diode is used mainly because of its low turn on voltage and low junction capacitance characteristics, which enables it to work at the high frequencies required. The circuit diagram of rectifier is given in Fig. 6, while component values are summarized in Table 1. Dimensions of the resonators and the matching network were optimized using Agilent's Advanced Design System (ADS) in conjunction with the Electromagnetic (EMDS) Simulation tool to get the required oscillation frequencies for dual-band operation. At a maximum distance of 2 m, output dc voltage of over 2 V at the lower frequency band and over 1 V at the higher frequency band can be achieved [9]. Figure 7 shows return loss in dB versus frequency for the deigned rectifier.

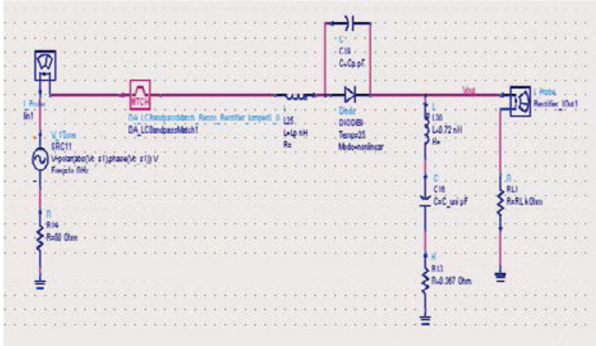

Fig. 6. Circuit diagram of the proposed rectifier circuit.

Table 1: Rectifier circuit dimensions and component values

Param.	R_L	L_2	L_1	C_{uni}
Value	1.1 KΩ	3.93 nH	2.01 nH	3.01 pF

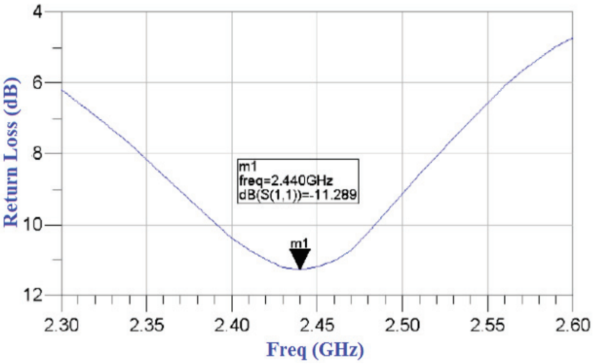

Fig. 7. Return loss versus the frequency.

III. RECTENNA PERFORMANCE

The receiving antenna and rectifying are connected by SMA connectors as shown in Fig. 8. It contains a linearly polarized monopole antenna designed at 2.4 GHz by using HFSS software [16]. The rectenna contains one HSMS2860 commercial Schottky diodes in a SOT23 package. The zero bias junction capacitance Cj0 is 0.18 pF and the series resistance Rs is 5 V. The experiments have been carried out in anechoic chamber. The transmitting antenna is a standard linear polarized horn with gain G_t of 12 dB. The rectenna is located at the distance *r* of 50 cm, which is the far region of the horn.

In general, the overall efficiency of a rectenna is defined as a ratio of DC power to incident RF power as below:

$$\eta_0 = \frac{V^2 / R_{Load}}{P_A}. \qquad (1)$$

The measured overall efficiency is shown in Fig. 8. In the power density range (0-0.25 mW/cm^2), the measured rectenna efficiency is above 72% from 0.2 mW/cm^2 power density over a 1 KΩ load resistance. The measured results show that the efficiency increases when the power density increases. In applications, the antenna and rectifying circuit can be integrated directly on one substrate by omitting SMA connectors. Without the loss of SMAs, the efficiency would be higher.

The output DC voltage has been measured against power density from the Friss transmission equation:

$$P_r = \left(\frac{\lambda}{4\pi r}\right)^2 P_t G_t G_r, \qquad (2)$$

where P_t is the transmitting power; G_r is the receiving antenna gain, λ is the free space wavelength at 2.42 GHz. The rectenna is illuminated by a linearly polarized incident plane wave of 20 V/m (0.10 mW/cm^2) at its broadside. On the transmitter side, we have used a 30 dB gain power amplifier at 2.4 GHz connected to a signal generator. The output DC voltage across the resistor load has been measured by a voltmeter.

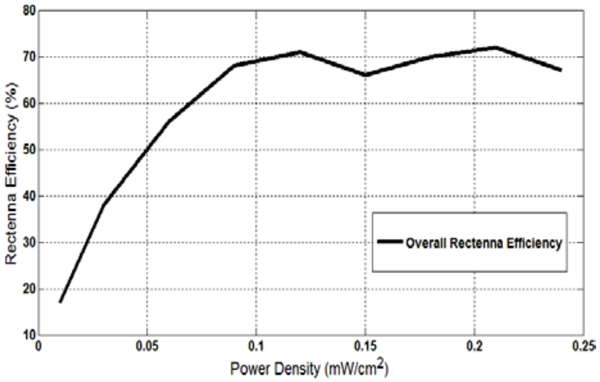

Fig. 8. Measured rectenna efficiency against power density.

The measured output DC voltages are shown in Fig. 9. In the power density range (0-0.3 mW/cm^2), the measured output DC voltage is 2.9 V over a 1 KΩ optimized load resistance. The measured results show that the output voltage increases when the power density increases.

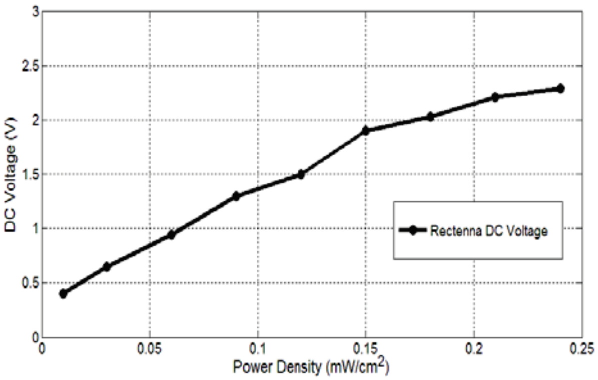

Fig. 9. Measured DC voltages against power density.

IV. CONCLUSION

As presented above, a novel design of rectenna with a series diode circuit topology is an interesting subject for WLAN applications. By using rotated E-shaped strip in the radiating patch, a new resonance at lower frequencies (2.4 GHz) can be achieved. Also, a rectangular slot with protruded interdigital strip inside the slot in the feed line is used to reject the second harmonic. No input low pass filter is needed; thus, reducing the insertion losses and the dimensions of the circuit. The oscillator design based on the AIA concept has been shown to provide an efficient and successful method for designing high efficiency and compact systems. The rectifying circuit has been optimized at 2.4 GHz for an input power of 10 dBm. The rectenna exhibits a measured efficiency of 72% at 0.24 mW/cm^2 power densities and an output DC voltage of 2.39 V.

REFERENCES

[1] A. R. Rofougaran, M. Rofougaran, and A. Behzad, “Radios for next-generation wireless networks,” *IEEE Microwave Magazine*, 6, pp. 38-43, March 2005.

[2] G. Orecchini, L. Yang, A. Rida, F. Alimenti, M. M. Tentzeris, and L. Roselli, “Green technologies and RFID: present and future,” *Applied Computational Electromagnetics Society (ACES) Journal*, vol. 25, no. 3, pp. 230-238, March 2010.

[3] L. Ukkonen, T. Björninen, L. Sydänheimo, A. Elsherbeni, and F. Yang, “Importance of computational electromagnetic modeling in the development of RFID tags for paper reel identification,” *Applied Computational Electromagnetics Society (ACES) Journal*, vol. 25, no. 6, pp. 505-516, June 2010.

[4] Y. Zhao, L. Zhong, J. S. Hong, and G. M. Zhang, "A monopole antenna with SIR ground for harmonic suppression and bandwidth enhancement," *Applied Computational Electromagnetics Society (ACES) Journal*, vol. 26, no. 8, pp. 705-708, August 2011.

[5] F. Zhang, X. Liu, F. Y. Meng, et al., "Design of a compact planar rectenna for wireless power transfer in the ISM band," *International Journal of Antennas and Propagation*, vol. 2014, article ID 298127, 9 pages, 2014. doi:10.1155/2014/298127.

[6] A. Faraghi, M. Ojaroudi, and N. Ghadimi, "Compact microstrip low-pass filter with sharp selection characteristics using triple novel defected structures for UWB applications," *Microwave and Optical Technology Letters*, 56 (4), pp. 1007-1010, 2014.

[7] G. Beigmohammadi, C. Ghobadi, J. Nourinia, and M. Ojaroudi, "Small square slot antenna with circular polarisation characteristics for WLAN/WiMAX applications," *Electron Lett*, 46, 2010.

[8] J. D. Kraus and R. J. Marthefka, "Antennas," *McGraw-Hill*, New York, 2003.

[9] J. Mazloum, A. Jalali, and M. Ojaroudi, "Miniaturized reconfigurable band-pass filter with electronically controllable for WiMAX/WLAN applications," *Microwave and Optical Technology Letters*, 56 (2), pp. 509-512, 2014.

[10] H. Takhedmit, L. Cirio, O. Picon, C. Vollaire, B. Allard, and F. Cost, "Design and characterization of an efficient dual patch rectenna for microwave energy recycling in the ISM band," *Progress In Electromagnetics Research C*, vol. 43, 93-108, 2013.

[11] P. E. Glaser, "An overview of the solar power satellite option," *IEEE Trans. Microw. Theory Tech.*, vol. 40, no. 6, pp. 1230-1238, June 1992.

[12] W. C. Brown, "The history of power transmission by radio waves," *IEEE Trans. Microw. Theory Tech.*, vol. 32, no. 9, pp. 1230-1242, September 1984.

[13] L. W. Epp, A. R. Khan, H. K. Smith, and R. P. Smith, "A compact dual polarized 8.51-GHz rectenna for high-voltage (50 V) actuator applications," *IEEE Trans. Microw. Theory Tech.*, 48, (1), pp. 111-120, 2000.

[14] K. M. Farinholt, G. Park, and C. R. Farrar, "RF energy transmission for a low-power wireless impedance sensor node," *IEEE Sensors J.*, 9, (7), pp. 793-800, 2009.

[15] H. Takhedmit, L. Cirio, B. Merabet, B. Allard, F. Costa, C. Vollaire, and O. Picon, "Efficient 2.45 GHz rectenna design including harmonic rejecting rectifier device," *Electronics Letters*, vol. 46, no. 12, 426, June 10, 2010.

[16] "Ansoft high frequency structure simulation (HFSS)," ver. 13, *Ansoft Corporation*, 2010.

A Compact Frequency Reconfigurable Split Ring Monopole Antenna for WLAN/WAVE Applications

V. Rajeshkumar and S. Raghavan

Department of Electronics and Communication Engineering
National Institute of Technology (NIT), Tiruchirappalli, Tamilnadu, India
vrajeshme@gmail.com, raghavan@nitt.edu

Abstract **─** A novel frequency reconfigurable dual band monopole antenna based on the triangular split ring element is proposed for wireless communications. The antenna with an overall compact size of 25×25×1.6 mm^3 is designed for the operating frequencies of wireless local area network (WLAN) 2.4/5.0 GHz standard and wireless access for vehicular environments (WAVE) 5.90 GHz standard. The parametric study is carried out for tuning the upper resonant frequency. The reconfigurability between the WLAN and WAVE frequency bands is achieved by using a pair of PIN diode. The design considerations for the proposed antenna are described and the experimental results are validated. The antenna exhibits almost uniform radiation characteristics and good gain at each frequency band with the -10 dB impedance bandwidth of 44.1%, 5.8% and 10.1% at 2.45/5.30/5.90 GHz WLAN and WAVE bands respectively.

Index Terms **─** Dual band, PIN diode, reconfigurable, split ring resonator, WAVE and WLAN.

I. INTRODUCTION

Rapid growth in the modern wireless communication systems leads to demand for multiband, low cost and compact antennas. In wireless communications, wireless local area network (WLAN) and wireless access for vehicular environment (WAVE) technologies are mainly used for its mobility and high-speed data accessing. Also, demand for compact and multiband antennas in modern wireless handheld devices are increased for passengers in vehicles to utilize the current wireless services such as entertainment applications, web browsing, emailing and data exchanging. As well as, the main applications of the WAVE technology includes intelligent transportation systems (ITS), high-speed communications and internet access, safety and security enhancements. The standard IEEE 802.11b/g covers the lower frequency band ranging from 2.40 GHz to 2.4835 GHz and the standard IEEE 802.11a covers the upper frequency band ranging from 5.15 GHz to 5.35 GHz and 5.725 GHz to 5.825 GHz for WLAN applications [1, 2]. The standard IEEE 802.11p covers the frequency band 5.85 to 5.925 GHz for WAVE applications [1].

The challenges in the design of dual band antennas are compact size, mechanically robust, wide bandwidth with good impedance matching, omnidirectional radiation patterns, high gain, low profile and low manufacturing cost [1, 3]. Due to the limited space availability in modern compact wireless devices, the design of multiband antennas requires much attention in terms of size along with aforementioned characteristics. Recently, different dual band antennas have been proposed for WLAN applications [1-5]. Although these antennas provide significant radiation characteristics, they lack on complex structure, bandwidth as well as large radiating area. In addition, the antennas reported in [6-9] are few notable multiband antennas operating in our frequency range of interest (WLAN). Although they provide wide band coverage and good radiation characteristics, they suffer from very poor compactness and tunability.

In recent years, split ring resonator (SRR) based monopole antennas are receiving a lot of interest towards the wireless applications, since it offers miniaturization due to its sub-wavelength

Submitted On: June 19, 2014
Accepted On: December 11, 2014

resonant nature [2, 7-10]. Reconfigurable antennas play a significant role in telecommunication systems because they offer compact size by avoiding multiple antenna requirements to utilize more than one wireless standard in a single system, similar radiation characteristics, stable gain at each designed frequency band and low cost [9-11]. In order to allow the operating frequencies to be reconfigurable, switching components specifically varactor diodes [10] and PIN diodes [11], are often used in reconfigurable antenna applications compared to MEMS switches. Since the PIN diode has several advantages like good performance and low cost compared to other switching elements [11], we opted for PIN diode as a switch element in the proposed reconfigurable antenna design.

In this paper, a reconfigurable novel SRR based monopole antenna for dual band WLAN/WAVE applications is presented. The proposed SRR is a single ring structure; hence it is simple to design compared to the conventional double ring SRRs. This triangular SRR is a kind of metamaterial cell that has the advantage of versatility in controlling the resonant characteristics by altering its length. Thus, it alters the inductance and capacitance values of the resonant structure. It paved the way for frequency tuning. Hence, the frequency reconfigurability between the WLAN and WAVE standard is achieved by altering the electrical length of the proposed SRR by using a pair of PIN diode. Details of the antenna design are described in Section II. The parametric study and the proposed method of reconfigurability are explained in Section III along with its radiation characteristics. The concluding remarks are highlighted in Section IV.

II. ANTENNA DESIGN

The geometry of the proposed split ring monopole antenna fed by a microstrip transmission line is shown in Fig. 1. The complete antenna is simulated using the EM simulator, Ansoft High Frequency Structure Simulator (HFSS) V.14.0, based on Finite Element Modeling (FEM) [12]. Also, it is fabricated on an FR4 substrate with dielectric constant $\varepsilon_r = 4.4$, thickness h = 1.6 mm and loss tangent $\tan\delta = 0.018$. The proposed antenna structure consists of a triangular SRR as the radiating element, a feed line, and a partial ground plane. The key antenna parameters of the antenna are optimized using optimetrics provided in the HFSS.

A pair of shunt arms of length L_3 in the triangular SRR plays an important role than the other parameters in the performance of the upper resonant frequency. Because it can create additional surface current paths in the antenna and therefore additional resonance is obtained. The overall length $2(L_2+T+L_3)$ contributes to split ring resonator's inductance and the split gap (s) contributes the capacitance, which determines the resonant frequency of the SRR. In addition, the presence of shunt arms completes the triangular split ring resonator; hence, the negative permeability can be created. Thus, the dimension of the shunt arm is varied for tuning of the upper resonant frequency. The feed length (f_L), width (W_1) and ground plane length (L_1) are optimized to 9 mm, 2.9 mm and 9 mm respectively, for good impedance matching. The various optimized design parameters of the antenna are given in Table 1.

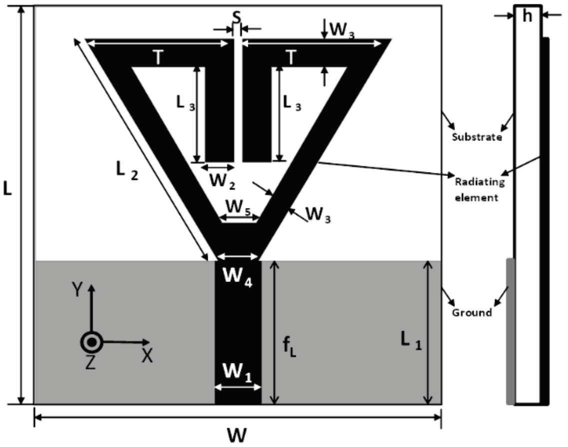

Fig. 1. Geometry of the proposed split ring monopole antenna.

Table 1: Design parameters of the optimized antenna

Parameter	Value (mm)	Parameter	Value (mm)
L	25	W_5	2.0
W	25	L_1	9.0
W_1	2.9	L_2	16.25
W_2	1.8	L_3	6.0
W_3	1.8	S	0.5
W_4	2.5	T	9.25

III. RESULTS AND DISCUSSIONS

In this section, the numerical and experimental results of the return loss and radiation characteristics are presented for the proposed split ring monopole antenna. The various design parameters are analyzed and based on that, the final prototype is fabricated and tested. The effect of feed width, shunt arm's length, possibility of reconfigurable antenna system and its radiation characteristics are discussed here.

A. Effect of feed width W_1 and shunt arm L_3

The split ring monopole antenna without the shunt arms (i.e., $L_3 = 0$) is designed initially. It is observed that the SRR monopole without the shunt arm resonates at 2.45 GHz and 7.0 GHz. The lower frequency band is caused by the feed length (f_L), feed width (W_1), strip (L_2) and top edge (T) of the SRR; since it contributes to the longer electrical length of the structure. The parametric study of W_1 (1.7 mm to 3.5 mm) is shown in Fig. 2. The variation in W_1 has significant effect on antenna performance. For better impedance matching in both the frequency bands, the feed width is chosen to be 2.9 mm in the proposed antenna design. Due to the absence of L_3, the SRR characteristic is less effective, and hence, poor return loss is observed in the upper resonant frequency which is shown in Fig. 3. Therefore, the parametric study is carried out by varying L_3 and keeping all other antenna parameters as constants. While the length L_3 is increased from 1 mm to 6 mm, it is observed that the upper resonant frequency starts decreasing from 7.0 GHz to 5.30 GHz. Since the split ring's electrical length increases, it is attributed to high inductance value of the SRR; hence, the resonant frequency decreases. The proposed antenna without the shunt arm is also fabricated and the corresponding simulated and measured results are shown in Fig. 3. The measured impedance bandwidth of about 1040 MHz and 620 MHz is achieved at 2.45 GHz and 7 GHz bands, respectively. This can be used for downlink 7 GHz X-band satellite applications. However, since our aim is to design the antenna for WLAN and WAVE application, the shunt arm's length is parameterized accordingly for WLAN and WAVE applications. The numerical resonant characteristics of the upper frequency for the proposed split ring monopole antenna for various lengths L_3 are given in Table 2.

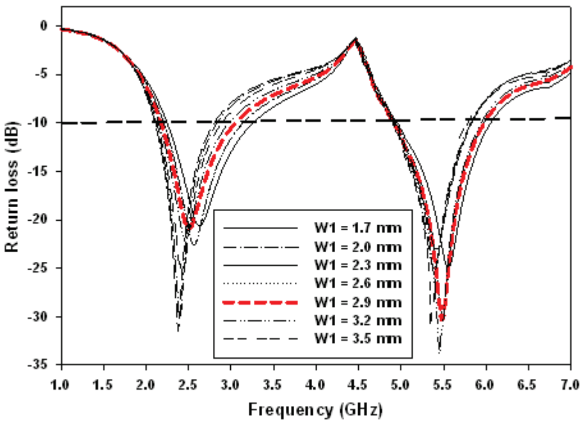

Fig. 2. Simulated return loss characteristics of the proposed antenna for various feed width.

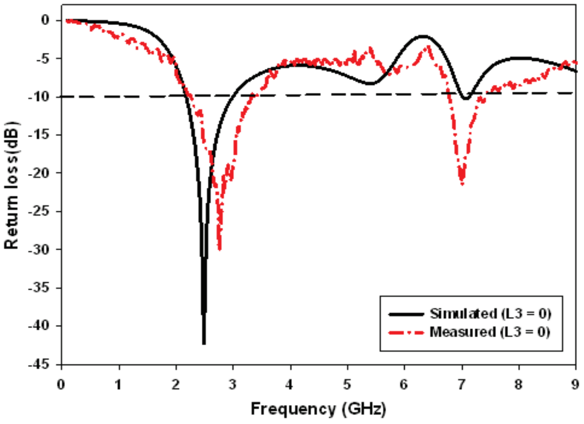

Fig. 3. Simulated and measured return loss characteristics of the proposed antenna when $L_3 = 0$.

Table 2: Effect of length L_3

L_3 (in mm)	f_r (in GHz)
0	7.0
1	6.77
2	6.67
3	6.13
4	5.90
5	5.80
6	5.30

B. Dual band antenna for WAVE/WLAN application

From the above parametric study it is noted that for the shunt arm length 4 mm and 6 mm, the proposed antenna has an upper resonant frequency of 5.90 GHz and 5.30 GHz, respectively. These are the operating frequencies of WAVE and WLAN bands correspondingly. The incremental length L_3 and its effect on the upper resonant frequency have paved the way for reconfigurability. It is decided to access WAVE and WLAN bands alternatively by using a switching element.

As shown in Fig. 4, the spaces left in the antenna configuration (#1) is used for the switches. Where 0.5 mm space is left for the switch and 1.5 mm length stub is placed successively. When the switches are in OFF state, the length L_3 is 4 mm, which contributes to the 5.90 GHz WAVE band. Similarly, when the switches are in ON state, the 1.5 mm stub gets added to L_3, which increases its electrical length to 6 mm contributing to the 5.30 GHz WLAN band. In the simulation, the presence and absence of a metal strip represent ON state and OFF state, respectively [9].

The switching can be practically achieved by introducing a pair of PIN diodes as switch element in the spaces left in configuration #1. The PIN diodes can go from the OFF state to the ON state by controlling the applied DC bias currents. In our practical realization, the PIN diode (BAP 6503, SOD323V) is used as a switch element in the spaces provided. Initially, the switches are kept in OFF state and the corresponding measurement is carried out.

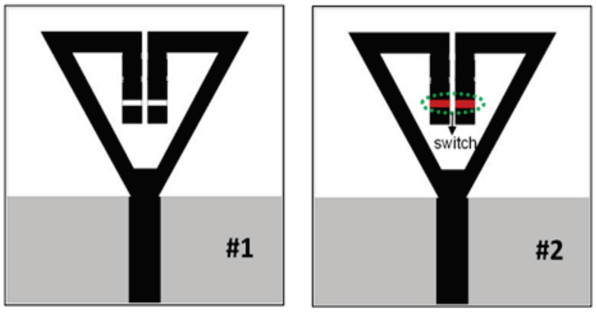

Fig. 4. Configurations of the reconfigurable split ring monopole antenna.

Figure 5 illustrates the simulated and measured return loss characteristics of the configuration #1 when the switches are in OFF state. In the dual band system, the measured first resonant frequency occurs at 2.45 GHz with the wide impedance bandwidth of 1080 MHz (2.01–3.09 GHz), and the second resonant frequency occurs at 5.90 GHz with an impedance bandwidth of about 600 MHz (5.76–6.36 GHz). It covers the lower band of WLAN as well as the WAVE frequency band (5.85–5.925 GHz). This makes the proposed antenna highly suitable for IEEE 802.11P WAVE standard.

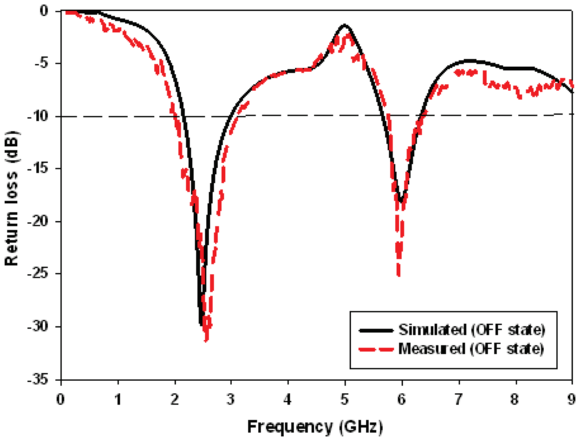

Fig. 5. Simulated and measured return loss characteristics when switches are in OFF state.

Then, by enabling the switches to ON state, the electrical length of shunt arms L_3 increases and reaches 6 mm, where the conductor stub is connected to the triangular split ring monopole antenna as shown in the configuration #2. The corresponding return loss characteristics are shown in Fig. 6, which shows the resonant frequencies at 2.45 GHz and 5.30 GHz bands, which are the desired WLAN bands. Figure 6 illustrates that similar results are obtained for both the proposed triangular SRR monopole antenna (without switches) and the reconfigurable antenna (#2). The measured impedance bandwidth of about 700 MHz (2.17–2.87 GHz) and 840 MHz (5.05–5.89 GHz) is achieved with good impedance matching at 2.45 GHz and 5.30 GHz bands respectively, which meet the specifications (2.4–2.4835 GHz & 5.15–5.825 GHz) of WLAN standard. The fabricated prototype of the proposed antenna is shown in Fig. 7 (a). Figure 7 (b) illustrates the antenna configuration (#2) with the PIN diodes.

The Figs. 8 (a) and (b) shows the simulated surface current distributions in 2.45 GHz and 5.30 GHz for the proposed antenna. While focusing the current distribution at 2.45 GHz, the maximum radiation can be observed in the feed line, strip L_2 and top edge T. As mentioned earlier, the shunt arm L_3 contributes to the upper resonant frequency of the antenna, and hence, a maximum current is distributed around L_3 for the upper resonant frequency 5.30/5.90 GHz.

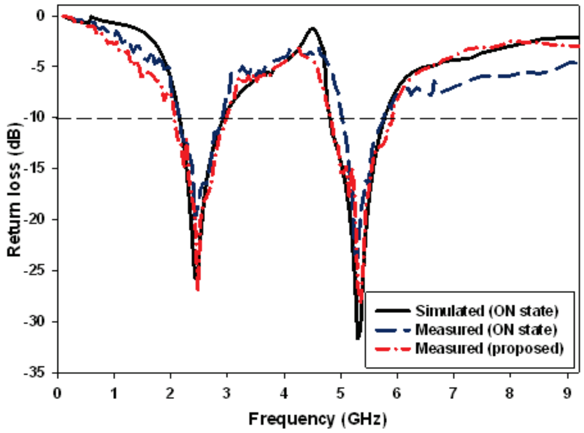

Fig. 6. Simulated and measured return loss characteristics when switches are in ON state.

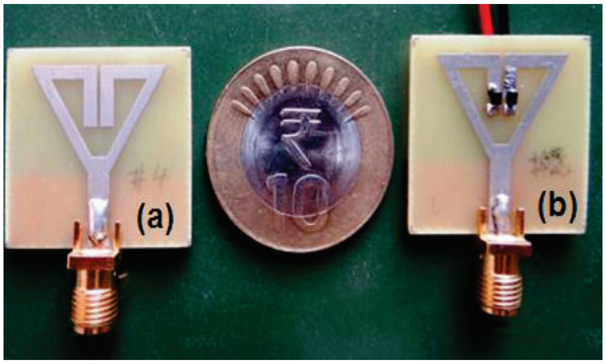

Fig. 7. Photographs of: (a) the proposed antenna, and (b) with switches.

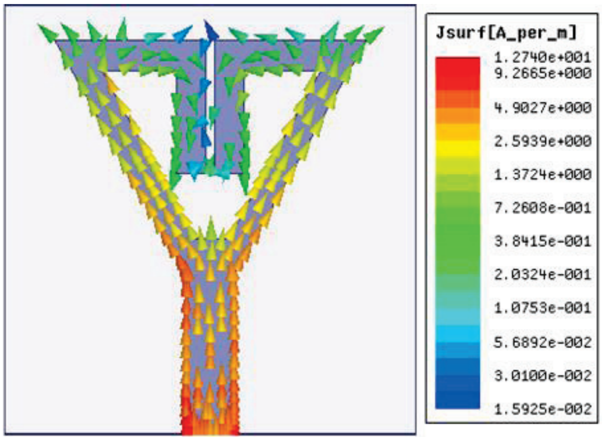

(a)

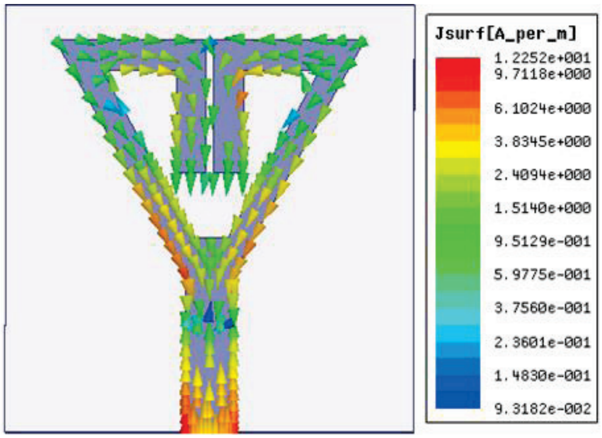

(b)

Fig. 8. The simulated surface current distributions at: (a) 2.45 GHz, and (b) 5.30 GHz.

C. Radiation patterns and gain

The radiation patterns of the proposed reconfigurable antenna have also been measured in an anechoic chamber using double ridge horn as transmitting antenna, and the proposed split ring monopole antenna as the receiving antenna. Figures 9 (a), (b) and (c) show the normalized co-polarization and cross-polarization radiation patterns in E-plane (yz–plane) and H-plane (xz–plane) at three different frequencies of 2.45 GHz, 5.30 GHz, and 5.90 GHz respectively. From these radiation patterns, it is observed that the proposed antenna displays omnidirectional radiation characteristics in the H-plane and dipole-like radiation in E-plane at all the desired frequencies. A low cross-polarization level of less than -20 dB is observed at all frequencies of interest.

The measured gain plot of the proposed reconfigurable antenna is shown in Fig. 10; maximum gain of 2.52 and 2.65 dBi is obtained at the WLAN frequencies 2.45 and 5.30 GHz respectively. Also, for the maximum gain of 2.75 dBi is observed for the 5.90 GHz WAVE frequency band. It is obvious that the antenna gain decreases drastically at the frequency where the SRR exhibits stop band characteristics due to its negative permeability characteristics. It is useful in antenna design for providing a very good out of band rejection between the operating bands. In the future, the proposed SRR can be used in filter applications and UWB communications for creating notches at the desired frequencies by using its negative permeability feature. It can be achieved by varying the inductance and capacitance values of the proposed SRR by altering its length and split gap.

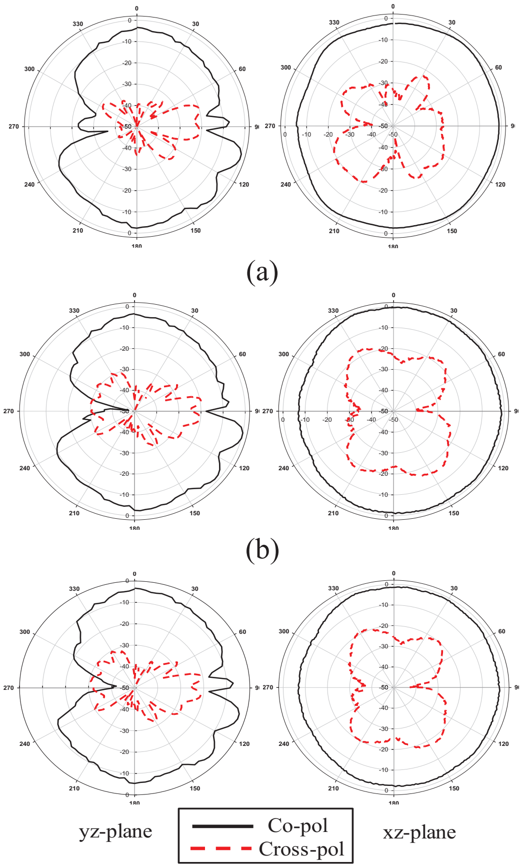

(a)

(b)

(c)

Fig. 9. Measured radiation patterns at: (a) 2.45 GHz, (b) 5.30 GHz, and (c) 5.90 GHz.

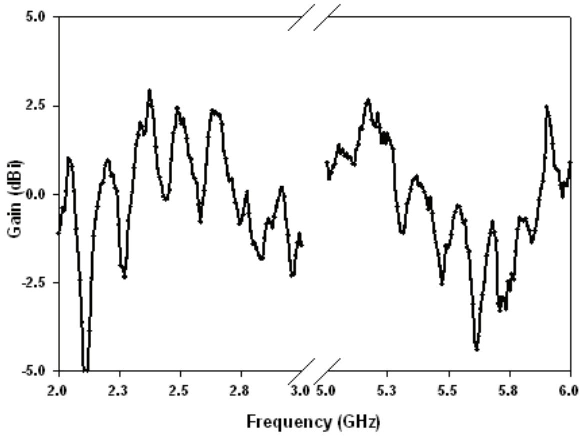

Fig. 10. Measured gain of the proposed antenna.

IV. CONCLUSION

A compact frequency reconfigurable dual band monopole antenna based on the split ring element is discussed. The operating frequencies of the proposed antenna are 2.45/5.0/5.9 GHz, which meet the specifications of WLAN/WAVE standards. A prototype with a very compact dimension, with respect to recently reported antennas, is fabricated and measured. By placing PIN diodes in the tuning stub (L_3), reconfigurability is demonstrated. The wireless devices in the fast moving vehicles can switch over from WLAN to WAVE mode, which is specifically designed for wireless access in a vehicular environment. Also, the proposed antenna finds most useful application in intelligent transportation systems. Measured results validate the reconfigurability of the proposed antenna. The experimental result shows good agreement with the simulation results. The compactness in size, consistency in gain and reconfigurable system approach makes the designed antenna suitable for practical application in the WLAN/WAVE communications.

REFERENCES

[1] W-C. Liu, C-M. Wu, and N-C. Chu, "A compact low-profile dual-band antenna for WLAN and WAVE applications," *AEU-Int. J. Electron. C.*, vol. 66, pp. 467-471, 2012.

[2] W-J. Wu, Y-Z. Yin, S-L. Zuo, Z-Y. Zhang, and W. Hu, "Dual-wideband monopole loaded with split ring for WLAN application," *Prog. Electromagn. Res. Lett.*, vol. 21, pp. 11-18, 2011.

[3] P. Wang, G. J. Wen, Y. J. Huang, and Y. H. Sun, "Compact meander T-shaped monopole antenna for dual-band WLAN applications," *Int. J. RF Microw. C. E.*, vol. 23, no. 1, pp. 67-73, 2013.

[4] J. Zhu and G. V. Eleftheriades, "Dual-band metamaterial-inspired small monopole antenna for WiFi applications," *IET Electron. Lett.*, vol. 45, no. 22, pp. 1104-1106, 2009.

[5] C-Y.Huang and E-Z. Yu, "A slot-monopole antenna for dual-band WLAN applications," *IEEE Antennas Wireless Propagat. Lett.*, vol. 10, pp. 500-502, 2011.

[6] J. Gemio, J. P. Granados, and J. S. Castany, "Dual-band antenna with fractal-based ground plane for WLAN applications," *IEEE Antennas Wireless Propagat. Lett.*, vol. 8, pp. 748-751, 2009.

[7] L-M. Si, W. Zhu, and H-J. Sun, "A compact, planar, and CPW-fed metamaterial-inspired dual-band antenna," *IEEE Antennas Wireless Propagat. Lett.*, vol. 12, pp. 305-308, 2013.

[8] S. C. Basaran and Y. E. Erdemli, "A dual-band split-ring monopole antenna for WLAN applications," *Microw. Opt. Technol. Lett.*, vol. 51, no. 11, pp. 2685-2688, 2009.

[9] R. H. Cheribi, F. Ghanem, and H. Kimouche, "Metamaterial-based frequency reconfigurable antenna," *IET Electronics Letters*, vol. 49, no. 5, pp. 315-316, 2013.

[10] S. Zhu, D. G. Holtby, K. L. Ford, A. Tennant, and R. J. Langley, "Compact low frequency varactor loaded tunable SRR antenna," *IEEE Trans. Antennas Propag.*, vol. 61, no. 4, pp. 2301-2304, 2013.

[11] H.-Y. Huang, B-Z. Wang, X. Ding, and W. Shao, "A pattern reconfigurable antenna based on TM_{10} and TM_{02} modes of rectangular patch," *Appl. Comp. Electro. Society (ACES) Journal*, vol. 28, no. 8, pp. 693-700, 2013.

[12] Ansoft High Frequency Structural Simulator (HFSS), ver. 14, Ansoft Corporation, 2014.

V. Rajeshkumar received his UG degree in Electronics and Communication Engineering from MPNMJ Engineering College, Erode, and the PG degree in Communication Systems from Sona College of Technology, Salem. He is working towards his Ph.D degree in the area of Metamaterial Antennas under the guidance of Dr. Raghavan in the department of Electronics and Communication Engineering, National Institute of Technology, Tiruchirappalli, India. His research interest includes metamaterials, fractal antennas, microwave integrated circuits, planar antennas, and computational electromagnetics.

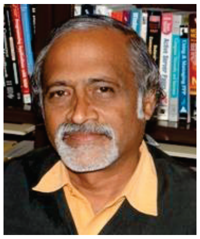

S. Raghavan has 32 years of experience in teaching and research at National Institute of Technology, Tiruchirappalli, India as a Senior Professor. He received his UG degree in ECE from College of Engineering, Guindy, and the PG degree in the specialization of Microwave Engineering from College of Engineering, Trivandrum. He completed his Doctoral programme in the field of Microwave Integrated Circuits from I.I.T. Delhi, India under the guidance of Professor Bhat and Professor Koul. His research interest includes microwave/millimeter-wave circuits and devices, microwave integrated circuits, EMI/EMC, antennas, computational electromagnetics, microwaves in biomedical applications, and metamaterials.

Design of a Novel Ultra-Wideband Semicircular Printed Antenna with Dual-Band Notched Characteristic

Mahdi Najafpur, Javad Nourinia, and Fateme Azamian Jazi**

Department of Electrical Engineering
Urmia Branch, Islamic Azad University, Urmia, Iran
mahdinajafpur@yandex.ru, J.Nourinia@urmia.ac.ir, fateme.azamian@yandex.ru

Abstract **─** A compact semicircular printed antenna with dual-band notched characteristic is proposed. A narrow rectangular slot is etched on the radiation patch to prevail notch band at 5.13-5.87 GHz for WLAN. By using two circular slots (C-shaped) defected ground structure, another notch band, at 7.59-9.03 GHz for some C-band satellite communication systems, is achieved. Due to the shape of the proposed antenna, the total dimension of this structure occupies very small space. The antenna is successfully simulated and measured. A simple 50-Ω microstrip line is used to excite the slot. The parameters and dimensions of the antenna have been investigated by using HFSS. Results demonstrate that the suggested antenna with small size of 20×20×1 mm^3 has desired bandwidth range from 2.6-13.3 GHz for VSWR≤2, except two notch bands.

Index Terms **─** Band notch, compact, microstrip antenna.

I. INTRODUCTION

High wireless communications is swiftly expanding resulting in a demand for communication systems that are credible. Ultra-wideband (UWB) system is becoming the good candidate of high speed technique for wireless communications. UWB antenna is the key device of the UWB wireless communication system [1]. The ultra-wideband (UWB) microstrip antenna has become very common and is now greatly used for various applications. The high demands on such a communications system have simulated research into many UWB antenna designs [2]. So, UWB antenna is a hot theme in recent years. There are several methods with which one can achieve a band-notched UWB antenna. The most popular approach to introduce such a band-notched function is to embed slots or slit into the radiator or its ground plane [3], [4]. A lot of slot antennas for UWB systems have been developed, such as circular slot antenna [5], square slot antenna. In the whole UWB band which is defined by FCC, there are some narrow bands which have been used for a long time, such as worldwide interoperability for microwave access (WiMAX), wireless local area networks (WLAN) and C-band, X-band [6], [7]. To decrease interference, the traditional method is to add narrow band-stop filter to filter the unrequired signal [6]. In this way the cost of process will rise, make the antenna size very large and also the efficiency and qualification of the antenna will decrease. So to solve this problem a lot of notch-band antennas are recommended. There are several ways with which one can obtain a band-notched UWB antenna. The most popular approach is to insert different kinds of slots in the patch or in the ground plane. Like U-shaped, H-shaped or C-shaped slots. The designs of meandering slot antennas in [8] and [9] use different slots to generate two resonant modes. These slot antennas mentioned are much smaller than the traditional modified monopoles, but their structures are much more complex for the practical engineering applications [10]. Ring antennas with simple structure have been presented in [11], [12], the proposed antenna has one notched band and the slots have some influence on the radiation patterns, and the notch band is difficult to adjust to form a good filter characteristic. The recommended two notch bands can be tuning by changing the dimensions of circular slots on the ground and narrow rectangular slot on the patch.

Submitted On: May 27, 2013
Accepted On: December 10, 2014

In this paper, a compact UWB antenna to exhibit notching method is designed. By embedding two different kinds of slot, dual-band notched characteristic antenna is achieved. To achieve the desired band notched characteristic, the dimensions of this antenna are optimized. It should be noted that the ultra-wideband characteristics from 2.6-13.3 GHz corresponds to 143% total bandwidth. The parameters which influence the act of the antenna are investigated in this paper.

II. ANTENNA DESIGN AND CONFIGURATION

Figure 1 shows the top view of the microstrip antenna with and without slots. The geometry of the suggested antenna is depicted in Fig. 2. It consists of a radiation patch with a semicircular-shaped patch and a partially modified ground plane with two kinds of slots to achieve a broad bandwidth. The antenna is printed on a low-cost FR-4 substrate with dielectric constant ε_r=4.4, loss tangent tanδ= 0.02, and thickness h=1 mm. A 50-Ω microstrip line with width of 1.96 mm to excite the patch is employed. Both the semicircular patch and microstrip line are printed on the same surface of the substrate. The upper narrow rectangular slot can notch the 5.13-5.87 GHz band for WLAN, and the lower C-shaped slot can notch the 7.2 GHz for some C-band satellite communication systems. The centre frequency of the notched bands are 5.3, 8.3 GHz. Both the centre frequencies and the bandwidths of the notched bands can be controlled by adjusting the slotline parameters, such as the length of each segment, the total length of the slotline, etc. [13]. The dimensions of the antenna are given on Table 1.

Fig. 1. (a) UWB antenna, (b) antenna with notched characteristic on WLAN band, and (c) proposed antenna.

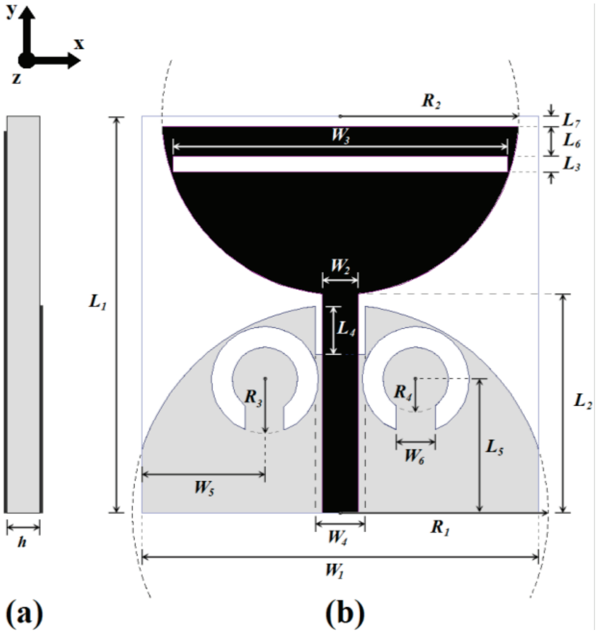

Fig. 2. Geometry of the proposed antenna: (a) side view, and (b) top view.

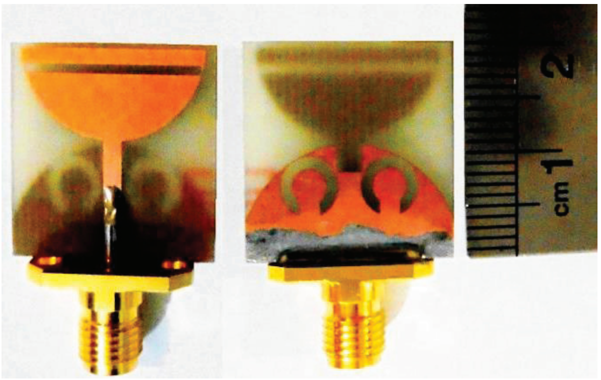

Fig. 3. Photograph of the proposed antenna.

Table 1: Dimensions of the antenna

Parameter	mm	Parameter	mm
R_1	10.5	W_5	6.2
R_2	9	W_6	2
R_3	2.7	L_2	11.1
R_4	1.65	L_3	0.8
$W_1 = L_1$	20	L_5	6.7
W_2	1.96	L_6	1.8
W_3	16.7	L_7	0.5
$W_4 = L_4$	2.5	h	1

III. RESULTS AND ANALYSIS

The HFSS-predicted VSWR [14] against frequency for three structures of the microstrip antenna in Fig. 1 are shown in Fig. 4. In this figure, it is obvious that by using a narrow rectangular slot upon the patch and two slots on the ground the desired bands for WLAN and C-band applications are notched. Influence of the DGS coupling are shown in Fig. 4 (d). It is obvious in Fig. 4 (d), that by eliminating one of C-shaped slots the VSWR characteristic decrease in C-band.

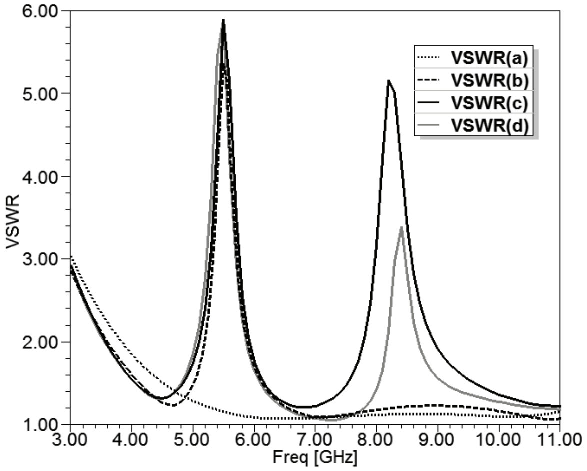

Fig. 4. Simulated VSWR for proposed antenna.

The antenna parameters are studied and the influence of these parameters on the bandwidth are shown in Fig. 5. In Fig. 5 (a), (c), it is obvious that only by variation on L_5 and R_4 the height or the location of the centre frequency of the second band-notched for C-band application is changed. In Fig. 5 (b), by changing the dimensions of the upper rectangular slot on the patch, the variation of the center frequency for WLAN is shown. The antenna is optimised to attain optimum bandwidth in the desired frequency bands. The simulated and measured VSWR for optimization parameters is shown in Fig. 6. In addition, the realized gain in the whole operating band has shown in Fig. 7, as desired in two 5.5 and 8.3 GHz gains decline due to the notch bands. Also, the group delay for the proposed antenna is presented in Fig. 7. It is clear that the variation of the group delay for the proposed antenna is around 1.5 ns for the desired bandwidth, but because of the notch behavior, there is a deviation at the notch frequency in the group delay.

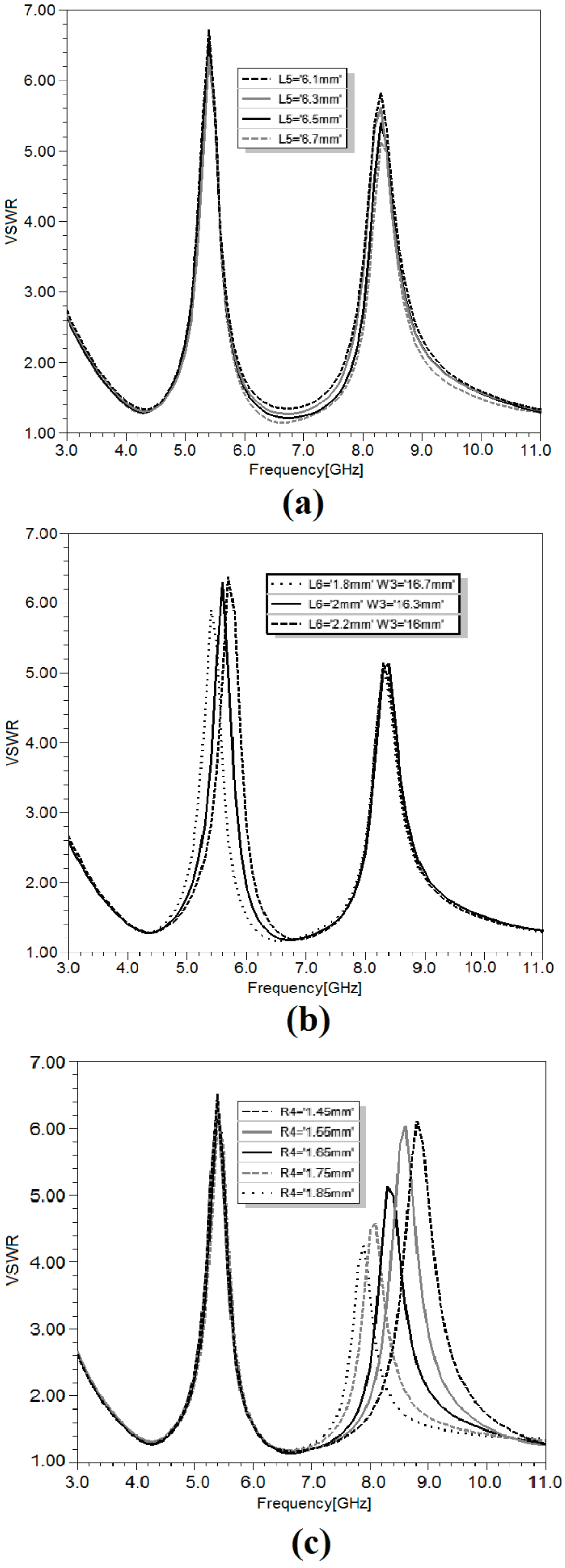

Fig. 5. The simulated VSWR plot for variation of: (a) L_5, (b) L_6, and (c) R_4.

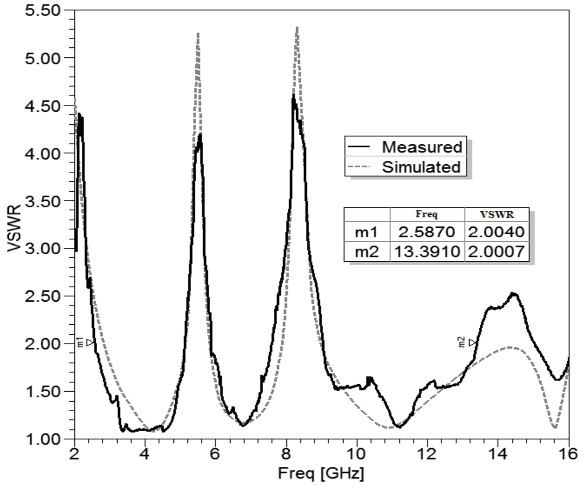

Fig. 6. The simulated and measured VSWR for optimized parameters.

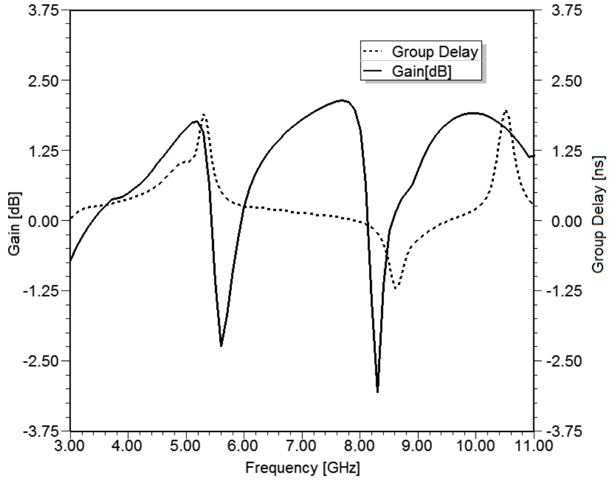

Fig. 7. The peak gain and group delay of the proposed antenna.

The measured and simulation radiation patterns of the proposed antenna at 4.5, 7 and 9.5 GHz are shown in Fig. 8 and Fig. 9. Both the co- and the cross-polar are shown. The antenna gives a nearly omnidirectional radiation pattern in the Z-X plane and a dipole-like radiation pattern in the Y-Z plane. The discrepancy in investigated parameters between simulated and measured results should be mostly attributed to the loss tangent tanδ of the substrate and the tolerance in manufacturing. Eventually it can be said that the simulation and measurment outcomes agree well with each other except two notch bands.

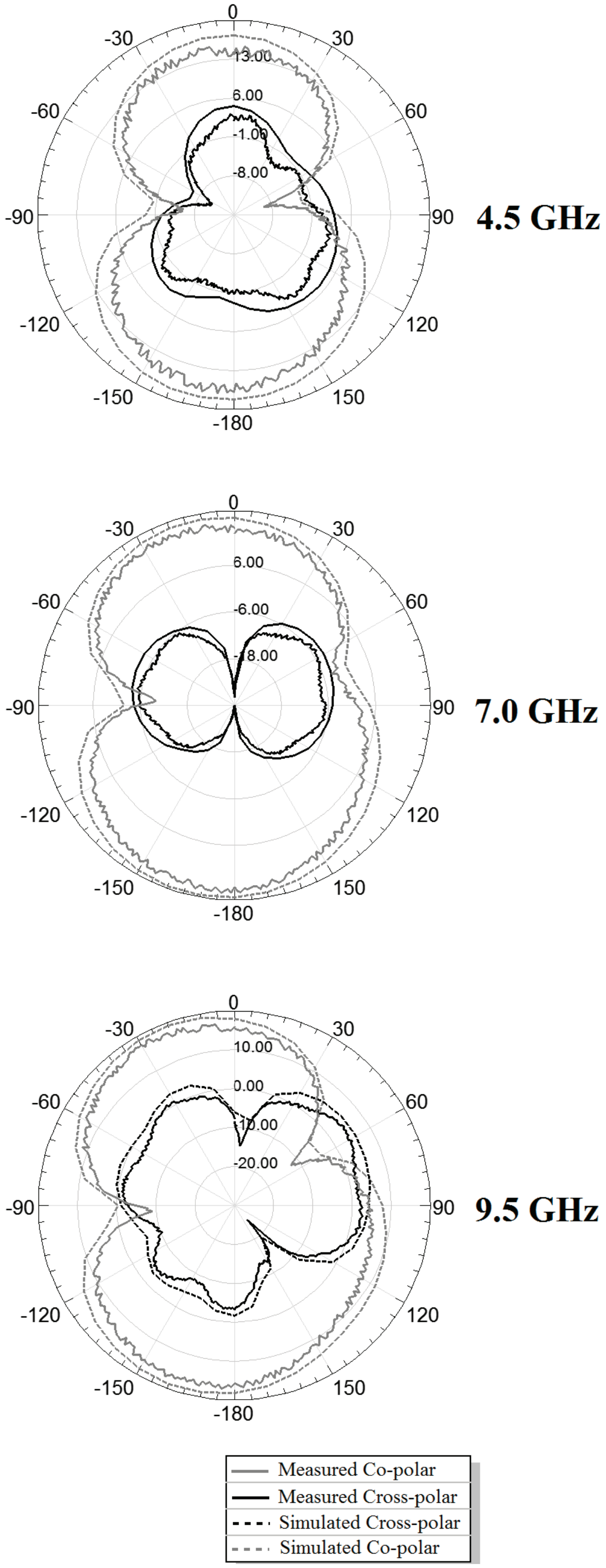

Fig. 8. The measured and simulation radiation patterns (dB) in Y-Z plane.

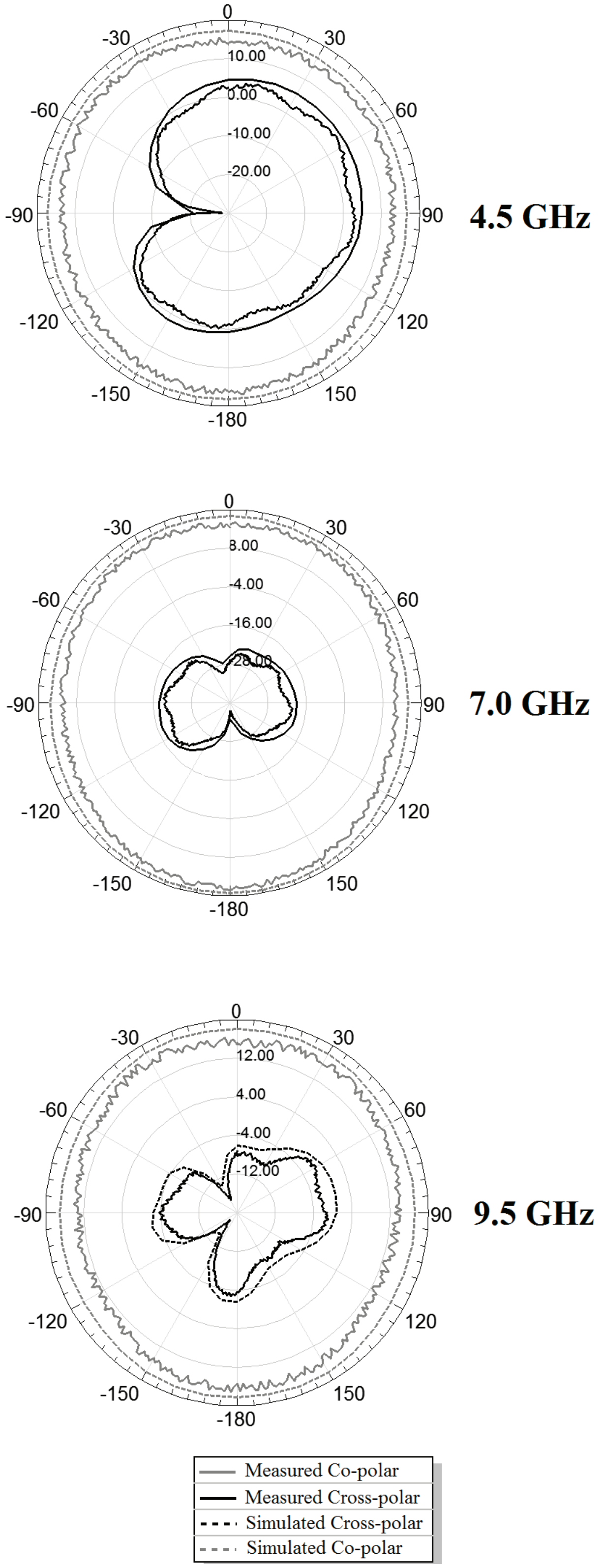

Fig. 9. The measured and Simulation radiation patterns (dB) in Z-X plane.

IV. CONCLUSION

A semicircular printed antenna with dual-band characteristic is presented and discussed. This antenna has a compact and small size 20×20×1 mm^3. This novel microstrip antenna has satisfactory characteristics within its operating bandwidth. To obstruct suppression in the applicable WLAN, and C-band communication systems, pair of symmetrical C-shape slots on the ground and a narrow rectangular slot on the patch is proposed. Prototype of the antenna designed, fabricated, and measured. The suggested low-profile antenna operates from 2.6-13.3 GHz except in two notch bands. The antenna which not only meets the requirement of the UWB systems, but also reduces the potential interference form 5.2 GHz-5.9 GHz for WLAN, 7.8 GHz-9.0 GHz for C-band satellite communications. The measured results show reasonable agreement with the simulated results.

ACKNOWLEDGMENT

This paper is partly supported by Khajeh Nasir University of Technology Antenna Measurement laboratory and the authors appreciatively acknowledge the support.

REFERENCES

[1] Y. Li, W. Li, Si. Li, and T. Jiang, “Miniaturization reconfigurable wide slot antenna for multi-mode wireless communication applications,” *IEEE Asia-Pacific Conference on Antennas and Propagation*, Singapore, Aug. 2012.

[2] C. C. Lin and R. W. Ziolkowski, “Tri-band notched ultra-wideband antenna using capacitively loaded loops (CLLs),” *IEEE*, 2010.

[3] W. S. Lee, D. Z. Kim, K. J. Kim, and J. W. Yu, “Wideband planar monopole antennas with dual band-notched characteristics,” *IEEE Trans. Microw. Theory Tech.*, vol. 54, pp. 2800-2806, 2006.

[4] S. W. Su and K. L. Wong, “Printed band-notched ultra-wideband quasi-dipole antenna,” *Microw. Opt. Technol. Lett.*, vol. 48, pp. 418-420, 2006.

[5] J. I. Kim and Y. Jee, “Design of ultrawideband coplanar waveguide-fed Li-shape planar monopole antennas,” *IEEE Antennas Wirel. Propag. Lett.*, vol. 6, pp. 383-387, 2007.

[6] Y. S. Li, X. D. Yang, C. Y. Liu, and T. Jiang, "Compact CPW-fed ultrawideband antenna with band-notched characteristic," *Electron. Lett*., vol. 46, no. 23, pp. 1533-1534, 2010.

[7] Y. S. Li, X. D. Yang, Q. Yang, and C. Y. Liu, "Compact coplanar waveguide fed ultra wideband antenna with a notch band characteristic," *AEU-Int. J. Electron. Commun*., vol. 65, no. 11, pp. 961-966, 2011.

[8] C. P. Hsieh, T. C. Chiu, and C. H. Lai, "Compact dual-band slot antenna at the corner of the ground plane," *IEEE Trans. Antennas Propag*., vol. 57, no. 10, pp. 3423-3426, Oct. 2009.

[9] W. C. Liu, C. M. Wu, and N. C. Chu, "A compact CPW-fed slotted patch antenna for dual-band operation," *IEEE Antennas Wireless Propag. Lett*., vol. 9, pp. 595-598, 2010.

[10] W. Hu, Y. Z. Yin, P. Fie, and X. Yang, "Compact triband square-slot antenna with symmetrical L-strips for WLAN/WIMAX applications," *IEEE Antennas and Wireless Propagation Letters*, vol. 10, pp. 462-465, 2011.

[11] S. Ghosh, "Band-notched modified circular ring monopole antenna for ultrawideband applications," *IEEE Antennas and Wireless Propagation Letters*, vol. 9, pp. 276-279, 2010.

[12] M. Ojaroudi, S. Yazdanifard, and N. Ojaroudi, "Band-notched small square-ring antenna with a pair of T-shaped strips protruded inside the square ring for UWB applications," *IEEE Antennas and Wireless Propagation Letters*, vol. 10, pp. 227-230, 2011.

[13] C. Deng, L. Li, Q. Gong, D. Zhan, and Y. Zou, "Planar printed monopole antennas for ultrawideband/multi-band wireless systems," *IEEE*, 2011.

[14] C. C. Lin, P. Jin, and R. W. Ziolkowski, "Single, dual and tri-band-notched ultrawideband (UWB) antennas using capacitively loaded loop (CLL) resonators," IEEE Transactions on Antennas and Propagation, vol. 60, no. 1, pp. 102-109, Jan. 2012.

Mahdi Najafpur was born in Tabriz, Iran, in October 1988. He received the Telecommunication Engineering degree from Islamic Azad University, Urmia, in 2010 and the M.S. degree in Electrical and Telecommunication Engineering from Islamic Azad University, Urmia, Iran. He's practically experienced in fields of microwave, mobile communication, as an antenna designer. His research interest includes the area of design and analysis of different kinds of microstrip antenna and ultrawide band antenna.

Javad Nourinia received his B.Sc. in Electrical and Electronic Engineering from Shiraz University and his M.Sc. degree in Electrical and Telecommunication Engineering from Iran University of Science and Technology, and his Ph.D. degree in Electrical and Telecommunication from the University of Science and Technology, Tehran Iran in 2000. From 2000 he was an Assistant Professor and now is Associated Professor in the Department of Electrical Engineering, of Urmia University, Urmia, Iran. His primary research interests are in antenna design, numerical methods in electromagnetic, microwave circuits and filters.

Fateme Azamian Jazi was born on May 2, 1988 in Isfahan, Iran. She received the B.S. degree in Electrical and Telecommunication Engineering from Islamic Azad University of Najafabad in 2007-2011, and the M.S. degree in Electrical and Telecommunication Engineering from Islamic Azad University of Urmia in 2011-2013. Her research interests are in designing of UWB and microstrip antennas and also airplane antennas such as ADF, Radio Altimeter, TCAS, ATC and particle swarm optimization technique.